JAIST Repository
https://dspace.jaist.ac.jp/

Title	溶液プロセスにより形成したイットリウムドープ酸化フニウム-ジルコニウムを用いた酸化物チャネル強誘電体ゲートトランジスタの研究
Author(s)	MOHIT
Citation	
Issue Date	2021-03
Type	Thesis or Dissertation
Text version	ETD
URL	http://hdl.handle.net/10119/17488
Rights	
Description	Supervisor:德光　永輔，先端科学技術研究科，博士

JAIST
JAPAN
ADVANCED INSTITUTE OF
SCIENCE AND TECHNOLOGY

Japan Advanced Institute of Science and Technology

Investigation of Oxide-Channel Ferroelectric-Gate Transistor using Yttrium Doped Hafnium- Zirconium Oxide Fabricated by Solution Process

Mohit

Japan Advanced Institute of Science and Technology

Doctoral Dissertation

Doctoral Dissertation

Investigation of Oxide-Channel Ferroelectric-Gate Transistor using Yttrium Doped Hafnium- Zirconium Oxide Fabricated by Solution Process

Mohit

Supervisor: Professor Eisuke Tokumitsu

Graduate School of Advanced Science and Technology

Japan Advanced Institute of Science and Technology

Materials Science

March 2021

Abstract

In this work, ferroelectric yttrium-doped hafnium-zirconium oxide (Y-HZO) has been realized by the chemical solution deposition (CSD) and applied to gate insulator of ferroelectric gate thin film transistor (FGT). Oxide semiconductor or conductor, In_2O_3 or In-Sn-O (ITO) was used as a channel, which was fabricated by CSD, too.

Ferroelectric properties of Y-HZO with various annealing temperature and environment was studied. Samples annealed at 600–800 °C in a vacuum, N_2 and O_2 environment showed ferroelectricity, which was confirmed by the polarization–electric field and capacitance–voltage measurements. It was found that the ferroelectric properties were dramatically improved when the samples were annealed in a vacuum at 800 °C and the leakage current was decreased, compared to the Y-HZO films annealed at 800 °C in oxygen and nitrogen.

Next, stability of ferroelectricity in HZO films deposited by sputtering and CSD has been investigated for oxide channel ferroelectric-gate thin film transistor application. Since it is known that the ferroelectric orthorhombic phase is metastable in HfO_2-baseed ferroelectric materials and we need to deposit oxide channel layer on the ferroelectric gate insulator followed by the annealing process, the robustness of the ferroelectricity is important to fabricate FGTs. After confirming the ferroelectricity of both sputtered HZO and CSD yttrium-doped HZO (Y-HZO) films, indium-tin-oxide (ITO) was deposited by sputtering on sputtered HZO or CSD Y-HZO layer to fabricate metal-ferroelectric-semiconductor (MFS) structure. Then, the MFS structures were re-annealed in N_2 environment for 15 min to examine the robustness of ferroelectricity. Interestingly, it was found that the sputtered HZO films became paraelectric which was confirmed by both X-ray diffraction (XRD) pattern and electrical measurements. On the other hand, the CSD Y-HZO films showed ferroelectric nature even after the re-annealing with a negligible monoclinic phase.

Then, ferroelectric gate transistor (FGT) with Y-HZO gate insulator and oxide channel with various thickness of In_2O_3 and ITO were fabricated. Both Y-HZO and channel layers were fabricated by chemical solution deposition (CSD). First, ferroelectric properties of vacuum and oxygen Y-HZO in the metal–ferroelectric–semiconductor (MFS) structure with 5-22 nm thick

In_2O_3 and 6-24 nm thick ITO, have been confirmed by polarization-voltage (P-V) and capacitance-voltage (C-V) characteristics. The C–V curves showed clear butterfly loops showing the depletion of In_2O_3 and ITO layer. Vacuum annealed samples show good ferroelectric properties as compared to oxygen annealed samples. Secondly, the device performance of FGTs for both vacuum and oxygen annealed samples has been evaluated with various thickness of In_2O_3 and ITO channel layer. The fabricated FGTs exhibited typical n-channel transistor operation with a counterclockwise hysteresis loop in their transfer curves due to the ferroelectric nature of the Y-HZO-gate insulator. It was found that FGT shows low sub-threshold voltage swing (SS), high on/off drain current ratio of 10^6, large on current, and memory window for vacuum annealed sample. In contrast, FGTs with Y-HZO gate insulator annealed in oxygen show degraded device performance due to high leakage current. In this thesis, good electrical properties have been demonstrated for oxide channel FGTs with ferroelectric Y-HZO gate insulator fabricated by CSD with vacuum annealing process, which can be a suitable candidate for future low-cost ferroelectric device and memory applications.

Keywords: Ferroelectric Hafnium dioxide, oxide channel, Ferroelectric Gate Transistor, solution process, thin films.

Acknowledgement

First of all, I would like to take this opportunity to thank Prof. Eisuke Tokumitsu to for accepting me in his lab even after spending 1.5 year in Mizuta lab. I am also thankful to Prof. Eisuke Tokumitsu for giving me such a interesting and hot topic that is *HfO_2 based ferroelectric gate transistors (FGT)*. His continuous guidance, suggestions, constructive criticism and kind support helped me motivate and focused throughout my doctoral course.

I would like to thank Prof. Hiroshi Mizuta for accepting me in his laboratory and teaching me about basic knowledge, necessary for research.

I would also like to thank the members of the review committee Prof. Masahiko Tomitori (JAIST), Prof. Hideyuki Murata (JAIST), Assoc. Prof. Masashi Akabori (JAIST), and Prof. Norifumi Fujimura (Osaka Prefecture University,Osaka), who have spent their valuable time to read the thesis and agreed to be a part of the review committee.

I would like to thank Dr. Shinji Migita, Dr. Hiroyuki Ota and Dr. Yukinori Morita for providing sputtered HZO samples.

I would like to thank Dr. Ken-ichi Haga for helpful discussion about solution process and ferroelectricity.

I am also grateful to Prof. Yuzuru Takamura for his fruitful discussions with a kind direction to conduct my minor thesis in his laboratory.

I would like to express my sincere gratitude to Assistant Prof. Daisuke Hirose of Takamura lab who help and teach me vacuum annealing system, Rf sputtering for Pt, Device parameter analyzer, MLA, glove box and other things. His valuable discussion and support helped during my minor research.

I owe deep sense of gratitude towards Dr. Takaaki Miyasako of Murata who help me with FGT design and fabrication process. His valuable suggestion and useful discussion helped me during FGT process.

I would like to express sincere thanks to Mr. Tatsuya Murakami from CNMT for invaluable support for XPS measurements.

I would like to express thank to my lab members Furuchi kun for teaching me Hall measurement and sputtering ITO, Kobayashi kun, Sasaki kun, Hara kun and Saito kun. I would

like to thank Dr. Takuya Iwasaki for suggesting me JAIST during my master in the UK. I would like to thank my friends in JAIST for their help and support during my journey Ph.D. Dr. Gargi Joshi for helping me with SEM measurement, Jyotish Patidar for teaching me XRD, Dr. Kunle for teaching me AFM, Dr. Rahul Bhardwaj for helping me with various things in VBL, Dr. Amit Kumar, Dr. Maninder Singh, Dr. Priyank Mohan, Dr. Neha Sharma.

I thank extensively my wife for unbeatable and incredible support throughout these years. I believe that without her continuous love, I would not able to complete my Ph.D journey.

In last but not the least, I would like to express thank my family for continuous love and indebted support through my doctoral course.

Mohit

Graduate School of Advanced Science and Technology

Japan Advanced Institute of Science and Technology

March 2021

Contents

Chapter 1 1

1. Introduction 2

1.1. General introduction 2

1.2. Ferroelectricity and history of ferroelectricity 2

1.3. Conventional ferroelectric materials 4

1.4. Ferroelectricity in hafnium dioxide 7

1.4.1. Properties of bulk HfO_2 7

1.4.2. Undoped HfO_2 thin films (High-k gate insulator) 10

1.4.3. Dielectric constant enhancement and stabilization of ferroelectric phase in HfO_2 12

1.5. Oxide channel ferroelectric gate thin film transistor (FGT) 16

1.5.1. Ferroelectric field effect transistor (FeFET) 16

1.5.2. Operating principle of FGT 17

1.5.3. Physical properties of Ferroelectric HfO_2 for FGT 18

1.6. Research objective 20

Chapter 2 24

2. Experimental details 25

2.1. Deposition methods of ferroelectric HfO_2 25

2.1.1. Atomic Layer Deposition (ALD) 25

2.1.2. Sputtering 26

2.1.3. Chemical Solution Deposition (CSD) 28

2.2. General process for fabrication of ferroelectric Y-HZO and oxide semiconductor thin films by Chemical solution process 31

2.2.1. Substrate cutting and cleaning 31

2.2.2. Preparation of precursor solution 31

2.2.3. Deposition of thin films 32

2.3. Analytical methods 33

2.3.1. X-ray diffraction 33

2.3.2. XPS 34

2.3.3. SEM 37

2.3.4. AFM 38

Chapter 3 43

3. Impact of annealing environment on electrical properties of yttrium-doped hafnium zirconium dioxide thin films prepared by the solution process. 44
3.1. Motivation 44
3.2. Experimental procedure 45
3.3. Crystallinity of films 45
3.4. XPS analysis 47
3.5. SIMS 49
3.6. TDS 50
3.7. Surface morphology of films 51
3.8. Effect of annealing temperature on vacuum annealed Y-HZO films. 53
3.9. Effect of annealing temperature on N_2 annealed Y-HZO films. 57
3.10. Effect of annealing temperature on O_2 annealed Y-HZO films. 60
3.11. Effect of annealing environment on Y-HZO films 62
3.12. Comparison of ferroelectric properties of HZO 64
3.13. Conclusion 66
Chapter 4 69
4. Stability of ferroelectric phase in HZO films 70
4.1. Motivation 70
4.2. Experimental 71
4.3. Crystallinity of films 74
4.4. Electrical properties 76
4.4.1. Sputtered HZO 76
4.4.2. CSD Y-HZO 83
4.5. Conclusion 90
Chapter 5 92
5. MFS and FGT using CSD Y-HZO 93
5.1. Motivation 93
5.2. Experimental details 94
5.2.1. Fabrication of MFS with 110 nm thick CSD ITO as a top electrode (oxygen annealed) 94
5.2.2. Fabrication of FGT 95
5.3. Ferroelectric properties of MFS structure 97
5.3.1. 110 nm thick CSD ITO (as metal electrode) 97
5.3.2. 5-22 nm thick CSD In2O3 /Y-HZO (Vacuum annealed) MFS structure 98
5.3.3. 6-24 nm thick CSD ITO /Y-HZO (Vacuum annealed) MFS structure 103
5.3.4. 5-22 nm thick CSD In_2O_3 /Y-HZO (oxygen annealed) MFS structure. 107
5.3.5. 6-24 nm thick CSD ITO /Y-HZO (oxygen annealed) MFS structure. 111

5.4. FGT 115
5.4.1. FGT with CSD In_2O_3 channel and vacuum annealed Y-HZO 115
5.4.2. FGT with CSD ITO channel and vacuum annealed Y-HZO 117
5.4.3. FGT with CSD In_2O_3 channel and oxygen annealed Y-HZO 119
5.4.4. FGT with CSD ITO channel and oxygen annealed Y-HZO 121
5.4.5. FGT with sputtered ITO and CSD Y-HZO (vacuum annealed)/ sputtered HZO 123
5.4.6. Comparison of FGT performance with previous work 124
5.5. Conclusion 125
Chapter 6 127
6. Conclusion and future work 128
6.1. Conclusion and summary of this research 128
6.2. Future work 130
6.3. List of Accomplishments 131

Dedicated to my father, mother, and wife

The years of anxious searching in the dark, with their intense longing, their alternations of confidence and exhaustion, and final emergence into light—only those who have experienced it can understand that

-Albert einstein

Chapter 1
Introduction

1. Introduction

1.1. General introduction

The modern electronics begins after a discovery of transistor operation demonstrated by William Shockley in the late 1940's. Mohamed Atalla and Dawon Kahng invented metal-oxide-semiconductor field effect transistor (MOSFET) at Bell laboratories in 1960. MOSFET becomes main device for current large-scale integration (LSI). The intense amount of work has been done to scale down the transistor dimensions that leads to improve their performance. According to Moore's law, "the number of transistors of an integrated circuit doubles each two years" [1]. However, progress in scaling of integrated circuit needs continuous innovation in many fields. In past few years, the decrease of electrical thickness of capacitor and gate insulator has become one of the major challenging topics. Previously, this was achieved by reducing thickness of dielectric such as silicon dioxide (SiO_2). However, this approach results in increase of leakage current, which prevents the MOSFET from further scaling down to sub nanometer regime. Hence, further improvement is possible by using high-k gate insulator material such as HfO_2 which allows reduction of electrical thickness without decreasing physical thickness. On the other hand, another challenge is to lower the subthreshold swing of the scaled MOSFET, which is limited to 60 mV/dec at room temperature. Internet of things (IoT) devices operates mostly in sleep mode (low power consumption) and it wakes up to do operation when required. Therefore, IoT application requires new innovative transistor and memory device technology. Ferroelectric materials as gate insulator are suitable for IoT applications

1.2. Ferroelectricity and history of ferroelectricity

The capability to retain remaining or remanent polarization (P_r) in non-existence of an electric field and to switch polarization by external electric field application, provides ferroelectric materials. They have exceptional ability of utilizing its polarization state as basis for electronic memories. The ferroelectricity occurs in polycrystalline or crystalline materials as result of polar, non-centrosymmetric crystal structure. Ferroelectricity can be further defined as a pyroelectric material in which there are at least two thermodynamically stable polarization states. In usual dielectric materials such as SiO_2, net polarization exists as result of distortion of electron cloud and nuclei of atom but disappear when electric field is removed. On the other

hand, ferroelectric materials exhibit a relative displacement of anions and cations within unit lattice cell, which remains even when electric field is removed. Hence, the P_r remains stable when electric field is removed and can be reverse when electric field with opposite polarity is applied.

Ferroelectricity was discovered in 1920 in Rochelle salt by Valasek [2]. After Rochelle salt, ferroelectric gained great interest and scientists all over the world were curious to find any other ferroelectric materials than the Rochelle salt. Paul Scherrer was among them, who is well known in the material science community for providing the formula to calculate the grain size from the rocking curve of x-ray diffraction measurements (XRD). Scientist during that period does not have clear understanding about the origin of ferroelectricity. It was still confusing that what was essential for a ferroelectric material. The confusing state lied between the molecules of water of crystallization or mobile hydrogen atoms [3]. Steulmann thought about the presence of some kind of dipoles in these crystals without elaborating further. In 1935, Busch and Scherrer proved his statement true about the existence of some dipole that result in showing showed ferroelectricity in KH_2PO_4 with a critical temperature of about 123 K [4]. Much later, ammonium iodate found to be antiferroelectric. During the Second World War, significant interest was triggered in ferroelectric materials mainly due to sonar and other defense related applications. As a result, ferroelectricity was discovered in Barium Titanate, $BaTiO_3$ (first artificial perovskite structure) in USA, Russia and Japan during 1942 and 1944. This triggers research on

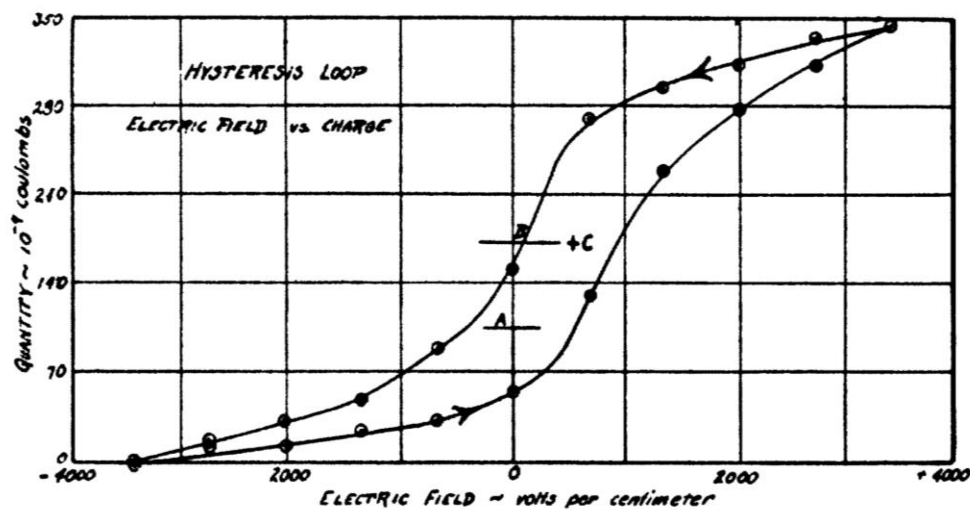

Figure 1.1 First hysteresis curve (Rochelle salt)[2]

ferroelectricity in $BaTiO_3$ (BT) in USA. Initial studies showed mixing or doping TiO_2 and BaO together results in ceramics material with dramatic improvement in dielectric constant. Thurnmaurer and Deaderick prepared mixed oxide in early 1942 at the American Lava Corporation [5]. Later the Erie Resistor Company (sold out to muRata and known as muRata Erie North America) measured higher dielectric constant exceeding 1000 which is ten times higher than other ceramics material such as TiO_2 (ε_r 110). The discovery of ferroelectricity in simple oxide materials such as $BaTiO_3$ was extremely important, and it was not correlated with hydrogen bonding always. $BaTiO_3$ was named based on member of the perovskite family, which has similar structure to naturally occurring $CaTiO_3$. As result, several investigations were done to understand structural changes occurring at the phase transitions using x-ray diffraction. Several years later, Smolenskii, Pepinsky and Mattias from USA, expanded the list of ferroelectric crystals [6]. After that, many other ferroelectric ceramics, such as lead titanate (PbTiO3), lead zirconate titanate ($Pb(ZryTi_{1-y})O_3$), lead lanthanum zirconate titanate ($(Pb_xLa_{1-x})(Zr_yTi_{1-y})O_3$) have been introduced and come up with variety of applications.

1.3. Conventional ferroelectric materials

As discussed in the previous section, ferroelectric material has spontaneous polarization. In addition, it can be reversed when an electric field is applied externally. The ferroelectric material shows wide range of useful characteristics as an electronic material.

- shows ferroelectric hysteresis which can be used in non-volatile memory.
- exhibit very high relative permittivity (several thousand) which the application of capacitors.
- shows piezoelectric effect (charge is generated when mechanical stress is applied) is extensively used in sensors such as accelerometers, microphones, hydrophones etc.
- shows pyroelectric effect (charge is produced when material temperature is changed) can be used in
- shows electro-optic effect (Pockels effect, Kerr effect, etc.) and non-linear optical effect which can be used in integrated optical (photonic) devices, laser Q-switches and optical shutters.

As shown in Figure 1.2, ferroelectric materials shows both the characteristics of piezoelectric, and pyroelectric. However, all pyro- or piezoelectric are not ferroelectric. Ferroelectric and pyroelectric materials are polar and spontaneously polarize or possess an electric dipole moment below the transition temperature. However, when the electric field applied, this polarity can be reoriented or reversed fully or in part

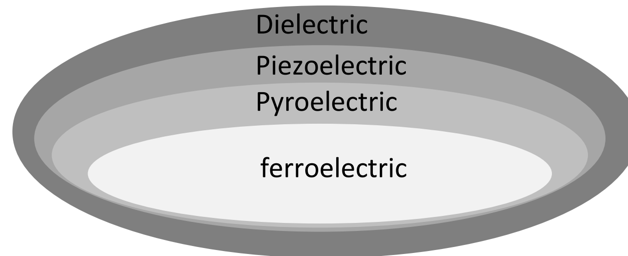

Figure 1.2 Classification of ferroelectrics into the different classes of dielectric materials

Conventional ferroelectric materials are used in the above features with their application. Most widely used conventional ferroelectric materials are from the perovskite oxides family for examples $Pb(Zr,Ti)O_3$ (PZT) and BT, or layer by layer perovskites such as $(Bi,La)_4Ti_3O_{12}$ (BLT), $BiFeO_3$ (BFO) and $SrBi_2Ta_2O_9$ (SBT). Figure 1.3 shows the crystal structure of perovskites based on conventional ferroelectric materials These types of materials have the general composition of CBO_3, where C and B represent a different cation element or combination of two or more such kind of elements. . The physical properties of perovskite-based conventional ferroelectric are very diverse which depends on cationic order. For instance, PZT shows P_r more than 20 μC/cm^2 where layered perovskite structure, BLT, and SBT shows P_r more than 10-15 μC/cm^2. Polarization happens due to smaller ions move up and down depending on the direction, and the polarization is maintained even if the applied voltage is 0 V. Polarization direction up and down is analogous to 1 and 0 of Boolean.

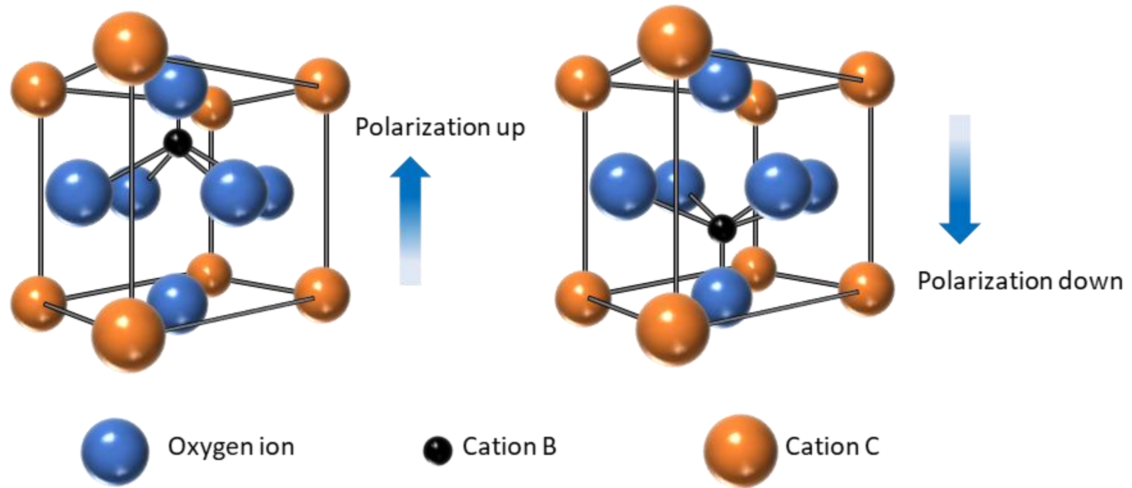

Figure 1.3 Crystal structure of the Conventional ferroelectric materials [7]

algebra respectively, can be used in nonvolatile memory. However, conventional ferroelectric material has several issues. Firstly, conventional ferroelectric materials suffer from the size effect, that is when the thickness is below 100 nm ferroelectric properties degrades drastically as shown in Figure 1.4 **P–E characteristics of PZT thin films with different thickness under 1–5 V[8].** . Secondly, small bandgap (Eg, 3–4 eV),generates a Schottky barrier height of only 1 eV in regard to the metal electrodes, and scaling effect has to be taken into consideration[8]–[10], Thirdly, poor compatibility with CMOS technology. Fourthly, defects such as oxygen vacancies because of relatively weak bonding energy of oxygen with constituent metal ion in conventional ferroelectric materials. As a result, problems like imprint, fatigue, and retention problems are originated [11]. In addition, lead in PZT films are hazardous to environment which draws the interest in developing new lead-free ferroelectric materials which has good compatibility, large P_r, E_g and with a high bonding energy between metal ions and oxygen.

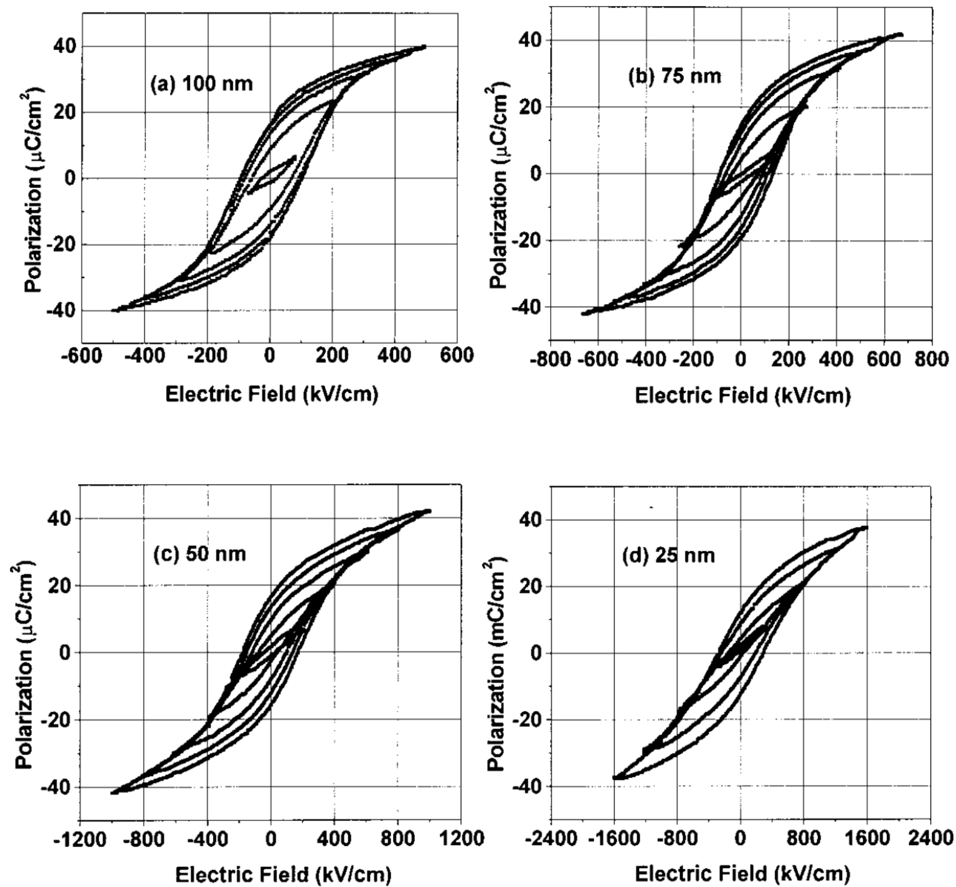

Figure 1.4 P–E characteristics of PZT thin films with different thickness under 1–5 V[8].

1.4. Ferroelectricity in hafnium dioxide

1.4.1. Properties of bulk HfO_2

The conventional use of bulk HfO_2 has been in nuclear applications as a result of high neutron cross-section absorption coefficient, and transformation toughening in ceramics for structural application has been an great interest [12]. Transformation toughening implies to enhancement in mechanical properties of a ceramic material during a crystal phase transition such as from the tetragonal phase to monoclinic phase transition into hafnia and zirconia which can achieved by applying external forces such as stress. ZrO_2 and ZrO_2 based toughened ceramics exhibited an exceptionally large fracture strength and toughness but stabilization of tetragonal phase above 1000 °C limits its utilization in applications [12]. In case of HfO_2, phase transition occurs at approximately 1700 °C which can be used in the high-temperature

application, even though it has not demonstrated good mechanical properties as seen in ZrO_2 [12]. However, HfO_2 and ZrO_2 forms completely mixable solid solution which can be expressed as $Hf_xZr_{1-x}O_2$. Figure 1.5 HfxZr1-xO2 solid solution system [13]. HfO_2 transfers through monoclinic to tetragonal to cubic to liquid phase transition with increasing temperature [13] and high pressure can result in formation of an orthorhombic phase[12], [14], [15]. Figure 1.6 **Phase diagram of HfO2 and ZrO2 with variation in temperature** [12]**.**shows a phase diagram of bulk HfO_2 with respect to temperature and pressure. Wide variation in pressure results in observation of the orthorhombic phase in bulk HfO_2 [12]. Figure 1.7 depicts crystal structure of Monoclinic(P21/c) and orthorhombic phase (Pbc21, Pbca and Pnma) which have been reported [15]. The dopant such as MgO, Y_2O_3 and Yb_2O_3 typically lowers the phase transition temperature for stabilization of the tetragonal and cubic phase. Kisi first reported existence of an orthorhombic Pbc21 crystal phase while investigating stabilization of crystal structure of Mg doped ZrO_2 at low temperature and under hydrostatic pressure [16]. Formation of orthorhombic phase was due to transformation from tetragonal phase. This orthorhombic phase which is also known as $Pbca_1$ is responsible for ferroelectricity in HfO_2 which will be discussed in later section[17].

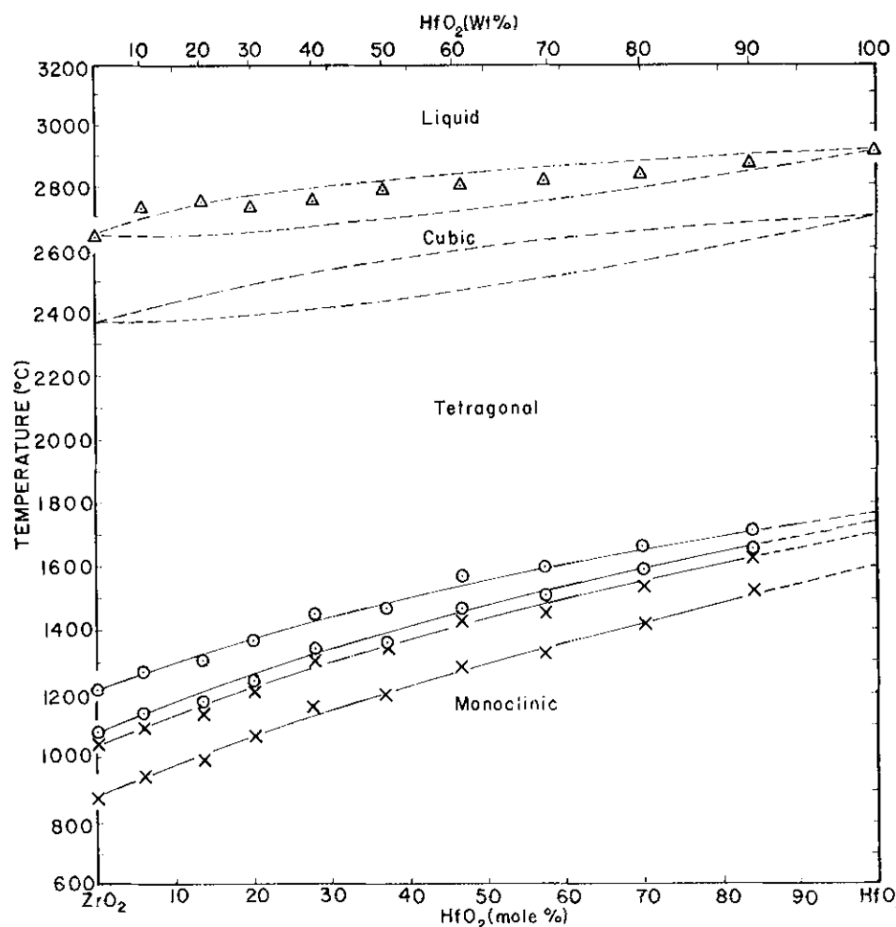

Figure 1.5 $Hf_xZr_{1-x}O_2$ solid solution system [13].

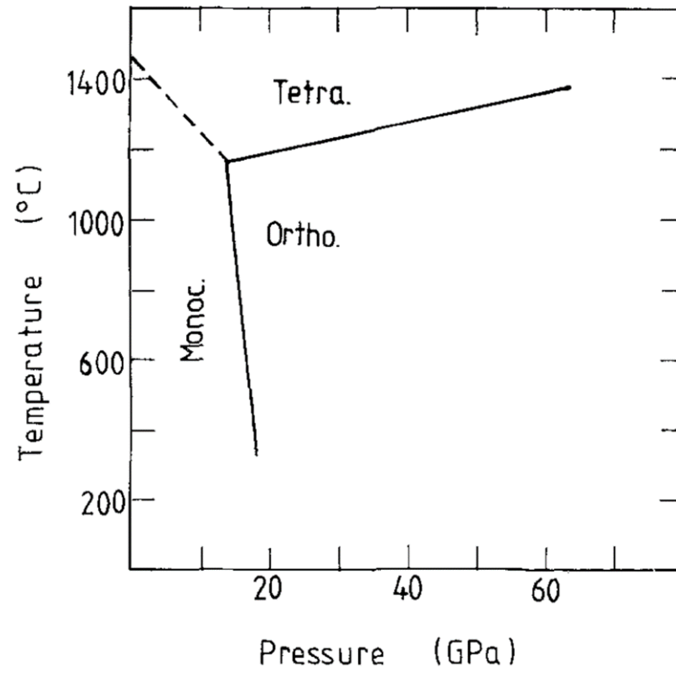

Figure 1.6 Phase diagram of HfO_2 and ZrO_2 with variation in temperature [12].

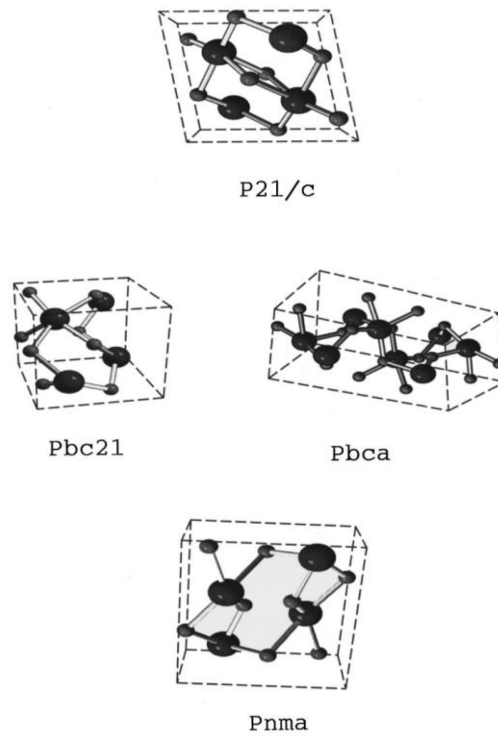

Figure 1.7 Crytsal structure of HfO_2 [12].

1.4.2. Undoped HfO_2 thin films (High-k gate insulator)

In early 2000s, the aggressive demand of scaling down silicon CMOS has been made it mandatory to replace SiO_2 with high-dielectric-constant (high-k) material. As a result, excessive tunneling current when thickness of SiO_2 is decreased [18]. The replacement of SiO_2 with high-k gate insulator was required. As a consequence, device scaling down can be continued with Equivalent Oxide Thickness (EOT) of their devices. However, at the same time using a physically thicker dielectric resulted in a leakage current reduction [18]. The EOT can be estimated by

$$T_{ox} = \frac{3.9}{K}\ t$$

Where T_{ox} is EOT, k is relative dielectric constant, and t is physical thickness of high-k gate insulator. The candidates for high-k insulator are La_2O_3, Lu_2O_3, Al_2O_3, HfO_2, ZrO_2, TiO_2, Sc_2O_3 Y_2O_3, Nb_2O_5, Ta_2O_5. Several parameters must be considered for choosing suitable high-k material gate insulator. Firstly, k value should be over 12, preferably 25-35 and bandgap over 5 eV [18]. *Figure 1.8* **Dielectric contant as function of band ganp for various dielectric materials**[18] . shows bandgap and relative dielectric constant of various gate insulator material. Bandgap inversely proportional to tends to vary inversely with its bandgap. For instance, $SrTiO_3$ ($\varepsilon_r = 300$) and TiO_2 (ε_r = 50-100) show low band gap about 3.3 eV. On contrary, ZrO_2 and HfO_2 have relatively suitable band gap of 5.5 eV and ε_r of 18-25 for monoclinic phase. Secondly, high-k gate insulator should be thermodynamic stable, which means either rmetal oxide must not react with Si to form SiO_2 or a silicide by the reactions. However, ZrO_2 is not thermally robust as compared to HfO_2 because ZrO_2 exhibits lower crystallization temperature and zirconium silicide ($ZrSi_2$) [19]. HfO_2 is suitable candidate for CMOS technology. Even since HfO_2 gate dielectric has been incorporated in commercial Intel 45-nm-node process in 2007 [18]. Advancement in technology and competitive nature of semiconductor industry from conventional planer to 3D structure of device as shown in Figure 1.9. Many changes occurred in transistor structure since 2007 but HfO_2 as gate dielectric in CMOS remained unchanged and unchallenged.

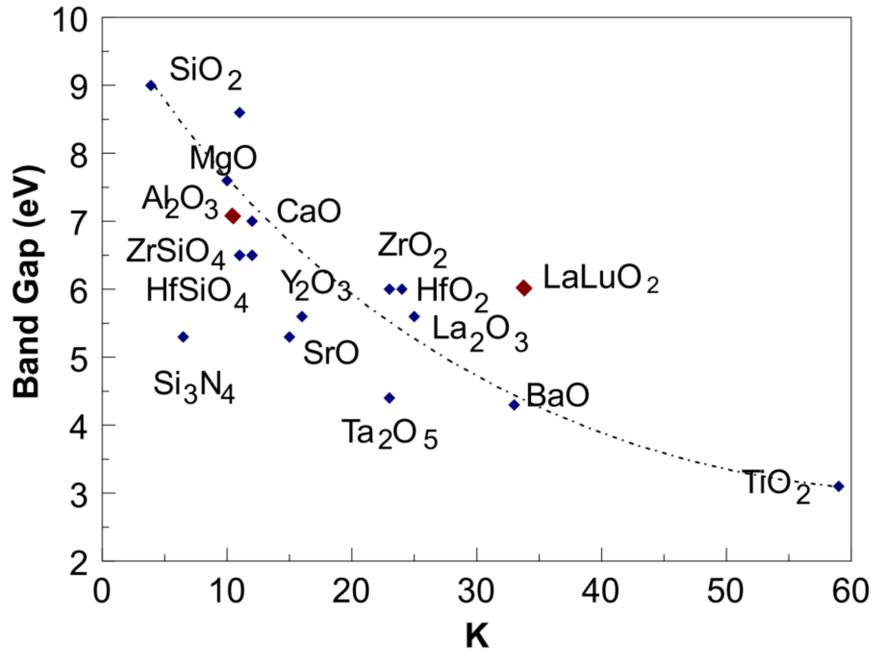

Figure 1.8 Dielectric contant as function of band ganp for various dielectric materials[18] .

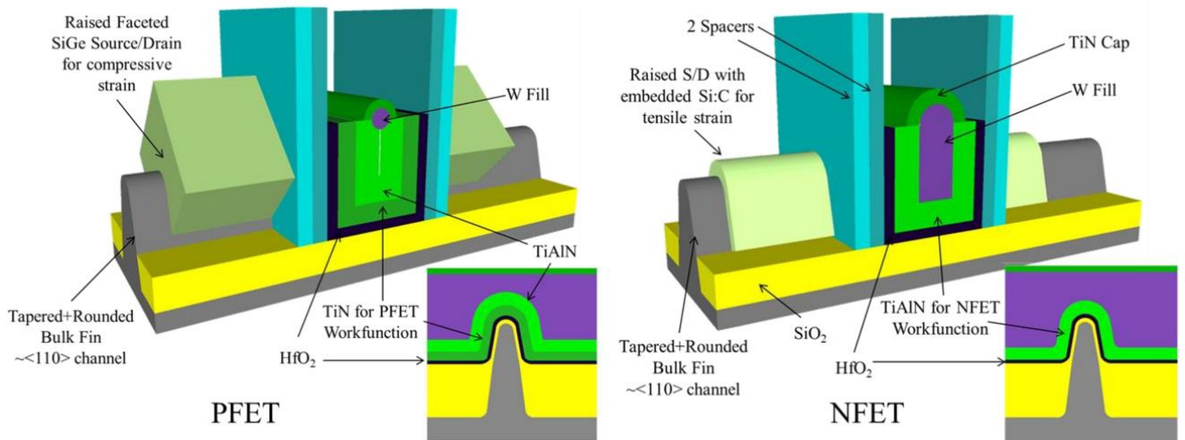

Figure 1.9 Schematic diagrams of P-type MOSFET (PFET) and N-type MOSFET (NFET) of Intel 22 nm node [18].

1.4.3. Dielectric constant enhancement and stabilization of ferroelectric phase in HfO_2

HfO_2 has been used in both transistor and metal-insulator-metal (MIM) capacitors for DRAM as dielectric material–and there has been a significant interest in improving dielectric constant in order to enhance device performance. Amorphous HfO_2 films are preferred due to high ε_r and low leakage current density for gate insulator application in MOSFETs. To achieve higher dielectric constant, polycrystalline HfO_2 films would be preferable. HfO_2 crystallize into three general phases, namely monoclinic phase, cubic and tetragonal which has ε_r 18, 29 and 70 respectively[20]. HfO_2 crystallizes in monoclinic phase at ambient conditions. Monoclinic phase has lowest free energy of formation and largest volume compared to other phases [21]. Therefore, low symmetry monoclinic phase is most stable at room temperature and increase in temperature leads to formation of high symmetry cubic and tetragonal phase [12]. However, introducing doping element can reduce the phase transition temperature and may result in stabilization of tetragonal or cubic phase[12]. In 2006, Kazuyuki Tomida et al reported dielectric constant of polycrystalline enhanced when Si content is less than 10 percent as shown in Figure 1.10. In addition, theoretical calculation suggests that monoclinic phase become less energetically stable than the tetragonal phase because of Si doping. It results in shorter Si-O bond length stretching in tetragonal phase compared to monoclinic phase [22]. However, Si doped HfO_2 films become amorphous even at 800 ^{o}C when Si content is higher than 10%. This is due to increase in crystallization temperature as shown in Figure 1.10. Furthermore, dielectric constant also decreases when Si content is higher due to Si has low polarizability compared to Hf.

In 2011, Böscke et al. first observed ferroelectricity in 10 nm Si-doped HfO_2 [17], [23]. Böscke discovery ferroelectricity in HfO_2 thin films while investigating enhancing dielectric constant for DRAM application at Qimonda memory company in 2007 [24]. Therefore, DRAM dielectric constant can be enhanced by doping HfO_2 or metal capping (mechanical encapsulation). Ferroelectricity in Atomic Layer Deposition (ALD) Si:HfO_2 films was discovered while searching for enhanced DRAM dielectric constant. However, requires crystallization of doped HfO_2 with post metallization annealing (PMA) which is also known as capping effect. Figure 1.11 (a) represents phase transformation from tetragonal to ferroelectric orthorhombic phase while cooling with metal cap [23]. Figure

1.11(b) indicates XRD patterns of 10 nm thick Si doped HfO_2 with and without metal cap, diffraction peak from orthorhombic phase is clearly observed with metal cap

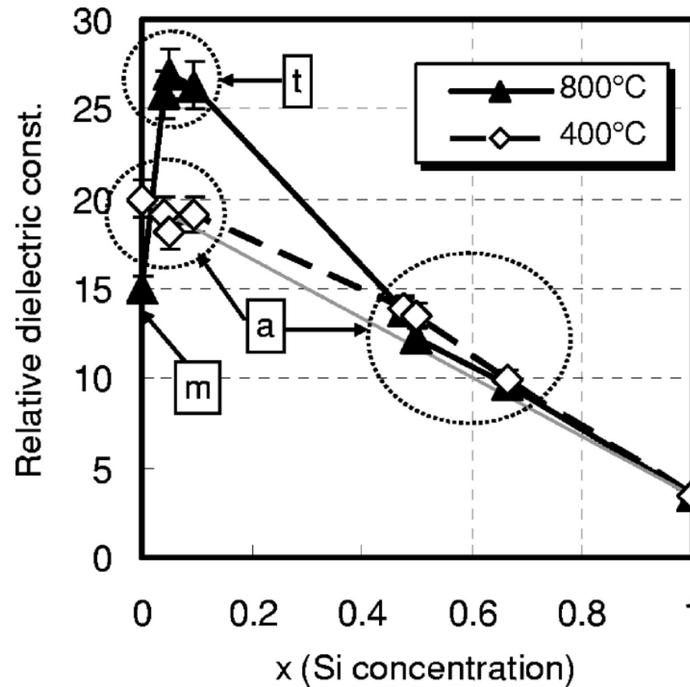

Figure 1.10 Dielectric constant of HfO_2 as function of silicon concentration[22]

whereas monoclinic phase is dominant without cap [23]. Figure 1.11(c) shows C-V curves of Si doped HfO_2 which clearly increase in capacitance near the coercive field due to ferroelectric nature for metal capped Si doped HfO_2 whereas straight curve is observed due to paraelectric nature of Si doped HfO_2 for without metal cap. Figure 1.11 (d) clearly shows ferroelectric hysteresis loop of Si doped HfO_2 films when doping is 3.8 % whereas anti-ferroelectric hysteresis loops when doping is 5.6 percent. Therefore, metal capping is important to stabilized. Later in 2012, Müller reported ferroelectricity in 7.5 nm to 9.5 nm thick ALD Zirconium doped Hafnium or HZO films [25]. In contrast to Si-doped HfO_2 which exhibits ferroelectricity when annealed at 1000 ^oC and had crystallization temperature above 500 ^oC, $H_{0.5}Zr_{0.5}O$ films were crystallization at as low as 450 ^oC. Figure 1.12 (a) shows P-E loops and C-V curves over wide range of Zr concentration. Pure HfO_2 and ZrO_2 shows paraelectric and anti-ferroelectric nature due to monoclinic and tetragonal phase. P_r and ε_r increased, 17 and 25 for $Hf_{0.5}Zr_{0.5}O_2$ respectively due to decrease in m-phase as shown in Figure 1.12 (b). As a result, HZO gain significant attention due to high P_r and exhibits ferroelectricity in wide range of doping which makes HZO as suitable candidate for various application [25], [26]. Doping and metal capping

is important. Later, Migita et al reported, sputtered HZO without metal cap over wide range of annealing as shown in Figure 1.13. If the major phase is orthorhombic and minor phase is monoclinic phase, then it is represented as O/M. Dashed lines are the general guidelines where the dominant phase changes with annealing time. Tetragonal phase is dominant when annealing temperature and time low and short respectively. But when annealing temperature is increased, small amount of orthorhombic phase appears. when the annealing temperature is 600-800 ºC and annealing time is 0-10 mins orthorhombic phase is dominant.

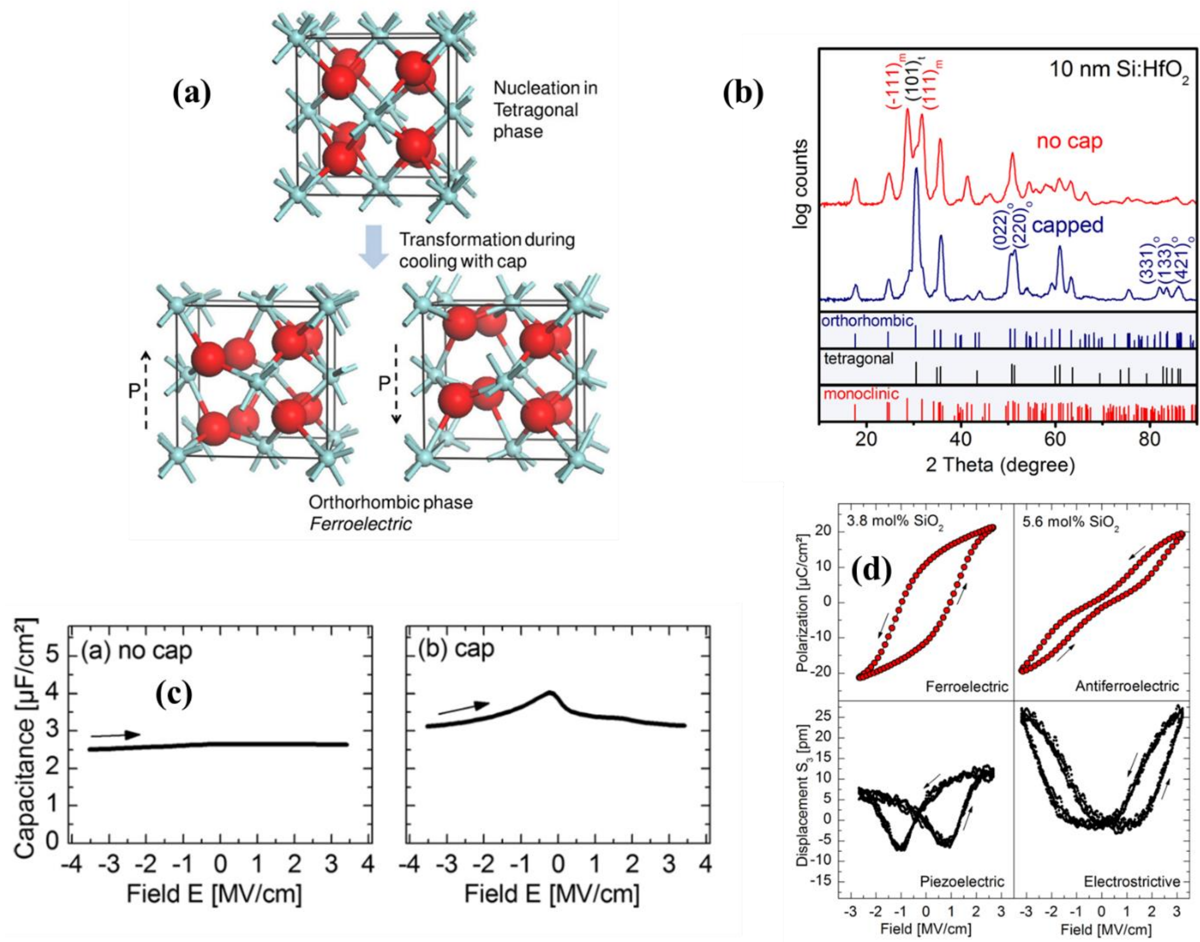

Figure 1.11 (a) Crystal Structure transformation of HfO_2 from tetragonal phase to ferroelectric phase with capping. (b) XRD patterns of 10 Si: HfO_2 with and without cap (c) Capacitance-Voltage (C-V) of $SiHfO_2$ with cap and without cap (d) Hysteresis loop of Si: HfO_2 with different doping concentration of Si:HfO_2[23].

HZO solid films can be deposited using several types of deposition techniques such as ALD[25], pulsed laser deposition [27], and sputtering[28]. As ALD has a good control of doping with deposition rate so it is one of the most commonly used deposition technique. On the other hand, chemical solution deposition (CSD which is a low-cost film deposition technique provides the opportunity of a wide range of elements. These elements can be used

as dopants and stoichiometry control of films which is easy for CSD. So far, some reports have been published on doped HfO_2 films deposited by CSD [29]–[34]. However, there are limited reports of HZO deposited by CSD. Starschich et al., reported various kinds of dopants in HfO_2. 5% yttrium-doped HfO_2 showed the highest remanent polarization of all examined dopants for HfO_2 films deposited by CSD as shown in Figure 1.14 . In addition, doping of HZO reported by Chernikova et al. results in showing good ferroelectric and endurance properties as compared to undoped HZO films [35].

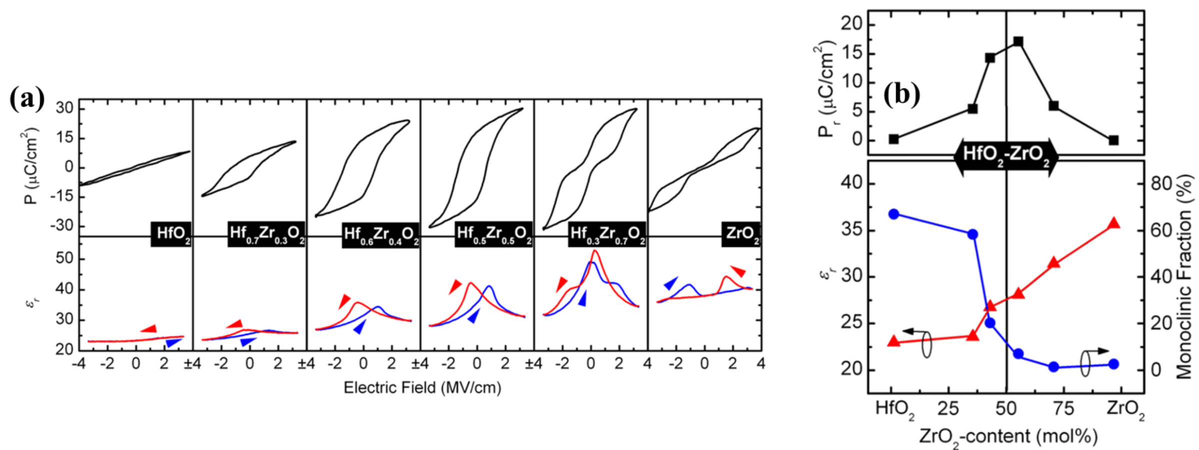

Figure 1.12 (a) Polarization-Electric field (P-E) loops and Capacitance of HZO with ZrO_2 doping centration (b) P_r and ε_r as function of ZrO_2 content. [25]

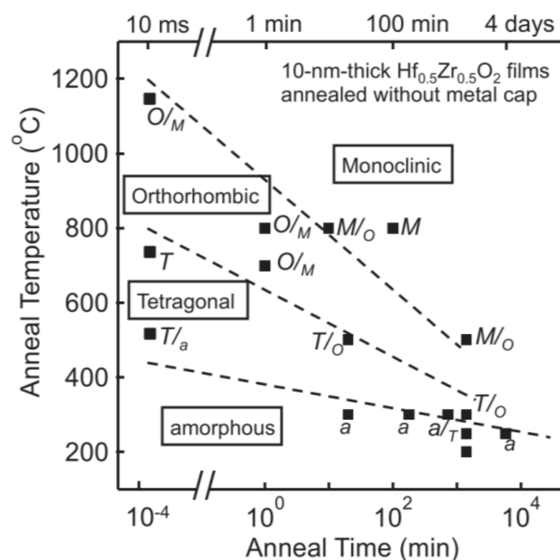

Figure 1.13 Transformation of dominant crystalline phases of 10 nm thick Hf0.5Zr0.5O2 films correlated with the annealing temperature and time in the condition of annealing without metal cap.[28]

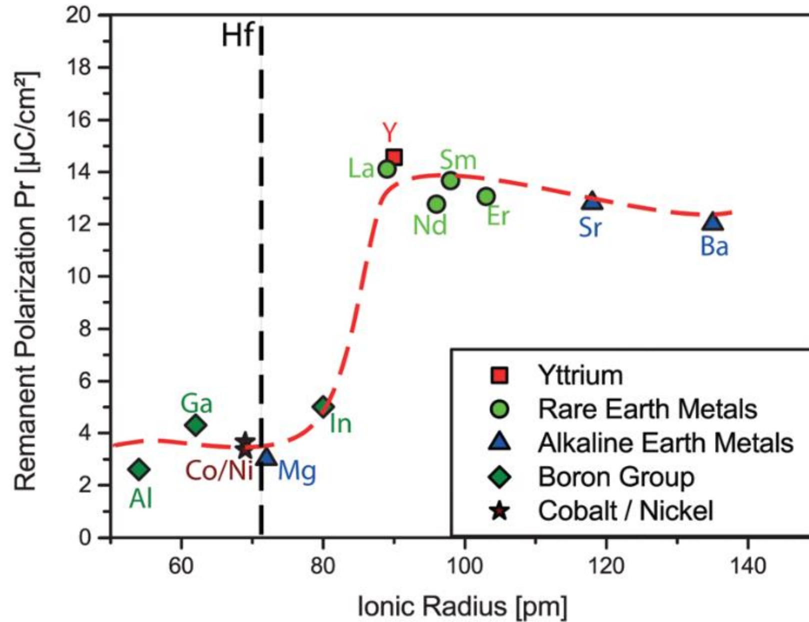

Figure 1.14 P_r as function of ionic radius of various element.[36]

1.5. Oxide channel ferroelectric gate thin film transistor (FGT)

1.5.1. Ferroelectric field effect transistor (FeFET)

Ferroelectric-gate field effect transistors (FeFETs) have a structure in which the gate insulating film of a Si-MOSFET (metal-oxide-semiconductor field-effect transistor) is replaced with a ferroelectric material. In FeFET, the polarization state of the ferroelectric material controls the drain current, and the ON and OFF current can be held by spontaneous polarization as shown in Figure 1.15. Since the ON current and OFF current corresponds to “0” and “1”, the data can be read without destroying it.

However, FeFET has not yet been put into practical use even now, more than 50 years after it was proposed in 1957. This is because SiO_2 interlayer layer forms at the interface between ferroelectric material and Si with poor electrical properties as discussed in the previous section. As a result, long-term data retention has been a long-standing issue for FeFETs. An MFIS (metal-ferroelectric-insulator-semiconductor) structure in which an insulating buffer layer is inserted between the ferroelectric substance and Si has been proposed.This proposed method is to improve the interfacial characteristics [37] and there are reports on long-term data

retention[38], [39]. However, minor loops of the ferroelectric material can only be used that reduces the memory window (MW) (threshold voltage shift).

In order to form a good semiconductor / ferroelectric interface, our research has been focusing on ferroelectric-gate thin film transistor (FGT) using a oxide semiconductor film as a channel. By adopting the bottom gated TFT structure, the ferroelectric substance having a high crystallization temperature can be crystallized first, and the device can be manufactured without the semiconductor / ferroelectric interface undergoing high temperature annealing. Furthermore, it is expected that by depositing oxide semiconductors at low temperature, oxidation does not occur at the interface and a good interface between oxides can be formed.

1.5.2. Operating principle of FGT

FGT with oxide semiconductor as channel material such as In_2O_3 and Indium-Tin-Oxide (ITO) which has generally a wide gap. The ON and OFF state in FGT is due to the accumulated state and depletion state of the semiconductor as shown in Figure 1.15 (if it does not become an inverted state by Fermi level pinning). The above explanation is for the case of the n-type oxide semiconductor channel used in this study, but even if a p-type oxide semiconductor is used, it operates on the same principle by replacing the role of electrons with holes. When a positive voltage is applied to the gate, the channel is in an accumulated state, and the electrons coupled with the polarization of the ferroelectric substance. This leads to large drain current (ON current) flows, and the device is turned on. When a negative voltage is applied to the gate, the channel becomes depleted and almost no current flows (OFF current) as shown in Figure 1.15. Even if the voltage is set to 0, it functions as a non-volatile memory element because it can maintain the accumulated / depleted state due to the spontaneous polarization of the ferroelectric substance. In principle, FGT (also FeFET) is a normally-on device after the positive programming gate voltage is applied, because the ON current continues to flow while the ON state is maintained. FGT can be also a normally off device after the negative programming gate voltage is applied. In this case, almost no current (OFF current) flows when the gate voltage is 0.

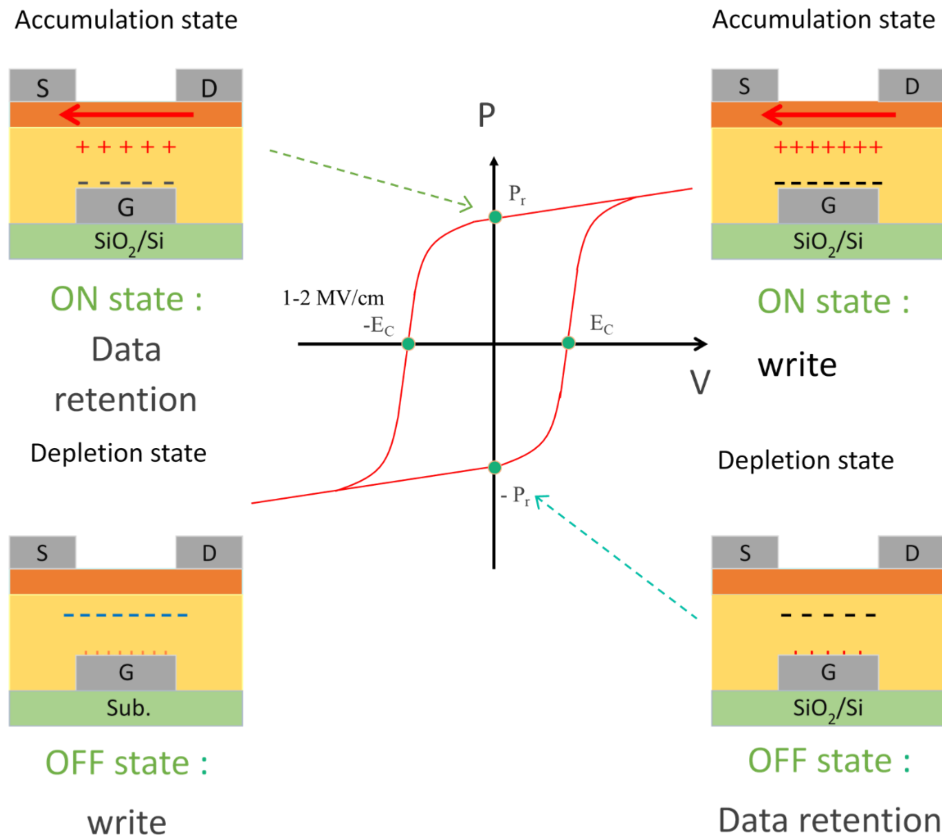

Figure 1.15 Principle operation of FGT

1.5.3. Physical properties of Ferroelectric HfO_2 for FGT

In FGT, the ferroelectric HfO_2 is required to have the following physical properties.

- Remnant polarization (P_r)

As the number of electrons coupled with the polarization of the ferroelectric HfO_2 is directly proportional to the magnitude of the ferroelectric polarization of the ferroelectric HfO_2. Therefore, the ON current of FGT depends on the magnitude of the polarization of the ferroelectric substance. Furthermore, Small OFF current can be obtained if the channel is completely depleted by the large polarization of the ferroelectric substance. Hence, large ON current and a small OFF current can be obtained if the residual polarization value is large enough as shown in Figure 1.16 Typical hysteresis loop of ferroelectric HfO2.

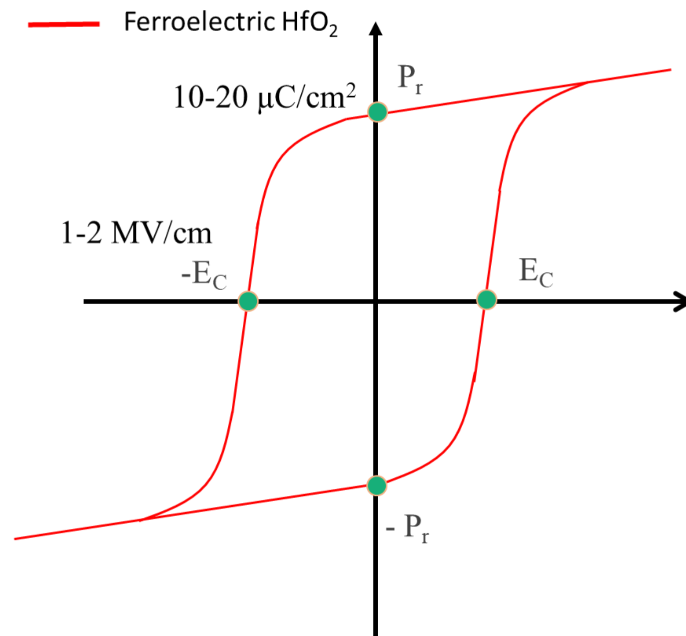

Figure 1.16 Typical hysteresis loop of ferroelectric HfO_2

- Leakage current

The gate leak current degrades the polarization of the ferroelectric substance (will be discussed in later section) and may result in loss of retained data. To ensure the reliability of FGT as a non-volatile memory device with long-term data retention characteristics, a leakage current as small as possible is required.

- Surface flatness

In bottom gated FGT structure, when the channel thickness is thin, better the switching characteristics can be obtained (see chapter 5 for details). In order to form a thin continuous thin film channel, it is desirable that the surface of the underlying ferroelectric HfO_2 thin film is smooth and flat. It is considered that a flat surface can suppress carrier scattering due to surface roughness, which could result in a decrease in channel mobility.

- Rectangularity

Since FGT controls channel accumulation and depletion by polarization of the ferroelectric HfO_2, hysteresis shape of the ferroelectric HfO_2 is directly related in the drain current-gate voltage (I_D-V_G) characteristics. Good rectangularity is required to achieve a small subthreshold voltage swing (SS value) and a large ON / OFF ratio, and to operate FGT at low voltage.

ALD based HfO_2 based FGT with oxide channel deposited by rf sputtering shows almost all the characteristics listed above have been reported [40], [41]. It would be interested to

realize the FGT by solution process where both gate insulator and channel layer by solution process.

1.6. Research objective

Discovery of ferroelectricity in HfO_2 has gain great interest to develop future high density ferroelectric random-access memory (FeRAM) devices. As discuss in previous section, Ferroelectricity in HfO_2 is due to the formation of orthorhombic phase. This phase is considered as metastable phase. It can be stabilized by doping. The most widely used doping elements are Al, Si, Y and Zr. In particular, Zr doped HfO_2 or Hafnium-Zirconium Oxide (HZO) has gained most significant attention because of high remnant polarization with wide doping range. Atomic layer deposition (ALD) and sputtering are usually used to fabricate HfO_2. On the other hand, inexpensive devices can be fabricated by CSD method for various applications at low cost. There are only few reports on CSD for ferroelectric HZO films and doping effect in HZO films by CSD has not been investigated.

The objective of this study is to develop the chemical solution process for HfO_2-based ferroelectric films and to apply them to ferroelectric-gate transistors (FGTs). To realize FGTs, oxide semiconductor or conductor, In_2O_3 or In-Sn-O (ITO) was used as a channel and yttrium doped HZO was used as gate insulator material. To best of my knowledge, thin film transistors (TFTs) using solution processed HZO ferroelectric gate insulator with solution processed In_2O_3 or ITO oxide channel have not been reported.

References

[1] G. Moore, "Moore's Law, Electronics," *Electronics*, vol. 38, no. 8, p. 114, 1965.

[2] J. Valasek, "Piezo-electric and allied phenomena in Rochelle salt," *Phys. Rev.*, vol. 17, no. 4, pp. 475–481, 1921, doi: 10.1103/PhysRev.17.475.

[3] A. Lüker and I. S. Técnico, "A Short History of Ferroelectricity," pp. 1–9, 2000.

[4] G. BUSCH and P. SCHERRER, "Kurze 0riginalmitteilungen.," *Naturwissenschaften*, vol. 23, p. 737, 1933.

[5] H. Thurnauer and J. Deaderick, "Nsulating Materal," vol. 7702, p. 588, 1947.

[6] G. A. SMOLENSKY and V. A. ISUPOV, "New Classes of Ferroelectric S of Displacement Type," *Le J. Phys. Colloq.*, vol. 33, no. C2, pp. C2-25-C2-31, 1972, doi: 10.1051/jphyscol:1972207.

[7] L. Process, "酸化物半導体の 強誘電体メモリ応用と液体プロセスに関する研

究."

[8] C. H. Lin, P. A. Friddle, C. H. Ma, A. Daga, and H. Chen, "Effects of thickness on the electrical properties of metalorganic chemical vapor deposited Pb(Zr, Ti)O3 (25-100 nm) thin films on LaNiO3 buffered Si," *J. Appl. Phys.*, vol. 90, no. 3, pp. 1509–1515, 2001, doi: 10.1063/1.1383262.

[9] J. F. Scott and C. A. Paz De Araujo, "Ferroelectric memories," *Science (80-.).*, vol. 246, no. 4936, pp. 1400–1405, 1989, doi: 10.1126/science.246.4936.1400.

[10] R. Maas, M. Koch, N. R. Harris, N. M. White, and A. G. R. Evans, "Thick-film printing of PZT onto silicon," *Mater. Lett.*, vol. 31, no. 1–2, pp. 109–112, 1997, doi: 10.1016/S0167-577X(96)00249-2.

[11] N. Setter *et al.*, "Ferroelectric thin films: Review of materials, properties, and applications," *J. Appl. Phys.*, vol. 100, no. 5, 2006, doi: 10.1063/1.2336999.

[12] J. Wang, H. P. Li, and R. Stevens, "Hafnia and hafnia-toughened ceramics," *J. Mater. Sci.*, vol. 27, no. 20, pp. 5397–5430, 1992, doi: 10.1007/BF00541601.

[13] R. Ruh, H. J. Garrett, R. F. Domagala, and N. M. Tallan, "The System Zirconia-Hafnia," *J. Am. Ceram. Soc.*, vol. 51, no. 1, pp. 23–27, 1968.

[14] O. Ohtaka, H. Takebe, A. Yoshiasa, H. Fukui, and Y. Katayama, "Phase relations of AgI under high pressure and high temperature," *Solid State Commun.*, vol. 123, no. 5, pp. 213–216, 2002, doi: 10.1016/S0038-1098(02)00290-9.

[15] J. E. Lowther, J. K. Dewhurst, J. M. Leger, and J. Haines, " Relative stability of ZrO2 and HfO2 structural phases ," *Phys. Rev. B*, vol. 60, no. 21, pp. 14485–14488, 1999, doi: 10.1103/physrevb.60.14485.

[16] E. H. Kisi, "Influence of hydrostatic pressure on the t → o transformation in Mg-PSZ studied by in situ neutron diffraction," *J. Am. Ceram. Soc.*, vol. 81, no. 3, pp. 741–745, 1998, doi: 10.1111/j.1151-2916.1998.tb02402.x.

[17] T. S. Böscke *et al.*, "Phase transitions in ferroelectric silicon doped hafnium oxide," *Appl. Phys. Lett.*, vol. 99, no. 11, pp. 10–13, 2011, doi: 10.1063/1.3636434.

[18] R. D. Clark, "Emerging applications for high K materials in VLSI technology," *Materials (Basel).*, vol. 7, no. 4, pp. 2913–2944, 2014, doi: 10.3390/ma7042913.

[19] J. H. Choi, Y. Mao, and J. P. Chang, "Development of hafnium based high-k materials - A review," *Mater. Sci. Eng. R Reports*, vol. 72, no. 6, pp. 97–136, 2011, doi: 10.1016/j.mser.2010.12.001.

[20] X. Zhao and D. Vanderbilt, "First-principles Study of Electronic and Dielectric Properties of ZrO_2 and HfO_2," *MRS Proc.*, vol. 745, p. N7.2/T5.2, Feb. 2002, doi: 10.1557/PROC-745-N7.2/T5.2.

[21] X. Zhao and D. Vanderbilt, "First-principles Study of Electronic and Dielectric Properties of ZrO_2 and HfO_2," *MRS Proc.*, vol. 745, p. N7.2/T5.2, Feb. 2002, doi: 10.1557/PROC-745-N7.2/T5.2.

[22] K. Tomida, K. Kita, and A. Toriumi, "Dielectric constant enhancement due to Si incorporation into HfO 2," *Appl. Phys. Lett.*, vol. 89, no. 14, pp. 2–5, 2006, doi: 10.1063/1.2355471.

[23] T. S. Böscke, J. Müller, D. Bräuhaus, U. Schröder, and U. Böttger, “Ferroelectricity in hafnium oxide thin films,” *Appl. Phys. Lett.*, vol. 99, no. 10, p. 102903, Sep. 2011, doi: 10.1063/1.3634052.

[24] M. H. Park *et al.*, “Ferroelectricity and Antiferroelectricity of Doped Thin HfO2-Based Films,” *Adv. Mater.*, vol. 27, no. 11, pp. 1811–1831, 2015, doi: 10.1002/adma.201404531.

[25] J. Müller *et al.*, “Ferroelectricity in simple binary ZrO2and HfO2,” *Nano Lett.*, vol. 12, no. 8, pp. 4318–4323, 2012, doi: 10.1021/nl302049k.

[26] H. J. Kim *et al.*, “Grain size engineering for ferroelectric Hf0.5Zr0.5O2 films by an insertion of Al2O3 interlayer,” *Appl. Phys. Lett.*, vol. 105, no. 19, pp. 1–6, 2014, doi: 10.1063/1.4902072.

[27] Y. Wei *et al.*, “A rhombohedral ferroelectric phase in epitaxially strained Hf 0.5 Zr 0.5 O 2 thin films,” *Nat. Mater.*, vol. 17, no. 12, pp. 1095–1100, 2018, doi: 10.1038/s41563-018-0196-0.

[28] S. Migita *et al.*, “Phase transformation behavior of ultrathin Hf0.5Zr0.5O2 films investigated through wide range annealing experiments,” *Jpn. J. Appl. Phys.*, vol. 58, no. SB, pp. 0–6, 2019, doi: 10.7567/1347-4065/ab00f6.

[29] S. Starschich, D. Griesche, T. Schneller, and U. Böttger, “Chemical Solution Deposition of Ferroelectric Hafnium Oxide for Future Lead Free Ferroelectric Devices,” *ECS J. Solid State Sci. Technol.*, vol. 4, no. 12, pp. 419–423, 2015, doi: 10.1149/2.0061512jss.

[30] H. Liu *et al.*, “Structural and ferroelectric properties of Pr doped HfO2 thin films fabricated by chemical solution method,” *J. Mater. Sci. Mater. Electron.*, vol. 0, no. 0, p. 0, 2019, doi: 10.1007/s10854-019-00874-4.

[31] Y. Yao *et al.*, “Experimental evidence of ferroelectricity in calcium doped hafnium oxide thin films,” *J. Appl. Phys.*, vol. 126, no. 15, p. 154103, Oct. 2019, doi: 10.1063/1.5117358.

[32] S. Kim and J. Hong, “Ferroelectricity in ultrathin yttrium-doped hafnium oxide films prepared by chemical solution deposition based on metal chlorides and alcohol,” *Ceram. Int.*, vol. 43, no. May 2017, pp. S158–S161, 2017, doi: 10.1016/j.ceramint.2017.05.181.

[33] X. Wang *et al.*, “Ferroelectric yttrium doped hafnium oxide films from all-inorganic aqueous precursor solution,” *Ceram. Int.*, vol. 44, no. 12, pp. 13867–13872, 2018, doi: 10.1016/j.ceramint.2018.04.233.

[34] A. Wei, C. Chen, L. Tang, K. Zhou, and D. Zhang, “Chemical solution deposition of ferroelectric Sr:HfO2 film from inorganic salt precursors,” *J. Alloys Compd.*, vol. 731, pp. 546–553, Jan. 2018, doi: 10.1016/j.jallcom.2017.09.264.

[35] A. G. Chernikova *et al.*, “Improved Ferroelectric Switching Endurance of La-Doped Hf0.5Zr0.5O2 Thin Films,” *ACS Appl. Mater. Interfaces*, vol. 10, no. 3, pp. 2701–2708, Jan. 2018, doi: 10.1021/acsami.7b15110.

[36] S. Starschich and U. Boettger, “An extensive study of the influence of dopants on the ferroelectric properties of HfO2,” *J. Mater. Chem. C*, vol. 5, no. 2, pp. 333–338, 2017, doi: 10.1039/c6tc04807b.

[37] J. Journal and A. P. Related, "Electrical Properties of Metal-Ferroelectric- Insulator-Semiconductor (MFIS) - and Metal- (MFMIS) -FETs Using Ferroelectric SrBi 2 Ta 2 O 9 Film and SrTa 2 O 6 / SiON Buffer Layer," 2000.

[38] X. Lu, J. W. Yoon, and H. Ishiwara, "Low-voltage operation and excellent data retention characteristics of metal-ferroelectric-insulator-Si devices based on organic ferroelectric films," *J. Appl. Phys.*, vol. 105, no. 8, pp. 1–5, 2009, doi: 10.1063/1.3097691.

[39] H. Saiki and E. Tokumitsu, "Data retention and readout degradation properties of Pt/Sr 0.7Sm0.07Bi2.2Ta2O 9/HfO2/Si structure ferroelectric-gate field effect transistors," *Japanese J. Appl. Physics, Part 1 Regul. Pap. Short Notes Rev. Pap.*, vol. 46, no. 1, pp. 261–266, 2007, doi: 10.1143/JJAP.46.261.

[40] F. Mo *et al.*, "Experimental Demonstration of Ferroelectric HfO2 FET with Ultrathin-body IGZO for High-Density and Low-Power Memory Application," *Dig. Tech. Pap. - Symp. VLSI Technol.*, vol. 2019-June, pp. T42–T43, 2019, doi: 10.23919/VLSIT.2019.8776553.

[41] M. Si *et al.*, "Indium-Tin-Oxide Transistors with One Nanometer Thick Channel and Ferroelectric Gating," *ACS Nano*, vol. 14, no. 9, pp. 11542–11547, 2020, doi: 10.1021/acsnano.0c03978.

Chapter 2
Experimental details

2. Experimental details

2.1. Deposition methods of ferroelectric HfO_2

2.1.1. Atomic Layer Deposition (ALD)

During mid-1970s, the ALD technique was commercialized by Suntola et al. in Finland [1]. Initially ALD was developed for fabrication of flat panel display using thin film electroluminescent (TFEL) technology. However now-a-days it is widely utilized for other several industrial related applications, such as production of semiconductor device [1], [2]. ALD is the sub-class of deposition technique, well known as chemical vapor deposition (CVD). It can be referred as "cyclic process" to deposit thin film material such as oxide or metals. In ALD, self-terminating gas – solid reactions occurs between two or more reacting elementals in a sequential manner [3]. Two or more chemical precursors are introduced to substrate surface individually. After saturation, each precursor forms a monolayer of material. The working principle is related to separation and self-termination of reactions as shown in figure 2.1. These reactions will proceed until appropriate sites are present on the substrates for reactant [2]. Most common inert carrier gas or purge gas used in commercial ALD is N_2 at 1 mbar. Figure 2.1 shows schematic of ALD cycle, at first chemical precursors are introduced into the flowing purge gas with short pulses, which are separated by using evacuation periods [2]. A specified amount, typically a monolayer of about 1 Å, of the thin film material is grown in each ALD cycle (pulse of precursor 1 – purge – pulse of precursor 2 – purge). Typical cycle times are from one second to several seconds and process temperatures range from room temperature to over 500 °C.

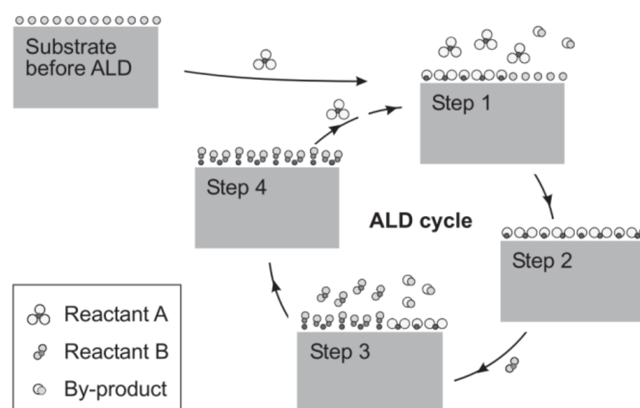

Figure 2.17 Schematic illustration of an ALD reaction cycle [2].

Most ALD processes operate between 200 °C and 400 °C. ALD have several benefits such as good control over the film thickness and deposition rate typically 0.1- 1 Å per second with the ability to deposit high aspect ratio structures with conformal material layers of high quality. As a result, ALD is main deposition method for deposition of HfO_2 in commercial semiconductor manufacturing process [4]. ALD HfO_2 films is a deposited by same way as described above. ALD has good control of doping concentration in HfO_2 during cycles. As mention in section 1.4.3, ferroelectricity is due to orthorhombic phase (O-phase) which can be stabilized by doping element. ALD has good control of dopant introduction during cycles which makes it main choice for deposition of ferroelectric HfO_2, too. However, ALD has several limitations such as deposition rate is very slow.

2.1.2. Sputtering

Figure 2.2 shows Schematic of sputtered system. Atoms are ejected from a source material in physical sputtering process due to impinging energetic particles. At a reduced pressure in a chamber, sputter deposition takes place. A sealed system which comprises of vacuum chamber and vacuum pump such as rotary pump (RP) and turbo molecular pump (TMP) are used to realize low background pressure. Generally, metal or metal oxide of desired material used as target which affixed towards face the substrate where thin film deposition take place uniformly. Sputtering gas which is usually a inert gas argon (due to low reactivity and results in high sputter yield) is introduced into the chamber and appropriate pressure value or flow rate of Ar is set which is called as process pressure. A negative potential is applied to target which acts as cathode. The electrons present in the chamber will be accelerated away from cathode due to electric field. The electrons collide with the gas molecules before being collected at the ground chamber walls. Through these collisions, electron-ion pairs are created at high electric field. As a result, a weak ionized gas is formed (less than 1 %), which is called as plasma (from hereafter). Electric field accelerates the Ions from the plasma are accelerated across the target sheath to impinge onto the target and results in bombardment between atoms within the target surface region. But some of the atoms bombard within the target and recoil towards the target surface. Atoms (as well as secondary electrons, ions etc.) are emitted from the target and process is known as physical sputtering. These atoms in the chamber move towards the substrate and results in formation a uniform thin film of desired target material. Therefore, this method is also known as physical vapour deposition (PVD). Sputtering have two different types

based on source power used, that is RF sputtering is which works in alternating current (AC) mode, while in case of DC sputtering operates using DC mode. DC sputtering is mostly employed for deposition of conductive materials such as metals or alloys but non-conductive materials such as dielectrics cannot be deposited. At first, +vely charged argon gas ions can be accelerated and collide with the target. Atoms which are ejected from target materials are easily deposited onto the substrate. It is a cheaper and feasible option when dealing with large substrate quantities and sizes.

On the other hand, limitation of DC sputtering can be overcome by RF (Radio Frequency). RF sputtering can be employed for both conductive and non-conductive materials. RF sputtering process involves two steps. In the first cycle, the target material is negatively charged which results in polarization of atoms and Ar gas atoms are attracted towards cathode where they eject target material atoms. Ionized Ar gas ions remain on surface of source material due polarized nature od source material atoms. In the next or second cycle, cathode polarization is reverse by applying negative voltage to it, as a result Ar ions with target atoms are emitted towards substrate.

Sputtering has several advantages like high deposition rates, ease of sputtering any metal, alloy, or compound, high-purity films, ability to coat heat-sensitive substrates, ease of automation with excellent uniformity on large-area substrates. Sputtering has fast deposition rate as compared to ALD. Due to all these advantages, sputtering is another candidate for deposition ferroelectric HfO_2. There are various research on ferroelectric HfO_2 films deposited by sputtering [5]–[9]. However, sputtering has some disadvantages such as high cost (new compound target should be bought separately for each doping concentration). In addition, as shown in this thesis, ferroelectricity of sputtered HfO_2 films is very unstable against the re-annealing process. This will be discussed in chapter 4.

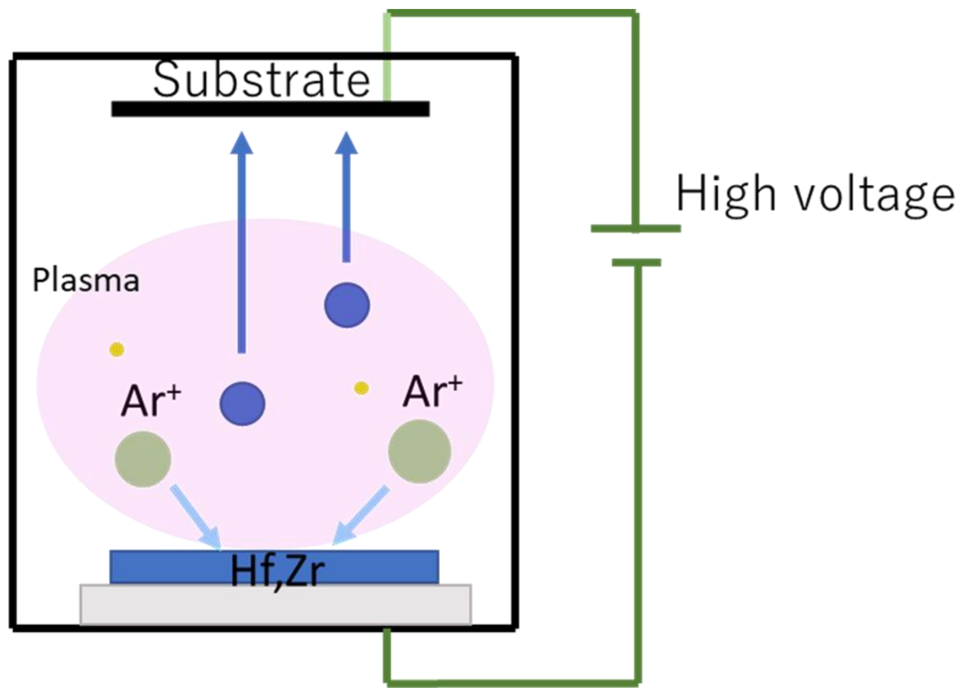

Figure 2.2 Schematic of sputtered films

2.1.3. Chemical Solution Deposition (CSD)

CSD is a deposition technique in which the film is formed due to pyrolysis of the solution [10]. This method is named following the name 'chemical vapor deposition'. CSD is a soft solution-processing method. It is carried out using a simplified experimental setup under atmospheric pressure and a temperature below 373 K[10].

The simple CSD can be employed to materials requires low processing temperature such as polymer-based films, complicated and different shape substrates, and porous materials. Therefore, CSD can be used to a low-cost and environmentally friendly coating process. Figure 2.3 shows, general CSD process for thin films. The fabrication of thin films begins with the preparation of appropriate source or precursors solution which are often metal-organic compounds such as acetylacetonate or alkoxides, or carboxylates [11]. These precursors are dissolved using suitable solvent such as DMSO (Dimethyl Sulfoxide), 2MeOH (Methonal), and PrA (Propionic acid). There are three kinds of techniques for CSD thin film deposition such as spin coating (rotating substrate), dip coating (dipping the substrate in the solution), and spray coating (misted solution) as shown in figure 2.3. The spin coating is the most conventional technique employed for CSD due to ease of fabrication. Therefore, CSD starts with spin coating source to form wet film. Wet film has lots of organic which are removed by

drying and pyrolysis. The "pyro" is Greek word which mean "heat". The decomposition of organics using indirect heat under air or oxygen is known as pyrolysis. The transformation of the wet film into the crystalline film is achieved by controlled thermal processes, which generally carried by using a hot plate or conventional furnace, or a rapid thermal annealing (RTA) system. Precise control of the deposition conditions are necessary to form uniform coating of thin films. [11]. There are several requirements that need to be fulfilled by the solution chemistry, substrates, and processing conditions for effective implementation of the CSD technique. These include:

- formation of a stable precursor solution with adequate solubility of the precursors in the solvent is necessary.
- synthesis of precursors that decompose without unwanted residual during thermal treatment, i.e., all of the elements except the cations (and oxygen ions) must be released into the gas phase during pyrolysis or thermal process.
- Thin film should not have non- uniformities or crack formation during pyrolysis or crystallization.
- Source solution should have enough long-term stability to avoid non-reproducible film properties.

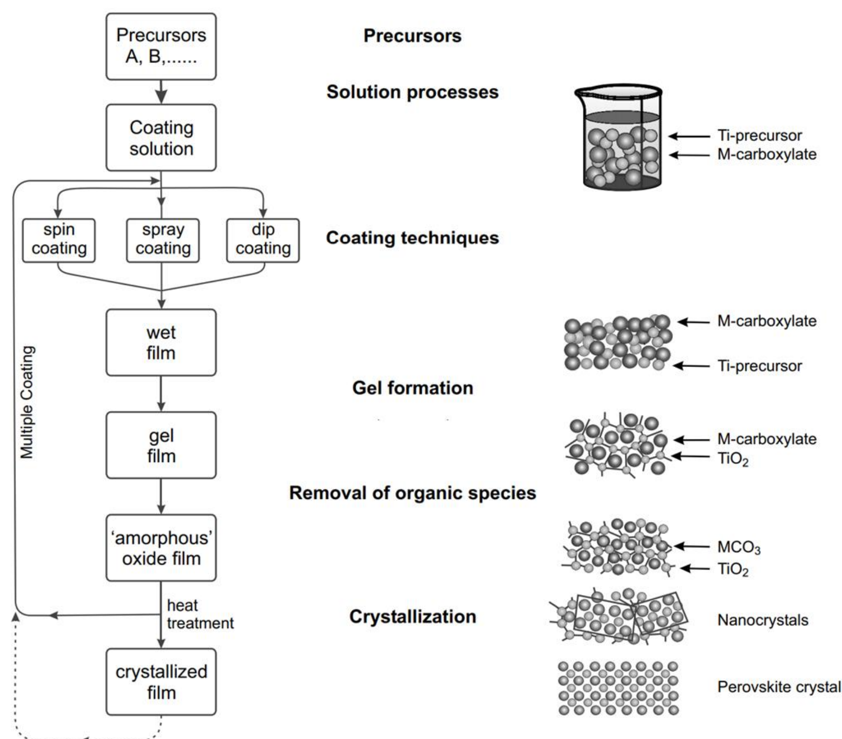

Figure 2.3 General CSD process for fabrication of thin films [11].

Ferroelectric HfO_2 films deposited by ALD and sputtering has several drawbacks such low deposition rate, high cost and sophisticated instrument. At the other side, the chemical solution deposition (CSD) method is good in fabricating inexpensive devices for a wide range of applications at low cost. In addition , various dopants can be used for films deposited by CSD for the comparative study of doping elements with ease [12], [13]. Table 1 shows previous studies on ferroelectric HfO_2, most of studies requires glove box which makes the process little bit complex. Some reports on CSD ferroelectric HfO_2 where precursor was prepared in air showed rounded polarization-electric filed (P-E) loops [14], [15].There are a few reports on CSD Hafnium-Zirconium oxide (HZO) with clear hysteresis loops but requires glove box. In addition, metal cap or post metallization annealing (PMA) is requires to stabilize the O-phase. On contrary, in this work, we prepare Y-HZO solution in air and the details will be discussed in section 2.2.1 and ferroelectricity is observed without metal cap or PMA which will be discussed in chapter 3.

Table 2.1: Comparison with previous work on HfO_2 based ferroelectric films prepared by CSD

Dopant	precursor	Solution preparation environment	Annealing environment	P-E loop and butterfly shape	Ref.
Y	$Hf(acac)_4$	Glove box	argon/oxygen	Clear hysteresis with clear butterfly loop	[13]
Pr	$Hf(acac)_4$	air	oxygen	Rounded loop and clear butterfly shape	[14]
Y	$HfCl_4$	air	N_2	Rounded loop	[15]
Sr	$HfCl_4$	Glove box	N_2	Rounded loop	[16]
La	$Hf(O\text{-}i\text{-}C_3H_7)_4$	Glove box	N_2	Clear hysteresis	[17]
HZO	$Hf(O\text{-}i\text{-}C_3H_7)_4$	Glove box	N_2	Clear hysteresis at low temperature.	[18]
HZO	$Hf(O\text{-}i\text{-}C_3H_7)_4$	Glove box	N_2	Clear hysteresis	[19]
This Work	$Hf(acac)_4$	air	Vacuum	Clear hysteresis with clear butterfly loop	-----

2.2. General process for fabrication of ferroelectric Y-HZO and oxide semiconductor thin films by Chemical solution process

2.2.1. Substrate cutting and cleaning

A platinized silicon wafer ($Pt/Ti/SiO_2/Si$) were bought from Tanaka Precious Metals. They were cut into substrates with dimensions of 1.5×1.5 cm^2 using a diamond pen cutter, which were also used to deposit thin films. Substrates were cleaned using standard cleaning procedure. At first, substrate for cleaning acetone for 10 min, followed by IPA for 10 mins and finally deionized water (DI water) for 10 min. Followed by N_2 air gun blow and drying on hot plate at 110 ^oC for 5 min to remove water. Substrate were cleaned again using the same procedure, just before deposition of thin films to avoid any dust and other particles.

2.2.2. Preparation of precursor solution

At first, precursor solution of ferroelectric, 5 % Yttrium doped Hafnium Zirconium Oxide (Y-HZO) was prepared. Precursor solution of Y-HZO was prepared using hafnium (IV) acetylacetonate ($Hf(acac)_4$), zirconium (IV) acetylacetonate ($Zr(acac)_4$), and yttrium (III) acetylacetonate ($Y(acac)_3$) as starting materials. Precursor solution was prepared in the air. $Hf(acac)_4$, $Zr(acac)_4$, and $Y(acac)_3$ were added to propionic acid with concentration of 0.3 mol/kg. The Precursor solution was mixed using magnetic stirrer at 1000 rpm at 120 ^oC for 1 hour. Y-HZO source solution was left 12 hours ageing or cool before filtering through 0.2 μM size pore syringe filter. It is worth noting that solution remain stable over 1 year. Figure 2.4 show Y-HZO solution prepared on 02/11/2018 and clear show no precipitation at bottom which means solution stable. The photograph was taken on 09/11/2020. Acetylacetonate is well known as stabilizer and it makes Y-HZO highly stable.

Next, precursor solution of oxide semiconductor channel In_2O_3 and Indium-Tin-Oxide (ITO) was prepared. Precursor solution of In_2O_3 was prepared using indium(III) acetylacetonate ($In(acac)_3$) as starting material. $In(acac)_3$ was added to PrA and magnetic stirrer at 1000 rpm at 120 ^oC for 1 hour. The solution concentration varied from 0.025 to 0.3 mol/kg to control

thickness which will be discussed in chapter 5. Precursor solution was left for overnight cooling and filtered through 0.2 μM size pore syringe filter. Indium acetylacetonate (In(acac)$_3$) and tin acetylacetonate (Sn(acac)$_2$) as starting material are used to prepare precursor solution of 7.5 % tin doped indium oxide (ITO). In(acac)$_3$ and Sn(acac)$_2$ were mixed in PrA and stirred using magnetic stirrer at 1000 rpm for 1 hour at 120 ^{o}C. The solution concentration of ITO also varied from 0.025 to 0.3 mol/kg to control thickness which will be discussed in chapter 5. Precursor solution of ITO was filtered through 0.2 μM size pore syringe filter.

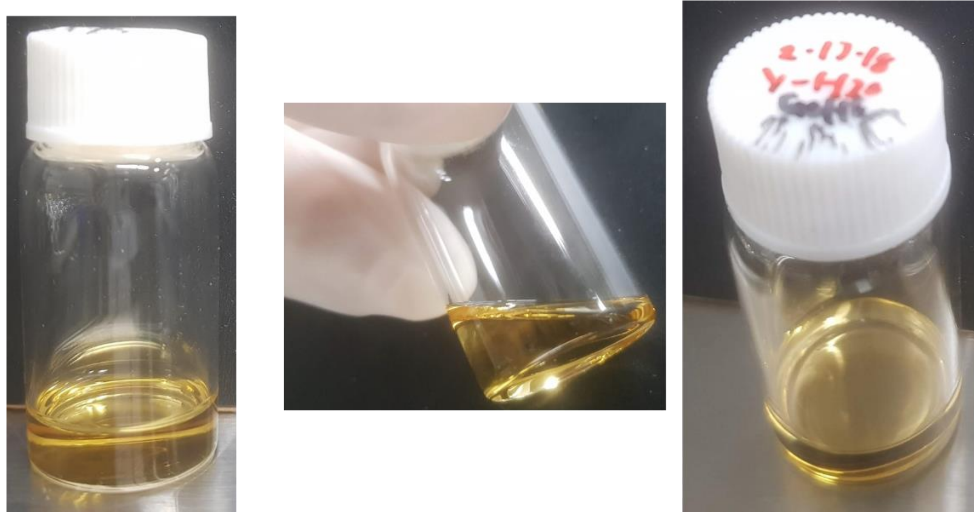

Figure 2.4 Precursor solution of Y-HZO after 2 years.

2.2.3. Deposition of thin films

2.2.3.1. Deposition of Y-HZO films

After cleaning the substrate and preparing precursor solution using starting material and mixing in PrA as described in section above, ~~and~~ the film was deposited by spin-coating as shown in figure 2.5 (a) and (b). Precursor solution was spin coated on platinized substrate at 3000 rpm for 120 s as shown in figure 2.5 (c). After depositing Y-HZO films, wet films were dried on hot plate at 225 ^{o}C for 3 min to form solid films as shown in figure 2.5 (d).

2.2.3.2. Deposition of oxide semiconductor In_2O_3 and ITO

After crystallization of Y-HZO (will be discussed in chapter 3), source solution of In_2O_3 and ITO was deposited on Y-HZO and spin coated at 3000 RPM for 20 sec as shown in figure 2.5 (c). Wet thin film of In_2O_3 and ITO was dried at 100 ^{o}C for 3 min on hot plate to make gel film.

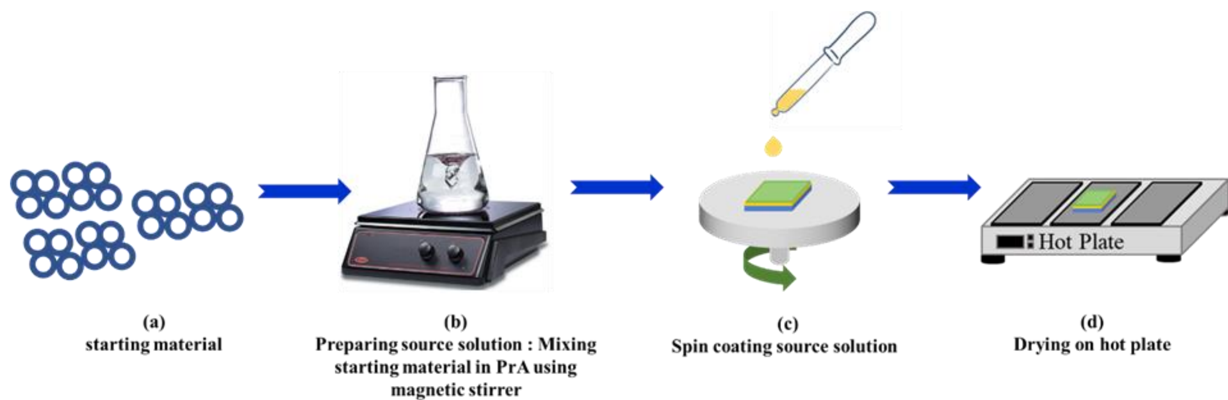

Figure 2.5 Chemcial solution deposition process for deposition of thin films.

2.3. Analytical methods

2.3.1. X-ray diffraction

Most of materials are made of small crystal. Each of these crystals are composed of regular arrangement of atoms with the repeated structure. The physical size of unit cells in crystal structure is referred as lattice parameter. The most well-known way to identify the lattice parameter of a crystal structure is X-ray diffraction (XRD) method using Bragg's law (equation 1). X-rays are high energy light with repeating period called the wavelength. Since the wavelength of an X-ray is similar to the distance between the atoms in a crystal, a special interference effect called diffraction. It can be used to measure the distance between the atoms. Interference occurs when x-ray interact with each other. If waves are in alignment, the signal is amplified. This is called constructive interference. If signals are out of alignment and signal is destroyed. This is called destructive interference. When X-ray encounters an atom, its energy is adsorbed by the electrons. Electrons occupy special energy states around the atom. Since this is not enough energy for electrons to be released, the energy must be re-emited in the form of a new X-ray. But the same energy as the original. This process is called elastic scattering. In a crystal, the repeating arrangement of atoms form distinct planes separated by well-defined distances as shown in figure 2.6. When the atomic planes are exposed to an X-ray beam. X-rays are scattered by regularly spaced atoms. Strong amplification of emitted signal occurs at very specific angles where the scattered waves constructively interfere. This is called diffraction. The angle between the incident and the scattered beam called 2θ. In order for constructive interference to occur. The scattered wave must be in alignment meaning that second wave must travel a whole number of wavelengths. In this case, one half of wavelength

is travelled on the incident side, and one half on the scattered side, yielding one additional wavelength. In the case of the next X-ray, wavelength has travelled on the both the incident and scattered side resulting in two wavelengths. This reinforcement occurs throughout the crystal. The exact angle at which diffraction occurs will be determined by triangle as shown in figure 2.6. The angle at the top is θ, half the angle between the incident and scattered beams. The long side is the distance (d) between the atomics planes and short side we know is one half of a wavelength. The relationship between the diffraction angle, and the spacing between the atoms can be determined by sine function. Re-arranging the equations gives an equation 1 which is commonly known as bragg's law equation.

$$d = n\lambda / 2\sin(\theta) \ldots (1)$$

The crystalline structure of Y-HZO, In_2O_3 and ITO was measured with XRD measurement using PANalytical X'Pert Pro system. The voltage and current were set as 45 kV and 40 mA, respectively, with CuKα radiation at the wavelength of 1.5406 Å in steps of 0.01 of θ − 2θ scan mode..

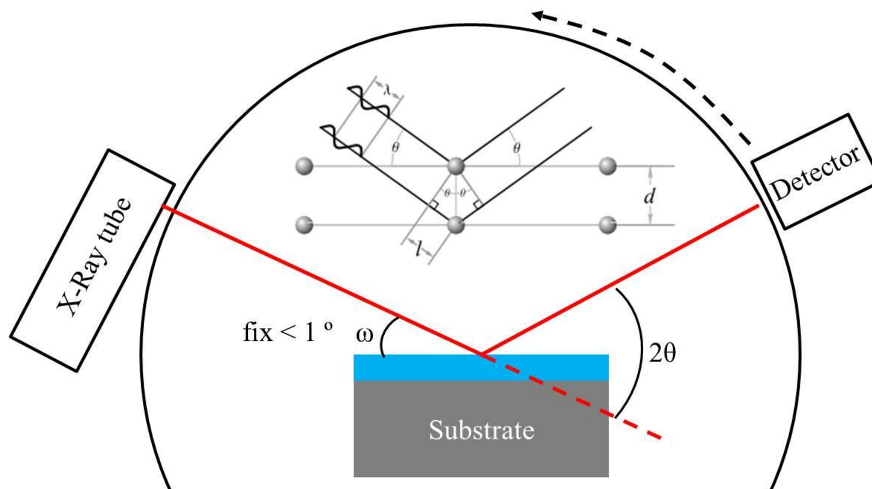

Figure 2.6 Schematic of XRD.

2.3.2. XPS

The method of detecting an interaction between photon and atom of sample (referred as photoionization) and evaluation of the kinetic energy of the radiated photoelectrons is called as photoelectron spectroscopy. Ionization of sample is done by using high-energy radiation

monochromatic source such as X-ray as shown in figure 2.7. Therefore, referred as X-ray photoelectron spectroscopy (XPS). XPS can be employed to identify electronic state and chemical composition close to the surface region (less than 10 nm). At first, X-ray is absorbed inside surface and followed by ionization along with the ejection of a core (inner shell) electron take place according to the following equation (eq.2):

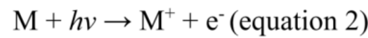

$$M + hv \rightarrow M^{+} + e^{-} \text{ (equation 2)}$$

where h: Planck constant, v: frequency, M (atom), e: electron.

According to rule of the conservation of energy, equation can be rewritten as below (equation 3):

$$E(M) + hv = E(M^{+}) + E(e^{-}) \text{ (equation 3)}$$

The equation 3 can be transformed into equation 4, since energy of electron can be represented with kinetic energy

$$KE = hv - [\mathbf{E(M^{+}) - E(M)}] = hv - \mathbf{BE} \text{ (equation 4)}$$

Binding energy [BE] of electrons represented by indicated brackets as shown in equation 4. As stated in equation 4, BE is difference in energy between the ionized and neutral atoms. Due to each core atomic orbital, there is a specific binding energy for every element. It indicates that any detected electrons provide a specific fingerprint of the atomic species[19].

In my experiment, the XPS was conducted using an AXIS ULTRA as shown in figure 2.8 with a monochromatic Al Kα (1486.7 eV) X-ray source for Y-HZO.

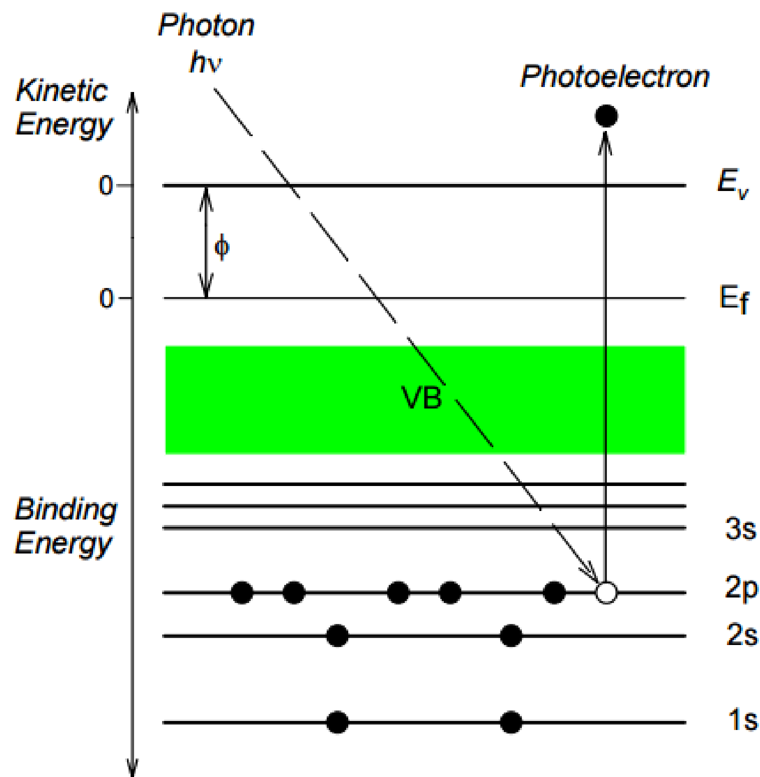

Figure 2.7. Schematic for the generation of energy difference by the photoemission.

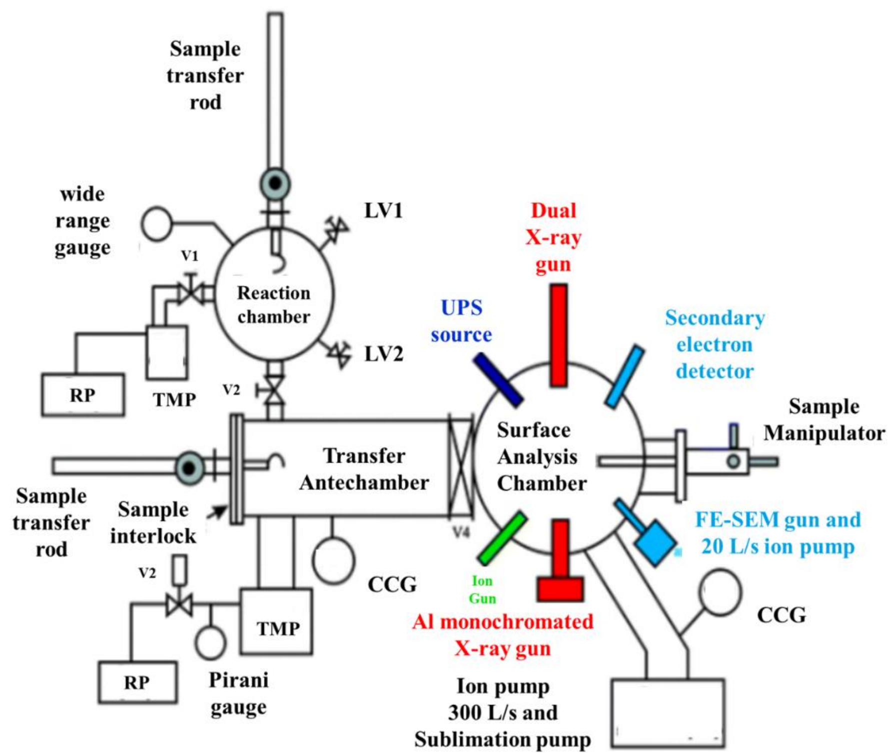

Figure 2.8. Schematic of the Kratos Axis Ultra XPS system.

2.3.3. SEM

A scanning electron microscope (SEM) is a high-resolution microscope for imaging surface of samples beyond limit of conventional microscope such as optical microscope. In SEM, Image of sample surface is generated by indenting electron beam of high energy (generally 0.1 to 50 keV). As a result, electrons are ejected from outer shell of atom in the sample. But some electrons originates from surface due to inelastic scattering between sample and electron beam. Generally these electrons are have low energy >50 eV and referred as secondary electrons (SE). On the other, some electrons originate from inside the sample due to elastic scattering between electron beam and sample atoms. These electrons are called back scattered electron with much higher energy than SE. Generally, SE are detected from the sample by using SE detector to produce image of sample.

SEM microscope is used to identify an electron by scanning the surface using electron beams. Due to high electron beam energy, the samples in measurement are damaged. The scattered electrons are used by SEM. These scattered electrons are further divided as backscattered, secondary electrons in SEM. The scattered electrons are accumulated and counted to produce the image. The SEM also focuses on surface morphology of the sample. Figure 2.9 shows the standard layout of an SEM, which encompasses the electron gun (electron source and accelerating anode), electromagnetic lenses to focus the electrons, a vacuum chamber housing the specimen stage, and a selection of detectors to collect the signals emitted from the specimen [20]

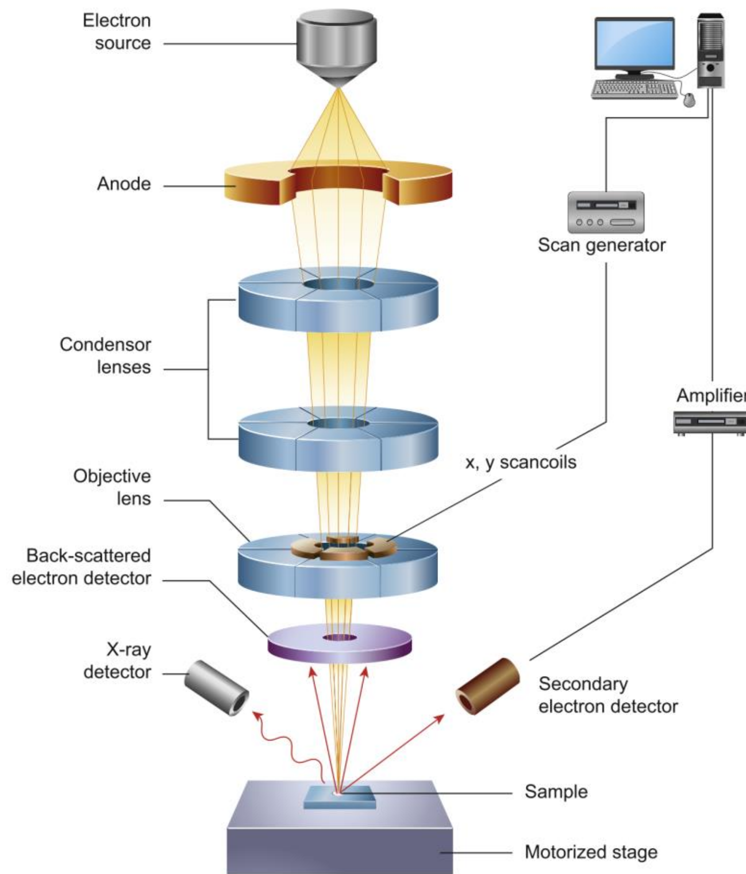

Figure 2.9 Schematic diagram of the core components of an SEM microscope [20].

2.3.4. AFM

Atomic Force Microscopy (AFM) is a high-resolution imaging technique which belongs to class of scanning probe microscopy (SPM). AFM has resolution of few nanometer and able to characterize the three-dimensional surface morphology of material by detecting the atomic force acting on the probe and sample as shown in figure 2.10. AFM uses sharp cantilever tips made of either silicon nitride or silicon with radius of a few nanometer. Force between AFM cantilever tip and surface of sample is governed by van der waal force which increases with decreasing the distance between sample and tip. Figure 2.10 represents dependency of the force curve with respect to the distance between the cantilever tip and the surface of the sample.

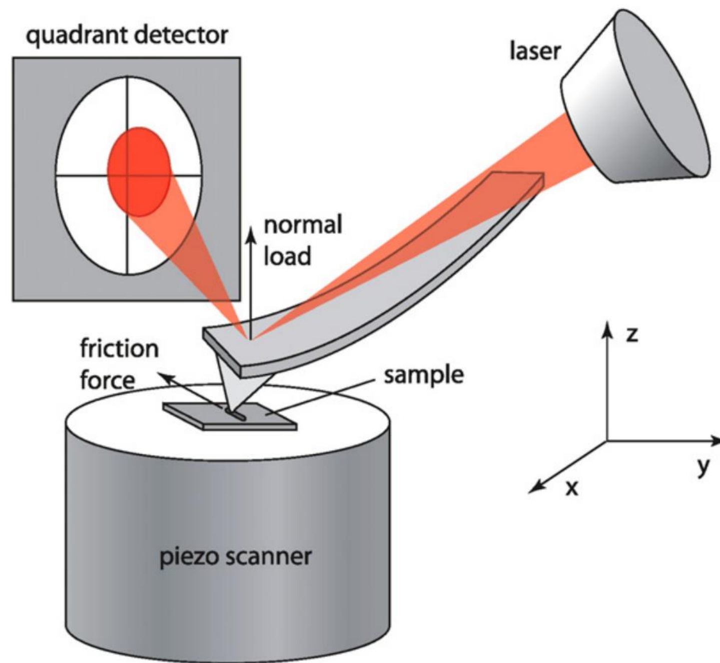

Figure 2.10. Schematic diagram of AFM [21].

AFM has two type of scan mode namely non-contact and contact. In the case of the non-contact mode, AFM cantilever remains close to sample surface with gap of 10 to 100 Å. Sample surface image is acquired by detecting movement of cantilever forward and backward direction on sample, using quadrant detector. The force induced on the cantilever mostly related to height profile of sample surface. In addition, Piezoelectric crystal with small IC employed to keep the height constant (therefore, a constant force). Laser is incident on back of the cantilever and change in the position of reflected laser is detected by photosensitive detector as shown in figure 2.10. As a result, difference in height on the sample is calculated

On the other hand, in case of contact mode AFM, cantilever tips maintain constant contact with sample. Therefore, Cantilever tip and sample surface are close proximity (less than few Å) due to repulsive force is used as shown in figure 2.11. While in case of non-contact AFM mode, attractive forces are dominant which are originated by long range van der Waals interactions.

In my experiment, the AFM is used for the observation of surface morphology of Y-HZO film using AFM5000II SPA-400, Hitachi in dynamic force microscope mode.

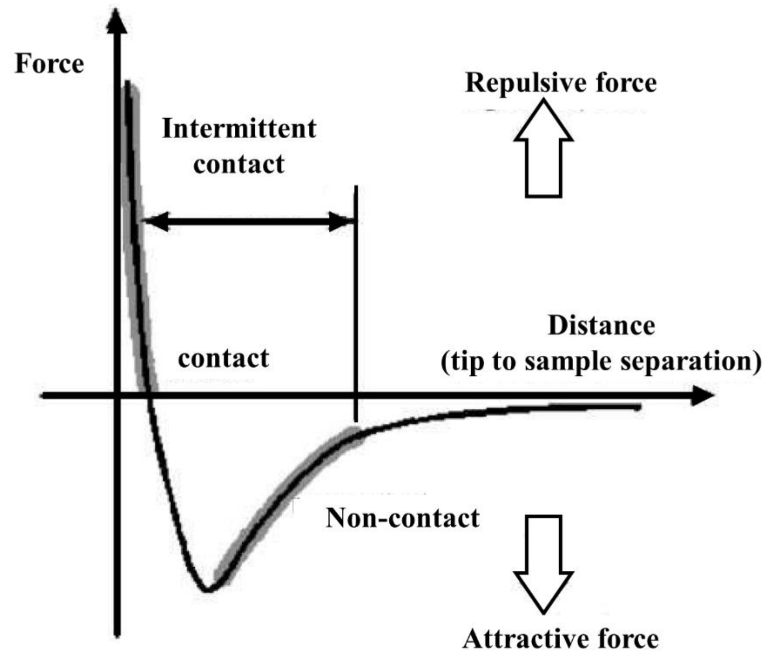

Figure 2.11 Force curve of AFM

2.3.5 Electrical measurements

The polarization–electric field (*P*–*E*) with current–electric field (I_s–*E*) characteristics of all samples was measured by a ferroelectric test system (TOYO Corporation model FCE-1) at 1 kHz, whereas capacitance–voltage (*C*–*V*) measurements were achieved using a precision component analyzer (Wayne Kerr 6440B model) at 10 kHz as shown in fig 12 (red square). The current density–voltage (*J*–*V*) curves, Output characteristics (I_d-V_d) and transfer characteristics (I_d-V_g) were acquired with a semiconductor parameter analyzer (Agilent 4155B) as shown in figure 2.12 (blue square) .Hall measurement system used was RESITEST 8400 by Toyo corp.

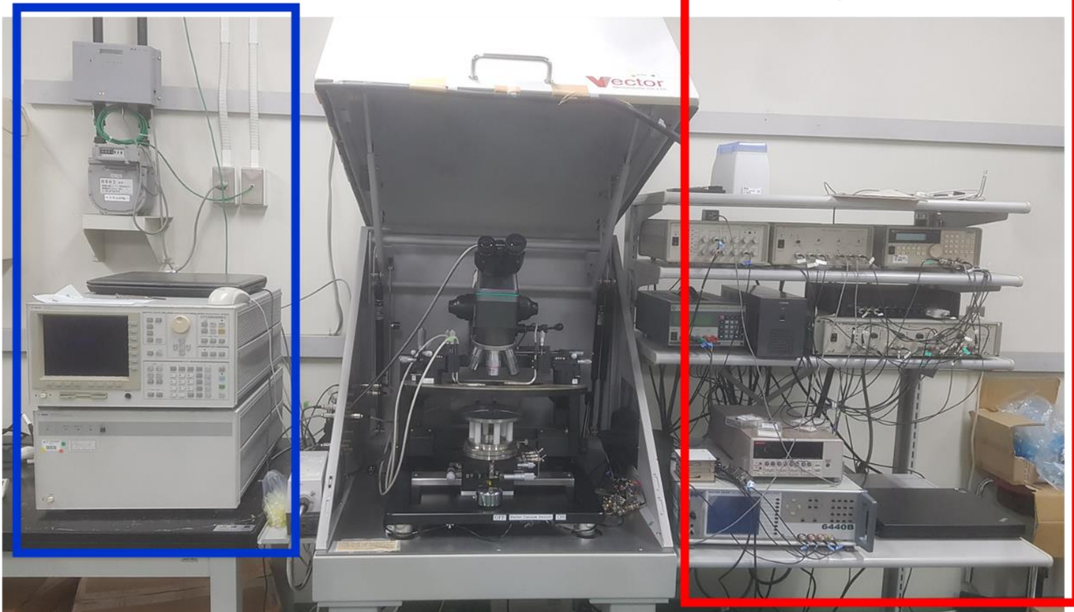

Figure 2.12 Ferroelectric measurement system and FGT parameter analyzer.

References.

[1] J. Antson, “United States Patent (19),” *Geothermics*, vol. 14, no. 19, pp. 595–599, 1977.

[2] R. L. Puurunen, H. Kattelus, and T. Suntola, *Atomic Layer Deposition in MEMS Technology*. Elsevier Inc, 2010.

[3] S. M. George, “Atomic layer deposition: An overview,” *Chem. Rev.*, vol. 110, no. 1, pp. 111–131, 2010, doi: 10.1021/cr900056b.

[4] R. D. Clark, “Emerging applications for high K materials in VLSI technology,” *Materials (Basel).*, vol. 7, no. 4, pp. 2913–2944, 2014, doi: 10.3390/ma7042913.

[5] T. Shimizu *et al.*, “The demonstration of significant ferroelectricity in epitaxial Y-doped HfO2film,” *Sci. Rep.*, vol. 6, no. August, pp. 1–8, 2016, doi: 10.1038/srep32931.

[6] T. Shimizu *et al.*, “Contribution of oxygen vacancies to the ferroelectric behavior of Hf0.5Zr0.5O2 thin films,” *Appl. Phys. Lett.*, vol. 106, no. 11, Mar. 2015, doi: 10.1063/1.4915336.

[7] T. Mimura *et al.*, “Effects of heat treatment and in situ high-temperature X-ray diffraction study on the formation of ferroelectric epitaxial Y-doped HfO_2 film,” *Jpn. J. Appl. Phys.*, vol. 58, no. SB, p. SBBB09, 2019, doi: 10.7567/1347-4065/aafed1.

[8] X. Tian, S. Shibayama, T. Nishimura, T. Yajima, S. Migita, and A. Toriumi, “Evolution of ferroelectric HfO2in ultrathin region down to 3 nm,” *Appl. Phys. Lett.*, 2018, doi: 10.1063/1.5017094.

[9] S. Migita *et al.*, “Phase transformation behavior of ultrathin Hf0.5Zr0.5O2 films investigated through wide range annealing experiments,” *Jpn. J. Appl. Phys.*, vol. 58, no. SB, pp. 0–6, 2019, doi: 10.7567/1347-4065/ab00f6.

[10] S. Hiromoto, “Chemical solution deposition of hydroxyapatite and octacalcium phosphate coatings for magnesium and its alloys to improve biocompatibility,” in *Surface Modification of Magnesium and Its Alloys for Biomedical Applications*, vol. 2, T. S. N. S. Narayanan, I.-S. Park, and M.-H. B. T.-S. M. of M. and its A. for B. A. Lee, Eds. Woodhead Publishing, 2015, pp. 60–80.

[11] R. W. Schwartz, T. Schneller, and R. Waser, “Chemical solution deposition of electronic oxide films,” *Comptes Rendus Chim.*, vol. 7, no. 5, pp. 433–461, 2004, doi: 10.1016/j.crci.2004.01.007.

[12] S. Starschich and U. Boettger, “An extensive study of the influence of dopants on the ferroelectric properties of HfO2,” *J. Mater. Chem. C*, vol. 5, no. 2, pp. 333–338, 2017, doi: 10.1039/c6tc04807b.

[13] S. Starschich, D. Griesche, T. Schneller, and U. Böttger, “Chemical Solution Deposition of Ferroelectric Hafnium Oxide for Future Lead Free Ferroelectric Devices,” *ECS J. Solid State Sci. Technol.*, vol. 4, no. 12, pp. P419–P423, Sep. 2015, doi: 10.1149/2.0061512jss.

[14] H. Liu *et al.*, “Structural and ferroelectric properties of Pr doped HfO2 thin films fabricated by chemical solution method,” *J. Mater. Sci. Mater. Electron.*, vol. 0, no. 0, p. 0, 2019, doi: 10.1007/s10854-019-00874-4.

[15] X. Wang *et al.*, “Ferroelectric yttrium doped hafnium oxide films from all-inorganic aqueous precursor solution,” *Ceram. Int.*, vol. 44, no. 12, pp. 13867–13872, 2018, doi: 10.1016/j.ceramint.2018.04.233.

[16] A. Wei, C. Chen, L. Tang, K. Zhou, and D. Zhang, “Chemical solution deposition of ferroelectric Sr:HfO2 film from inorganic salt precursors,” *J. Alloys Compd.*, vol. 731, pp. 546–553, Jan. 2018, doi: 10.1016/j.jallcom.2017.09.264.

[17] Shingo Yoneda et al, High dielectric permittivity of HfO2-based films with (La,Bi,Nb) substitution, Jpn. J. Appl. Phys. 57 11UF03 2018, doi : https://doi.org/10.7567/JJAP.57.11UF03

[18] C. Abe *et al.*, “Crystal structure and dielectric/ferroelectric properties of CSD-derived HfO2-ZrO2 solid solution films,” *Ceram. Int.*, vol. 43, no. May, pp. S501–S505, 2017, doi: 10.1016/j.ceramint.2017.05.253.

[19] S. Nakayama, H. Funakubo, and H. Uchida, “Crystallization behavior and ferroelectric property of HfO2-ZrO2 films fabricated by chemical solution deposition,” *Jpn. J. Appl. Phys.*, vol. 57, no. 11, pp. 2–7, 2018, doi: 10.7567/JJAP.57.11UF06.

[20] “Comparison of XPS and AES with Other Analytical Techniques,” *An Introduction to Surface Analysis by XPS and AES*. pp. 165–182, 25-Mar-2003, doi: https://doi.org/10.1002/0470867930.ch6.

[21] B. J. Inkson, *Scanning Electron Microscopy (SEM) and Transmission Electron Microscopy (TEM) for Materials Characterization*. Elsevier Ltd, 2016.

[22] I. Szlufarska, M. Chandross, and R. W. Carpick, “Recent advances in single-asperity nanotribology,” *J. Phys. D. Appl. Phys.*, vol. 41, no. 12, 2008, doi: 10.1088/0022-3727/41/12/123001.

Chapter 3

Impact of annealing environment on electrical properties of yttrium-doped hafnium zirconium dioxide thin films prepared by the solution process.

3. Impact of annealing environment on electrical properties of yttrium-doped hafnium zirconium dioxide thin films prepared by the solution process.

3.1. Motivation

As discussed in chapter 2, ALD [1], sputtering [2] and pulsed laser deposition [3] are mostly commonly employed to form thin films of ferroelectric HZO. On contrary, CSD provides an advantage to fabricate cost-efficient devices for different type of applications due to low resource cost. In addition, CSD provides stoichiometric flexibility to investigate wide range of dopants with different composition for thin films with ease [4]. Until now, only some people have reported HfO_2 based ferroelectric thin films prepared by CSD, [4]–[10] however, just a few study on HZO based ferroelectric films prepared by CSD. As discussed in section 2.2.3 of chapter 2, mostly the source or precursor solution prepared using a glove box with inert gas environment, as a result the process becomes sophisticated. However, there are a few reports, where source or precursor solution was prepared in air. Electric properties such as polarization – electric field, shows rounded loops were observed as a result of high leakage current for films deposited using precursor prepared in air [6]. Therefore, ferroelectric properties of HZO films depends on deposition condition of film, especially the annealing environment.

There are few reports on effect of annealing environment on ferroelectric properties of HfO_2 [11]–[14]. Suzuki et al., investigated impact of deposition conditions and annealing environment on ferroelectric properties of Y doped HfO_2 deposited by using sputtering [11]. For HZO films deposited by metal-organic chemical vapor deposition (MOCVD), Shimizu et al., reported the effect of annealing gas on ferroelectric properties [12]. Moreover, effect of annealing forming gas environment on ferroelectric properties of ALD HZO was also investigate by park et al [13]. Yano et al., reported effect of oxygen and nitrogen annealing environment on HZO thin films deposited by CSD [14]. Therefore, it is interesting to investigate the impact of annealing environment on the ferroelectric properties of HZO films deposited by CSD.

Previously, we reported Y doped HZO (Y-HZO) films prepared by CSD [15]. It was observed that Y-HZO shows better ferroelectric properties in comparison to undoped HZO for MFS structure which will be discussed in chapter 5. But, when samples were annealed in an oxygen

environment, It was found that P-E loops were rounded and impact of annealing atmosphere or environment has not been investigated. In this chapter, we will systematically investigated and discuss ferroelectric properties of Y-HZO films annealed in a vacuum, nitrogen and oxygen from 600-800 ^{o}C deposited by CSD for Metal-Ferroelectric-Metal (MFM) structure. It was found that Vacuum annealed Y-HZO films exhibits clear P-E loops due to lower leakage current as compared to nitrogen and oxygen annealed samples.

3.2. Experimental procedure

At first, the source solution of Y-HZO was prepared as described in chapter 2. The source solution was deposited on a Pt/Ti/SiO_2/Si substrate by spin coating, followed by drying of wet films at 225 °C for 3 min in air on a hot plate. Y-HZO films were crystallization using rapid thermal annealing (RTA) system at 600-800 °C for 3 min in a vacuum environment at 2.3 Pa. Likewise Y-HZO films were also crystallized at 600, 700 and 800 °C for 3 min in N_2 and O_2 environments. Thickness of Y-HZO films was measured using Alpha step profiler and was approximately 40 nm. In order to fabricate MFM structure, 100 nm thick Platinum metal (top electrode) dot of 300 μm diameter was sputtered through a metal mask. Interface between top electrode Pt and Y-HZO was improved by Post-metallization annealing (PMA) using RTA system at 500 °C for 5 min in an O_2 environment.

3.3. Crystallinity of films

As discussed in chapter 1, orthorhombic phase (O-phase) is important for ferroelectricity in HZO. Therefore, crystallinity of Y-HZO films was measured using XRD. Figure 3.1 (a) shows diffraction patterns of 5 % Y-HZO annealed in a vacuum environment at different annealing temperature. The diffraction peak around 30.5 and 35.2 ° were observed, suggesting that Y-HZO films can be crystallized even at 600 ^{o}C which is also observed previously [15]. Starschich et al. reported CSD HfO_2 films requires temperature more than 495 ^{o}C to achieve complete pyrolysis and no further weight loss was observed [5], which indicates that temperature over 495 ^{o}C is needed to crystalized films fabricated by CSD. Vacuum annealed Y-HZO samples shows a large diffraction peak at 30.5° corresponding to 111 of O-Phase or tetragonal phase (T-phase) or cubic phase (C-phase). It is interesting to emphasis that shift of diffraction peak was observed with increasing crystallization temperature from 600 to 800 ^{o}C

which is also observed in other ferroelectric HfO_2 films [16]. Therefore, shift in the diffraction peak shift suggests the formation of ferroelectric O-phase for films annealed at 800 °C. The sub-peak around 35.2 ° corresponds to 200 direction of O-phase or C-phase or T-phase. Figure 3.1(b) and (c) demonstrates XRD patterns of 5 % Y-HZO annealed in a N_2 and O_2 environment at various crystallization temperatures, respectively. The most intense peak about 30.5 and 35.2 ° were observed, demonstrating that Y-HZO films annealed in nitrogen and oxygen, can be crystallized at 600 °C too. The shift of diffraction peak was observed with increase in annealing temperature from 600 to 800 °C in case of Y-HZO films annealed in N_2 and O_2 samples too. Figure 3.1(d) shows XRD patterns of 5 % Y-HZO annealed at 800 °C in various annealing environment., It is clear that films annealed at 800 °C in various annealing environment vacuum, O_2 and N_2 environment also depicts diffraction peak around 30.5 and 35.2 ° which corresponds to 111 and 200 of O-phase/T-phase/C-phase, respectively. However, the diffraction peak intensity of Y-HZO films in O_2 is relatively low compared to vacuum and N_2.

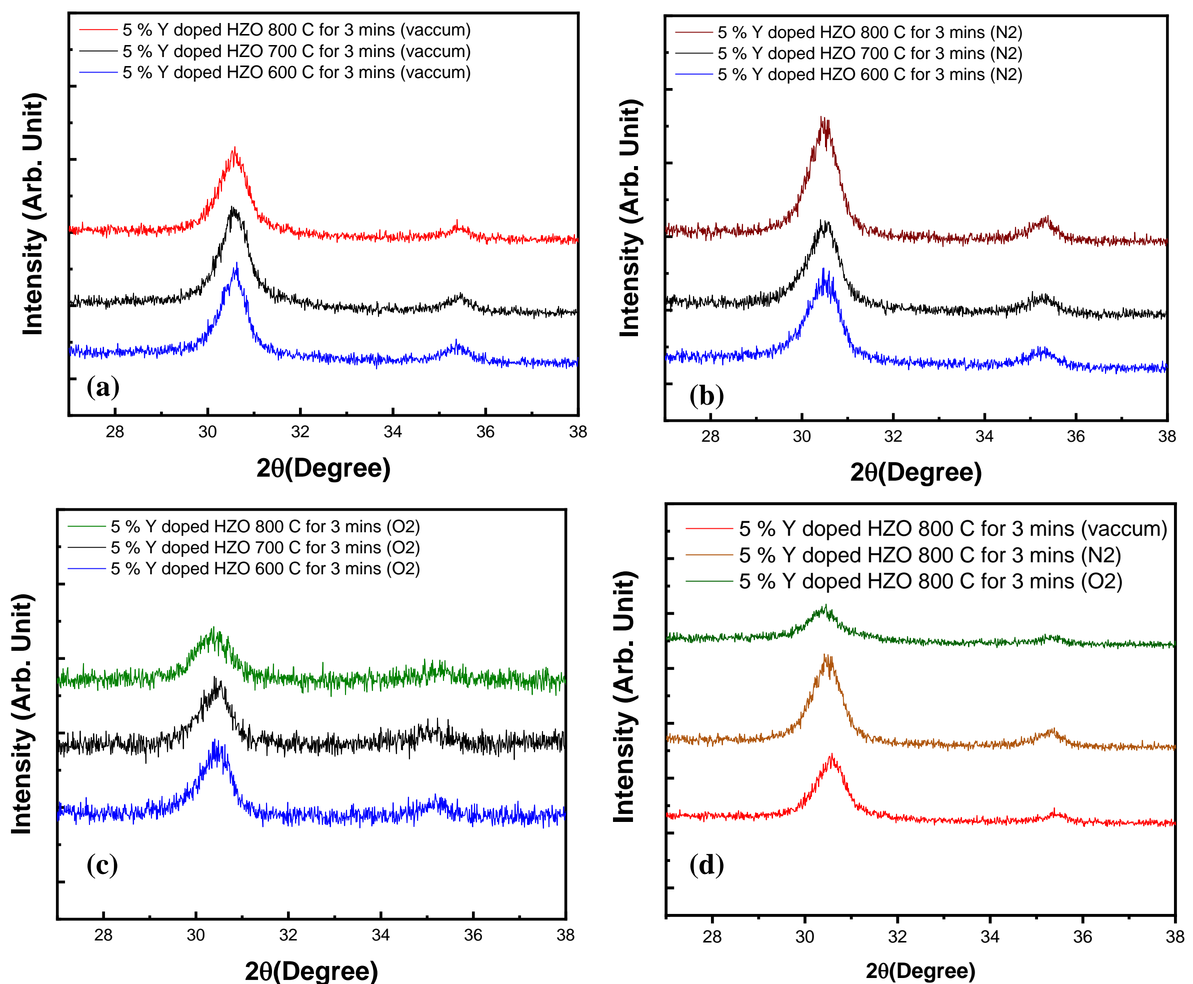

Fig. 3.1. XRD patterns of (a) Y-HZO annealed in a vacuum environment at various crystallization temperature (b) Y-HZO annealed in a N_2 environment at various crystallization temperature (c) Y-HZO annealed in a O_2 environment at various crystallization temperature (d)

The grain sizes of vacuum annealed Y-HZO films at 600, 700, and 800 °C were estimated 9.7, 9.4, and 8.7 nm, respectively as shown in Figure 3.2. Park et al reported a decrease in grain size shows better ferroelectric properties [40]. The grain size of oxygen annealed Y-HZO at 800 °C was 8.1 nm which is slightly lower as compared to vacuum annealed 8.7 nm as shown in Figure 3.2. The estimated grain size of N_2 annealed Y-HZO films at 800 °C was 9.4 nm as shown in Figure 3.2.

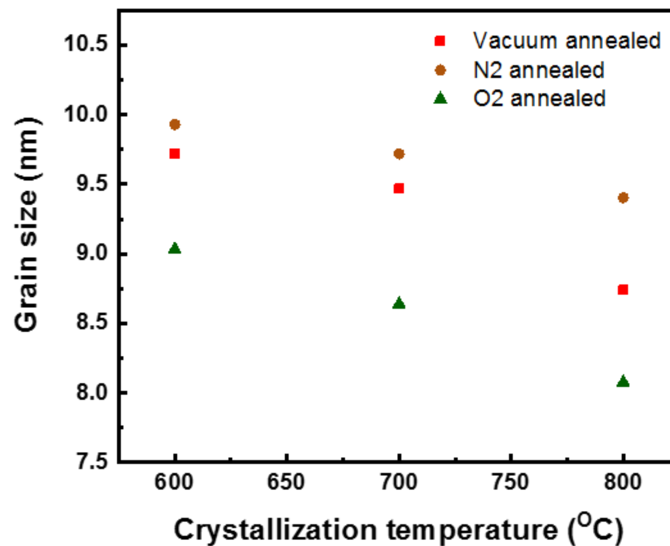

Fig. 3.2. Effect of annealing temperature on the grain size of Y-HZO annealed in various annealing environment.

3.4. XPS analysis

In addition to XRD, Chemical bond state of CSD Y-HZO annealed in various annealing environment was investigated using XPS. Figure 3.3 (a) illustrates O 1s spectra of vacuum annealed Y-HZO films at different crystallization temperatures. Metal-oxide (M-O) bond peak was observed at 530 eV due to presence of oxygen ions in O-Hf, O-Zr and O-Y, whereas peak of higher energy around 532 eV as result of oxygen vacancies (V_O) in the Y-HZO films [17]. These results demonstrate good consistency with HZO films reported previously [18]. Figure

3.3 (a) manifests that 800 ^{o}C annealed Y-HZO film possess more oxygen vacancies in comparison to 600 and 700 ^{o}C annealed films. O 1s Peaks of Y-HZO films were deconvoluted to calculated peak area ratios of Vo to M-O peak. these are 25, 27 and 35% for 600, 700, and 800 ^{o}C annealed Y-HZO films. These values suggest that amount of V_O increases with increasing the annealing temperature. The crystalline phases within the HZO thin films were suggested to be closely related to the amounts of V_O contained in the HZO films [18]. According theoretical aspect, the presence of the oxygen vacancies is preferable to stabilize the O-phase of HfO_2-based ferroelectrics [19]. In addition, Min et al., reported that HZO films changes phase from ferroelectric to paraelectric with decreasing oxygen vacancies [18]. Therefore, It is believed that the existence of oxygen vacancies in vacuum annealed Y-HZO film at 800 ^{o}C is beneficial to stabilize the O-phase in order to obtain good ferroelectric properties. As previously reported, residual carbon may also play an vital role in stabilization of the ferroelectricity in Y-HZO films and will be discussed in detail in chapter 4 [15]. Hence, XPS spectra of C 1s was also evaluated for Y-HZO films. Figure 3.3 (b) depicts C 1s spectra of vacuum annealed at different annealing temperature. The XPS peaks observed around 285 and 288 eV related to adventitious carbon-carbon bond and carbon-oxygen bond, respectively [20]. As annealing temperature of vacuum Y-HZO films increases carbon-oxygen (C-O) bond peak intensity shows substantial decrease.

Chemical bonding state was also carried for Y-HZO annealed in different annealing environments at 800 ^{o}C using XPS as shown in Figure 3.3 (c) and 3.3 (d). Figure 3.3 (c) clearly shows that vacuum annealed Y-HZO films shows existence of more oxygen vacancies, $V_{O,}$ as compared to N_2 and O_2 annealed Y-HZO films. The calculated peak area ratio of M-O to V_O of N_2 and O_2 annealed Y-HZO films were approximately calculated by peak deconvolution; these are 23 % and 20 %. In comparison, Oxygen vacancies concentration observed in Y-HZO film annealed in vacuum much higher compared to N_2 and O_2 films. Figure 3.3 (d) illustrates C 1s XPS spectra of Y-HZO films annealed in various annealing environment at 800 ^{o}C. Low intensity of C-O bond peak around 288 eV was observed for vacuum annealed Y-HZO films as compared to N_2 and O_2 annealed Y-HZO films at 800 ^{o}C. These result reveals that the evaporation of organic species is enhanced during the annealing process in case of vacuum annealing.

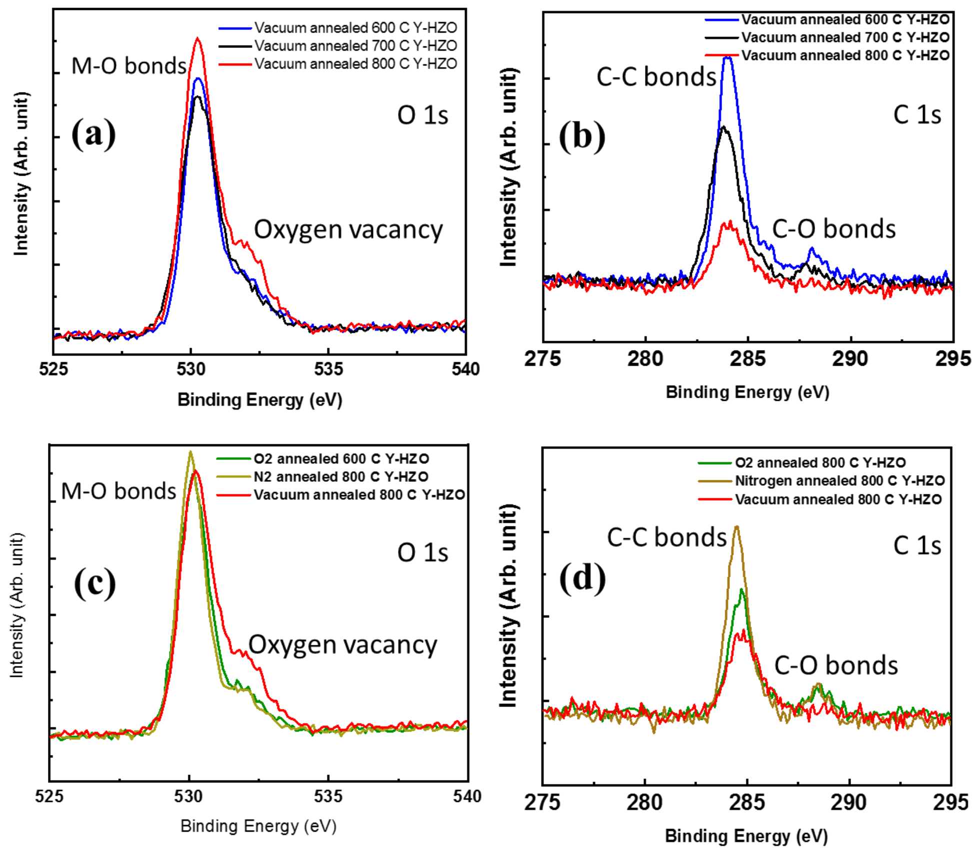

Fig. 3.3. XPS spectra of vacuum Y-HZO at various annealing temperature (a) O 1s (b) C 1s; XPS spectra of Y-HZO films annealed in various annealing environment (c) O 1s (d) C 1s

3.5. SIMS

Carbon concentration in Y-HZO films was measured by using SIMS as illustrated in Figure 3.4. The carbon content was found about 5 % for all Y-HZO samples and no substantial variation was observed for the vacuum, N_2 and O_2 annealed Y-HZO films. Even though total amount carbon concentration is similar for all Y-HZO samples, it is worth noting that the XPS results shows the C-O bonds are reduced for vacuum annealed samples.

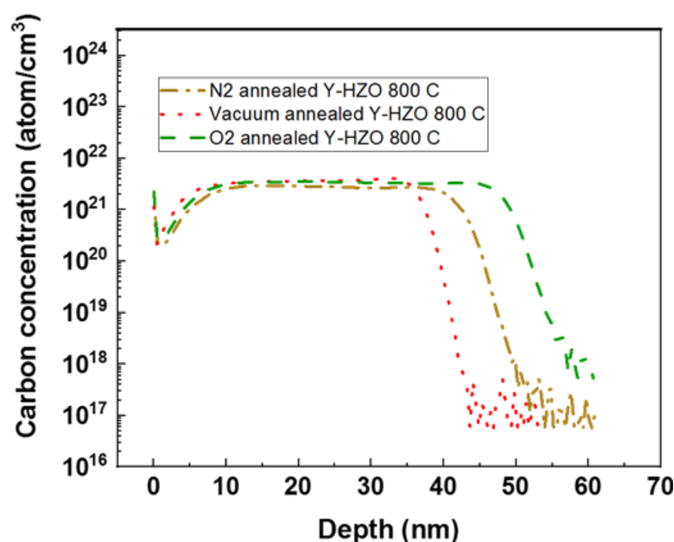

Fig. 3.4. SIMS profile of Y-HZO films annealed in various annealing environment.

3.6. TDS

TDS was also measured to understand the desorption of various gas species during the annealing process for the Y-HZO film. The measured sample is the Y-HZO sol-film which was spin-coated and dried at 225 °C on a hot plate for 3 mins. The sample was heated in a high vacuum with temperature ranging up to 1100 °C. Figure 3.5 shows desorption signal of hydrogen, water, CO or C_2H_4 and CO_2 or C_2H_8 which corresponds to mass numbers of 2, 18, 28, 44, respectively. Initially, large peak depicting H_2O desorption around 100 °C is not from the film but considered as a result of the water absorbed from the sample stage surface. Peak observed around 280~290 and 400 °C, desorption of water and CO_2 or C_3H_8 species are observed which corresponds to the desorption of organic species and oxidation reaction, respectively. Moreover, methyl and ethyl species (mass 15, 29) desorption peaks were observed around 275 °C (not shown in the Figure 3.5). In addition, CO or C_2H_4 species desorption peaks were observed around 280, 450, and 600 °C too. As discussed in previous section, CSD HfO_2 based films needed annealing temperature of more than 495 °C for complete pyrolysis. The HfO_2 precursor solution, DTA/TG (differential thermal analysis/ thermo gravimetry) characteristics measured previously which reveals that the oxidation reaction begins to take place around 350 °C [21]. Hence, it is believed that the various species desorption peaks around 280-290 °C are mainly due to the removal of the organic species in the spin-coated wet film and that relatively sharp desorption peaks observed around 400°C are caused by the oxidation process. It is interesting to emphasis that substantial desorption of CO or C_2H_4 was observed for temperature ranging from 500 to 800°C, and that the desorption of hydrogen, water, and

CO_2 or C_3H_8 was observed around 800 °C or above. These results are consistent with the XPS data which shows C-O bonds decreases for the film annealed at 800 °C.

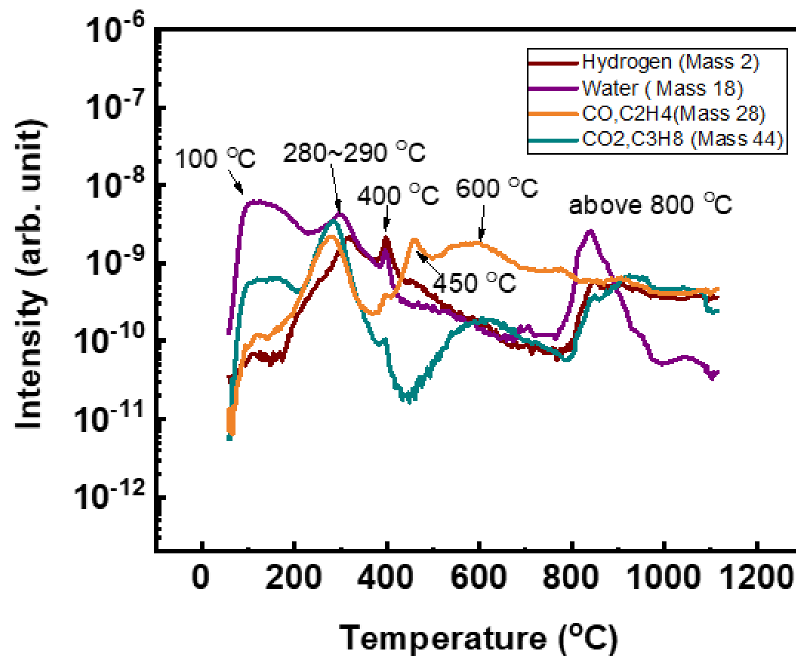

Fig. 3.5. TDS signals of Y-HZO film as a function of temperature

3.7. Surface morphology of films

AFM was used to characterize the surface morphology of platinized substrate, vacuum and N_2 annealed Y-HZO thin films as demonstrated in Figure 3.6. RMS roughness of platinized was 0.5 nm. Vacuum annealed Y-HZO films at various crystallization temperature of 600, 700 and 800 °C shows root means square roughness (R_{rms}) value of 0.79, 0.85, and 0.87 nm, respectively. These values suggest that R_{rms} roughness value increases when annealing temperature increased and these results are lower than that of previously reported HfO_2 based ferroelectric films deposited by CSD. Surface roughness of films varies on several factors such as process for crystallization [9]. Therefore, the effect of annealing environment on the surface roughness was examined. The RMS roughness of Y-HZO film annealed at 800°C in N_2 and O_2 was 1.34 and 1.13 nm respectively [15], which are more than that of vacuum annealed Y-HZO film. Such an effect by vacuum annealing has been reported for Dy_2O_3 films [22], [23]. Vacuum annealed Y-HZO films have a relatively smooth surface compared to O_2 and N_2 annealed Y-HZO films.

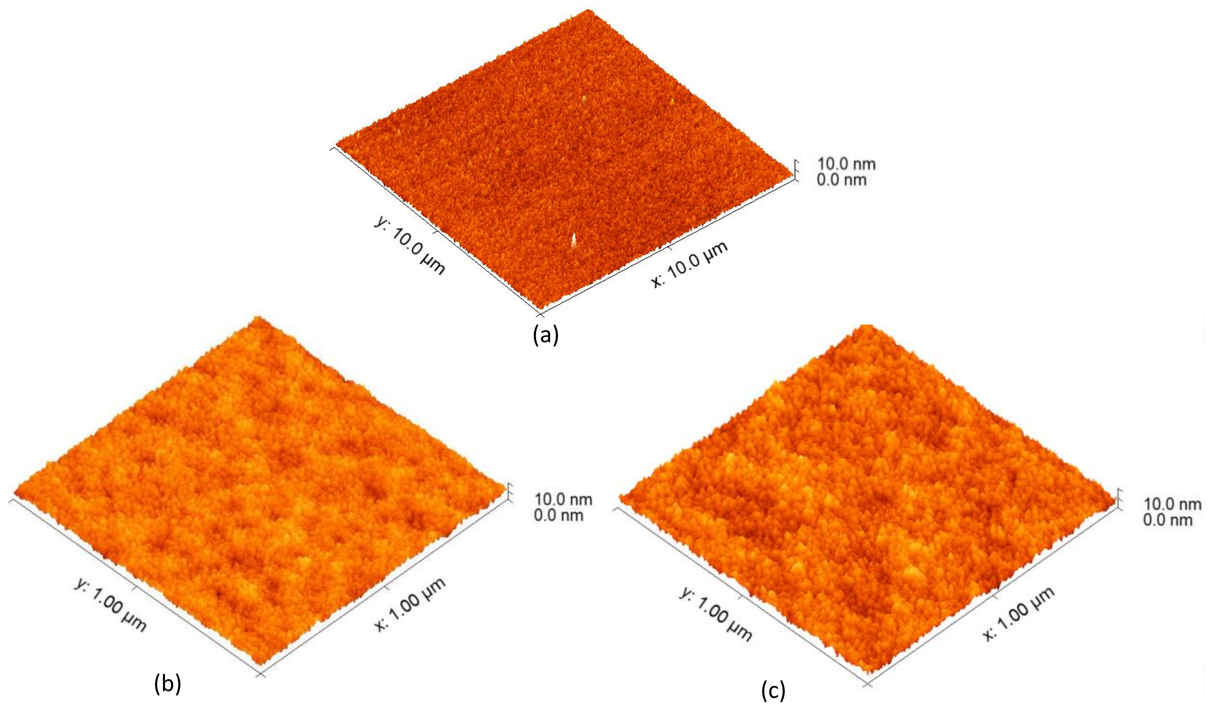

Fig. 3.6. AFM of (a) Pt substrate and Y-HZO films annealed at 800 ^{o}C in (b) vacuum and (c) N_2 environment

The grain size of HZO films can largely effects the ferroelectric properties [24]. The SEM was used to analyze the surface of Y-HZO films annealed in a vacuum and N_2 environment. Figure 3.7 illustrates SEM image (plan-view) of the Y-HZO films annealed in vacuum and N_2 environment at 800 ^{o}C with visible small grains. The grain size of Y-HZO was estimated by using Gwyddion software [25] and these values are 8.84 and 9.53 nm for the films annealed in vacuum and nitrogen, respectively. The grain size of Y-HZO films annealed in vacuum and N_2, calculated from out of plan XRD peaks shows similar tendency as grain size of estimated from SEM (in-plane). It is worth noting that Y-HZO films annealed at 800 ^{o}C in vacuum environment still shows a smaller grain size, which is believed to be desirable to achieve O-phase and ferroelectric properties [49]. As discussed in the XPS section, more oxygen vacancies present in the Y-HZO film annealed in vacuum at 800 ^{o}C, as compared to the films at lower temperature in vacuum and annealed in N_2 at 800 ^{o}C. It was suggested that oxygen vacancies would be helpful for stabilization of ferroelectric phase [19]. On the other hand, a correlation between grain size and O-phase fraction in the HZO was discussed earlier, revealing that smaller grain size would have larger fraction of O-phase [26]. Therefore, as shown later in this chapter, good ferroelectric properties are expected for the Y-HZO film annealed in vacuum at 800 ^{o}C, which has oxygen vacancies and small grain size.

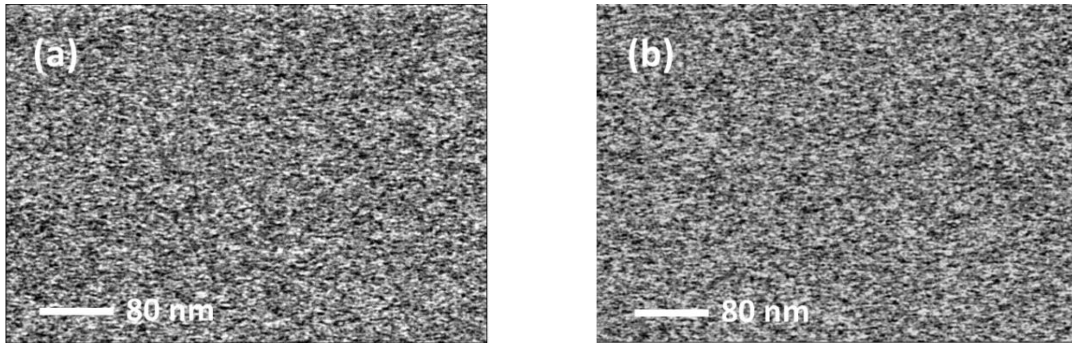

Fig. 3.7 SEM images of Y-HZO annealed at 800 ^{o}C in (a) vacuum environment (b) N_2 environment.

3.8. Effect of annealing temperature on vacuum annealed Y-HZO films.

In order to confirm ferroelectricity, the P-E and C-V characteristics were carried out for vacuum annealed Y-HZO films fabricated by CSD. Figures 3.8 (a), (c) and (e) depicts P-E loops, and Figures 3.8 (b), (d), and (f) illustrates equivalent current response of vacuum annealed Y-HZO films at different annealing temperatures, 600, 700, and 800 ^{o}C respectively. P-E loops shows rounded hysteresis loops due too high leakage current when Y-HZO films annealed at 600 ^{o}C. Figure 3.8 (b) represents equivalent current response, revealing no clear switching current response. We can see the trace of switching current along with leakage current for the film annealed at 700 ^{o}C. On the other, Figure 3.8 (e) shows P-E loops of 800 ^{o}C with good ferroelectric hysteresis loop due to lower leakage current compared to 600 and 700 ^{o}C. Figure 3.8 (f) shows corresponding current response where clear switching current was observed. Leakage density-electric field (J-E) characteristics were measured for Y-HZO films annealed at various annealing temperature as shown in figure 3.9. Leakage current at 1 MV/cm for vacuum annealed Y-HZO films at 600, 700, and 800°C roughly estimated from Figure 3.9 are 3.6 x 10^{-3}, 1.8 x $10^{-3,}$ and 6.5 x 10^{-5} A/cm^2, respectively, which clearly shows a drastic decrease in leakage current when annealing temperature increases. Remnant polarization (P_r) and coercive field (E_c) of Y-HZO films annealed at 600-800 ^{o}C were estimated from Figure 3.8 (a), (c) and (e), and these are approximately 10 μC/cm^2 and 1.8 MV/cm, 14 μC/cm^2 and 1.6 MV/cm, 15 μC/cm^2 and 1.4 MV/cm respectively. P_r value shows an increasing trend with increasing annealing temperature which is consistent with previously reported other ferroelectric HfO_2 [15], [27].

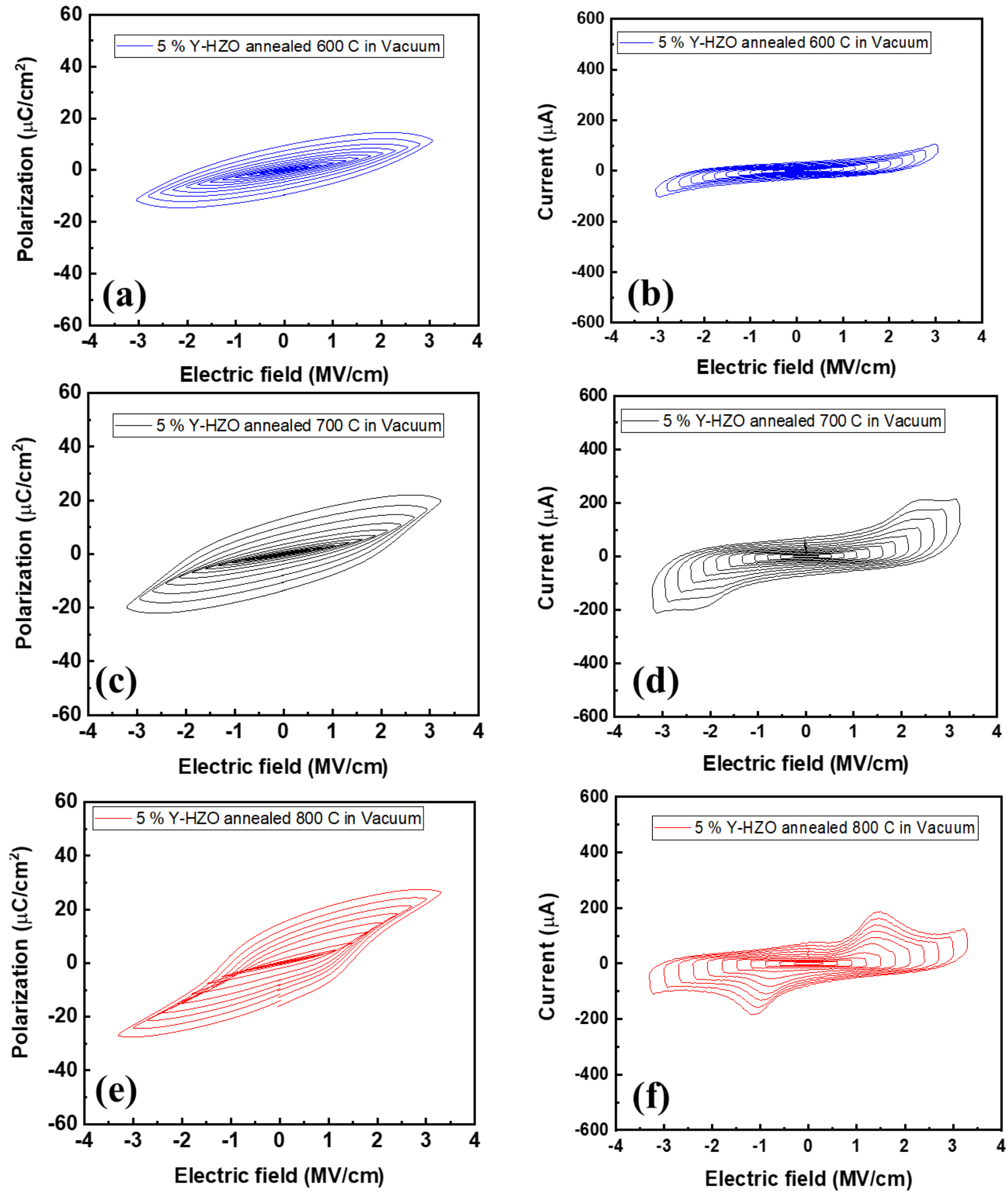

Fig. 3.8. Electrical properties of Y-HZO annealed in a vacuum; (a) P–E loops of Y-HZO annealed at 600 °C (sweeping voltage −12 to 12 V), (b) I_s-E curves of Y-HZO annealed at 600 °C, (c) P–E of Y-HZO annealed at 700 °C (d) I_s-E of Y-HZO annealed at 700 °C, (e) P–E of Y-HZO annealed at 800 °C, and (f) I_s-E of Y-HZO annealed at 800 °C.

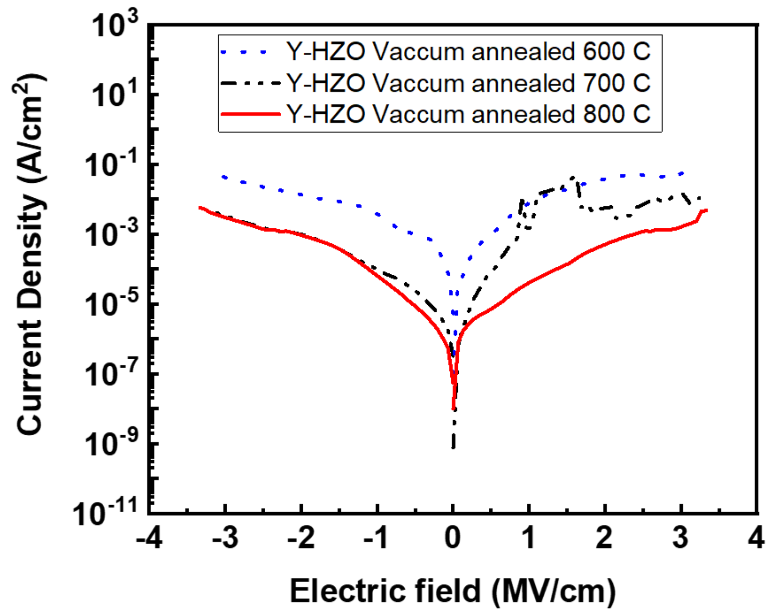

Fig. 3.9. Leakage current density (J-E) of Y-HZO films annealed in vacuum at various annealing temperature.

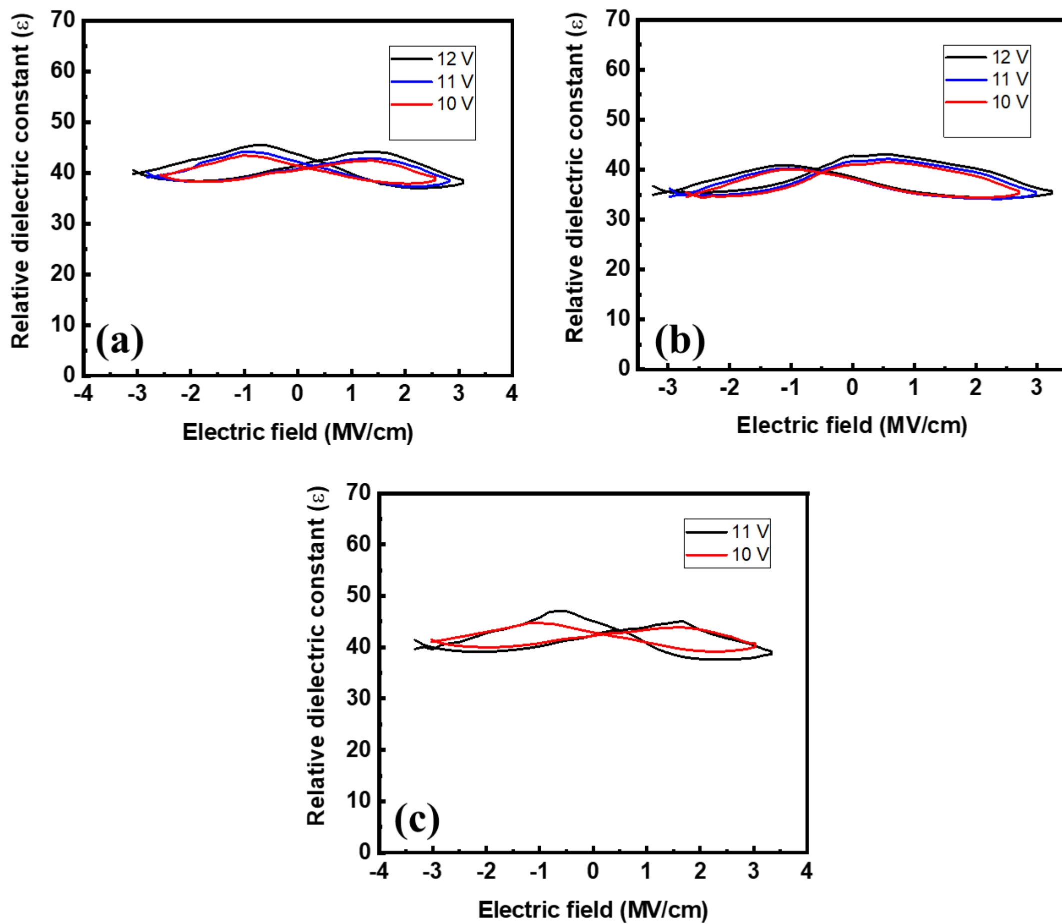

Fig. 3.10. Capacitance-Voltage (C-V) curves of Y-HZO annealed in a vacuum at (a)600 °C (b) 700 °C (c) 800 °C

To further confirm ferroelectricity, the capacitance-Voltage (C-V) curves were measured for Y-HZO films annealed in vacuum at various annealing temperature. Figure 3.8 (a), (b), and (c) depicts C-V curves of vacuum annealed Y-HZO films at 600, 700, and 800 ^{o}C, respectively, exhibiting clear butterfly shape as a result of the ferroelectric nature of Y-HZO films. Coercive field, E_c was estimated from the peaks and these are 1.07 MV/cm, 1.1 MV/cm and 1.18 MV/cm for Y-HZO films annealed 600, 700, and 800 ^{o}C, respectively. The E_c values observed shows good consistency with other HfO_2 based ferroelectric materials [28]. Although 600 ^{o}C annealed Y-HZO film demonstrates rounded P-E loops and the switching current response is barely observed, but C-V curves shows clear inverse butterfly shaped. It is clear from C-V curves that Y-HZO films annealed in vacuum at 600 ^{o}C shows similar tendency in butterfly shape in comparison to 800 ^{o}C annealed sample. Additionally, change in capacitance between maximum and minimum peak values is gradually increased with annealing temperature, which suggested the ferroelectricity was enhanced by higher the annealing temperature. Hence, the inverse butterfly curves obtained in C-V curves for the 600 ^{o}C annealed sample is probably due to the ferroelectricity even though inferior in comparison to the 800 ^{o}C annealed Y-HZO film. The cause for the discrepancy between C-V and P-E measurements is not fully known but presumably due to measurement method difference, where the P-E loops are acquired by evaluating charge along with slowly sweeping the applied voltage and C-V curves are acquired by the capacitance measured by small AC signal at a fixed DC bias. Lui et al, also reported a butterfly shaped C-V curve for P_r doped HfO_2 film whose ferroelectricity is not clear from the observed rounded P-E loops [6].

3.9. Effect of annealing temperature on N_2 annealed Y-HZO films.

Next, P-E and C-V characteristics were measured for N_2 annealed CSD Y-HZO films to confirm ferroelectricity in the films. Figure 3.10 (a), (c) and (e) depicts P-E loops, and whereas Figures 3.10 (b), (d), and (f) illustrates equivalent current response of nitrogen annealed Y-HZO films at different annealing temperatures, 600, 700, and 800 ^{o}C respectively. It was found that P-E loops of all nitrogen annealed samples exhibits rounded loops due to the leakage current and the switching current response of nitrogen annealed Y-HZO films cannot be clearly observed.

To further confirm ferroelectricity for nitrogen annealed Y-HZO films, C-V curves were measured. Figures 3.11 (a), (b) and (c) show C-V curves of nitrogen annealed Y-HZO films annealed at 600-800 ^{o}C, respectively, exhibiting clear butterfly shape as a result of the ferroelectric nature of Y-HZO films. Coercive field, Ec was estimated from the C-V curves peaks and these are 1.29 MV/cm, 1.26 MV/cm and 1.1 MV/cm for Y-HZO films annealed 600, 700, and 800 ^{o}C, respectively. The Ec values observed for Y-HZO films have good consistency with other HfO_2 based ferroelectric materials [29].

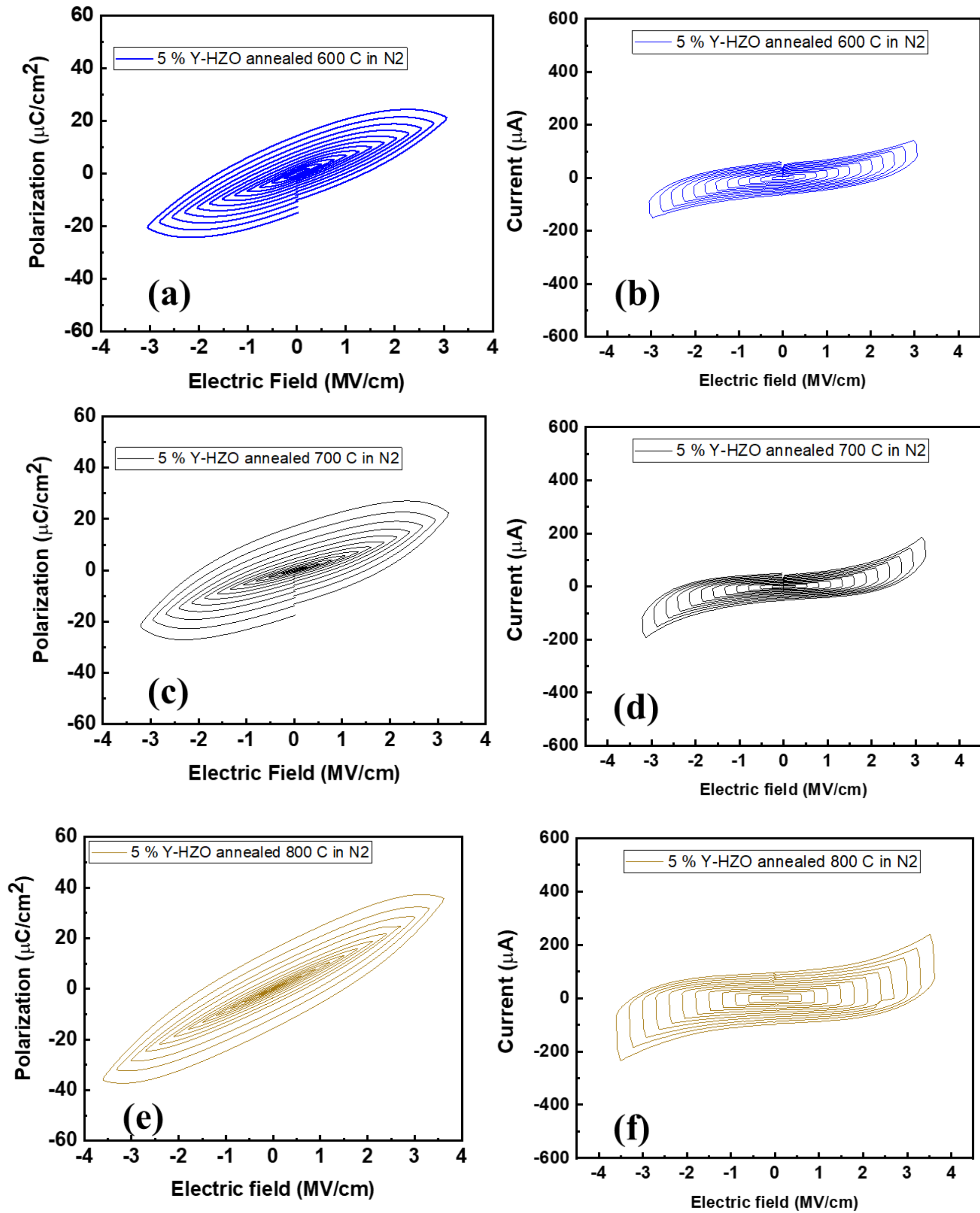

Fig. 3.11. Electrical properties of Y-HZO annealed in a N_2; (a) P–E loops of Y-HZO annealed at 600 °C (sweeping voltage −12 to 12 V), (b) I_s-E curves of Y-HZO annealed at 600 °C, (c) P–E of Y-HZO annealed at 700 °C (d) I_s-E of Y-HZO annealed at 700 °C, (e) P–E of Y-HZO annealed at 800 °C, and (f) I_s-E of Y-HZO annealed at 800 °C.

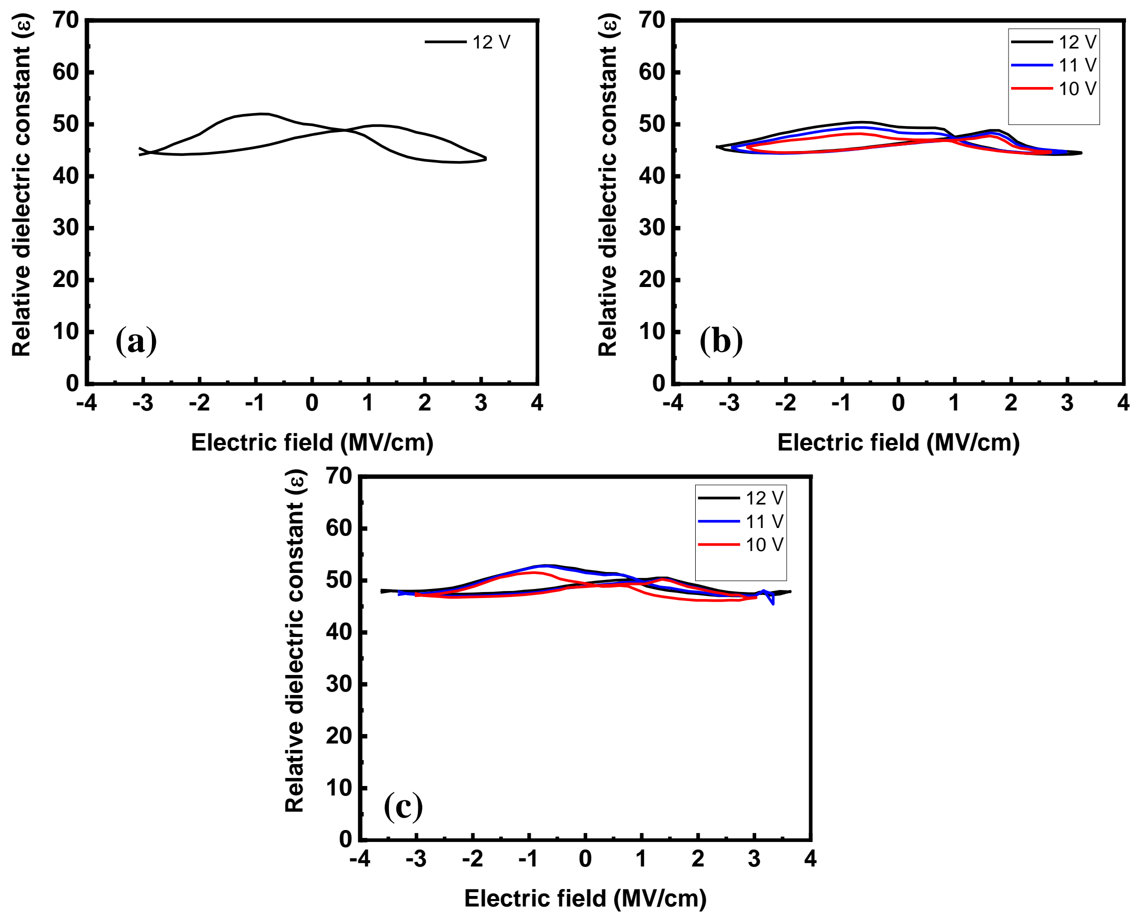

Fig. 3.12. Capacitance-Voltage (C-V) curves of Y-HZO annealed in a N_2 at (a) 600 °C (b) 700 °C (c) 800 °C

3.10. Effect of annealing temperature on O_2 annealed Y-HZO films.

Likewise, P-E and C-V characteristics were measured for O_2 annealed CSD Y-HZO films to confirm ferroelctrcity. Figures 3.13 (a), (c) and (e) shows P-E loops, and Figures 3.13 (b), (d), and (f) show corresponding current response of Y-HZO films annealed in a O_2 environment at different crystallization temperatures, 600, 700 and 800 ^{o}C respectively. Y-HZO films annealed at 600 ^{o}C shows rounded P-E loops since they are affected by leakage. Y-HZO films annealed at 700 and 800 ^{o}C show ferroelectric *P–E* loops with a trace of switching current along with leakage current.

To further evaluate ferroelectricity in O_2 annealed CSD Y-HZO films C-V measurement were carried out. Figures 3.14 (a), (b) and (c) depicts C-V curves of Y-HZO films annealed in O_2 at 600, 700, and 800 ^{o}C, respectively, exhibiting clear butterfly shape as a result of the ferroelectric nature of oxygen annealed Y-HZO films. Coercive field, E_c was calculated from the C-V curves peaks and these are 1.16 MV/cm, 1.23 MV/cm and 1.08 MV/cm for Y-HZO films annealed 600, 700, and 800 ^{o}C, respectively. The Ec values observed for Y-HZO films have good consistency with other HfO_2 based ferroelectric materials [29].

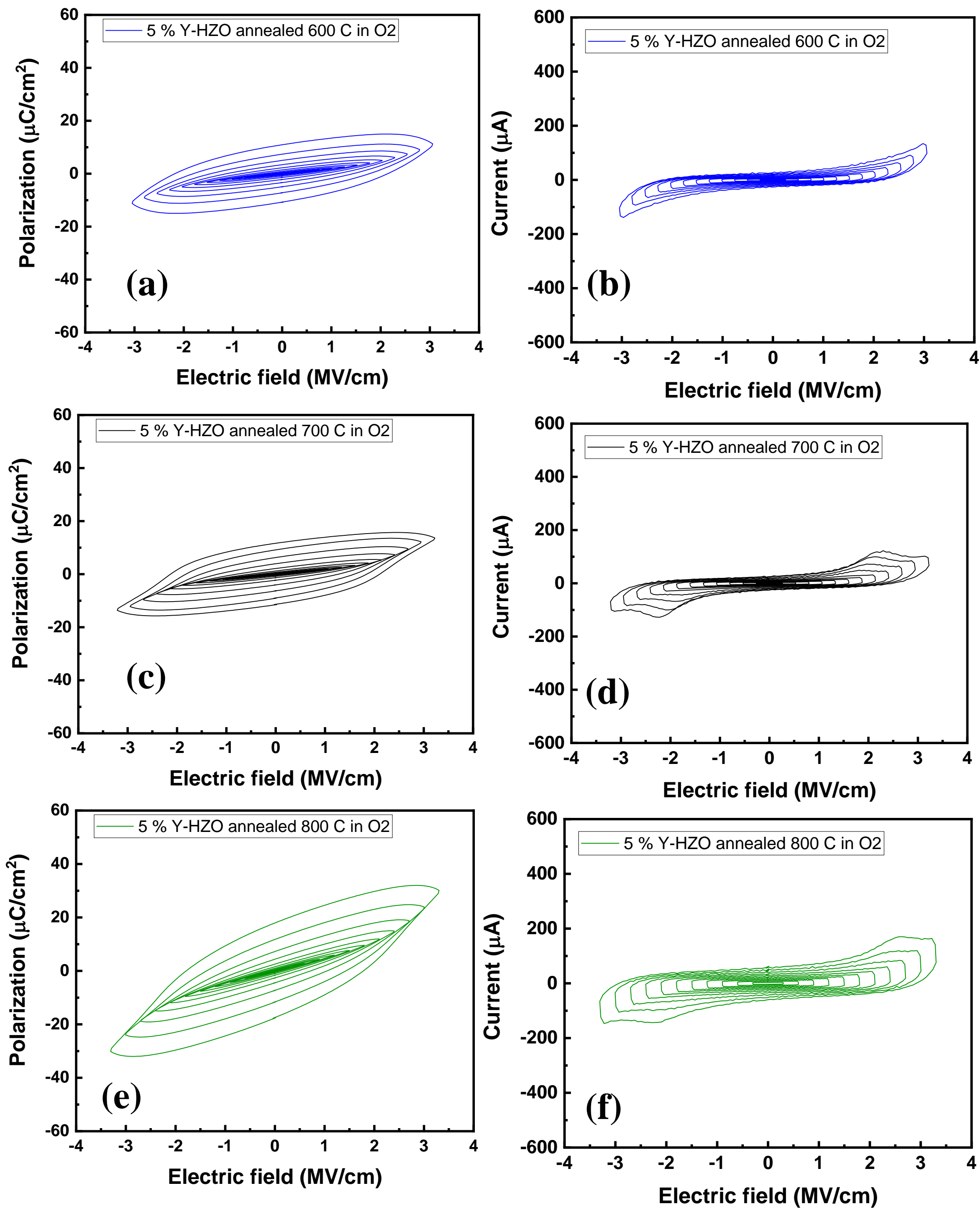

Fig. 3.13. Electrical properties of Y-HZO annealed in O_2 ; (a) P–E loops of Y-HZO annealed at 600 °C (sweeping voltage −12 to 12 V), (b) I_s-E curves of Y-HZO annealed at 600 °C, (c) P–E of Y-HZO annealed at 700 °C (d) I_s-E of Y-HZO annealed at 700 °C, (e) P–E of Y-HZO annealed at 800 °C, and (f) I_s-E of Y-HZO annealed at 800 °C.

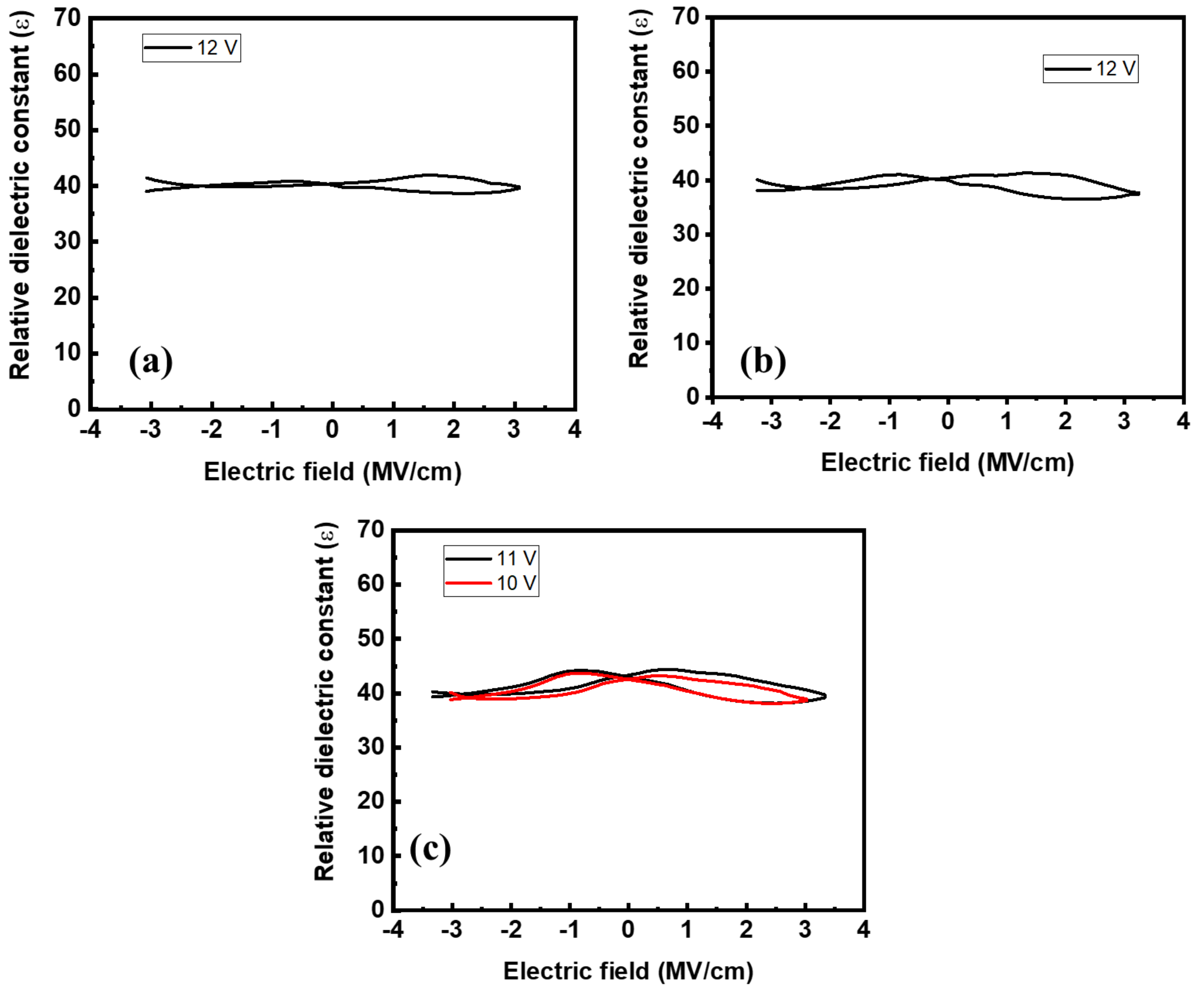

Fig. 3.14. Capacitance-Voltage (C-V) curves of Y-HZO annealed in a O_2 at (a) 600 °C (b) 700 °C (c) 800 °C

3.11. Effect of annealing environment on Y-HZO films

As discussed in the previous section. vacuum annealed Y-HZO films at 800 °C shows good ferroelectric properties which was confirmed by P-E loops and C-V curves. At first, P-E loops were compared to investigate the effect of annealing environment for Y-HZO films annealed at 800 °C as shown in Figures 3.15. It is clear that P-E loops of N_2 annealed film exibits rounded loops due to the leakage current. On the other hand, O_2 annealed Y-HZO films exhibits ferroelectric P-E loops with small trace of switching current along with leakage current. Whereas Vacuum annealed samples shows good ferroelectric properties with clear hysteresis loops due to drastic decrease in leakage current as discussed in previous section.

Figure 3.16 depicts J-E characteristics of Y-HZO films annealed in N_2 and O_2 environment. Leakage current density at 1 MV/cm was estimated for Y-HZO films annealed in environment; there are 3.8 x 10^{-3}, 1.8 x $10^{-3,}$ and 6.5 x 10^{-5} A/cm^2, respectively. Drastic decrease in leakage current was observed for vacuum annealed Y-HZO as compared to N_2 and O_2 environment which is presumably because of lower C-O bonds in vacuum annealed samples. Kim et al., reported the impact of organic species on leakage current of HZO films deposited by different precursor of HZO for ALD [30]. Higher carbon content in HZO films may results in higher leakage current. In addition, surface roughness of vacuum is relatively smooth as compared to N_2 and O_2 annealed sample which is another reason for lower leakage current in vacuum annealed sample. Therefore, it is suggested C-O bonds and surface roughness play important roles in decreasing the leakage current in Y-HZO films prepared by CSD.

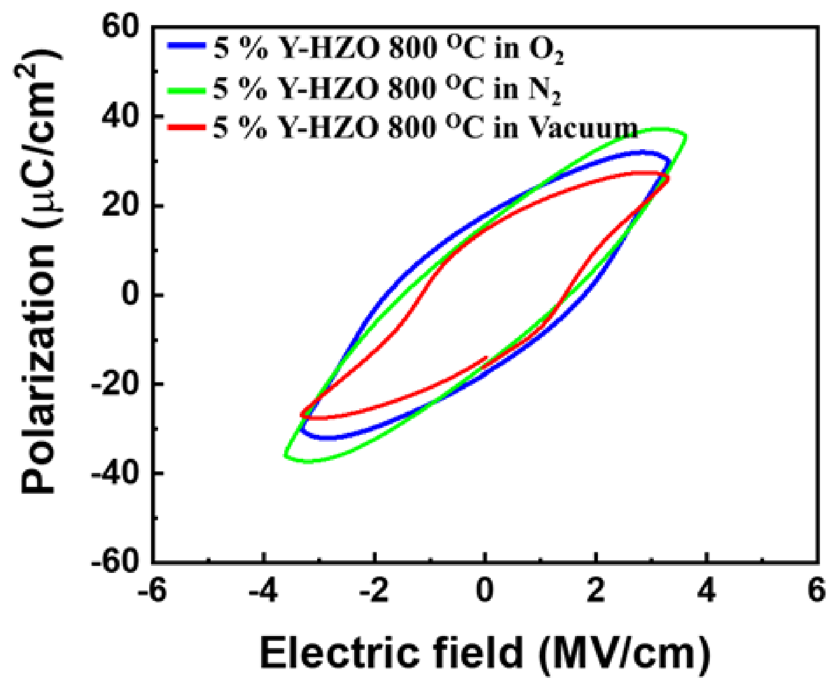

Fig. 3. 15. Electrical properties of Y-HZO films annealed in various annealing environment.

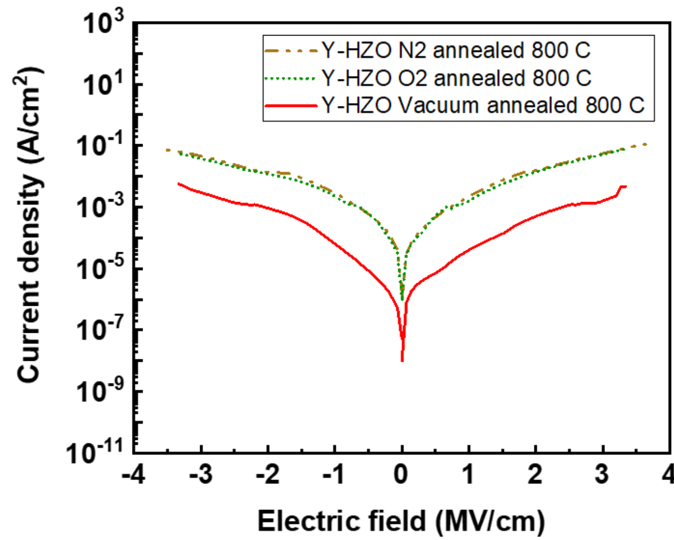

Fig. 3. 16. Leakage current density (J-E) of Y-HZO) annealed in various annealing environment at 800 °C

The ferroelectric nature of Y-HZO films annealed at 800 °C in vacuum, N_2 and O_2 environment was also compared by C-V measurement. Figure 3.10 (c), 12 (c) and 14 (c) show CV curves of Y-HZO films annealed at 800 °C in vacuum, N_2 and O_2 environment, respectively. The capacitance change was estimated for Y-HZO films annealed at 800 °C in vacuum, N_2 and O_2 environment. Observed difference in maximum and minimum capacitance values in C-V curves of the N_2 and O_2 annealed Y-HZO films is smaller than that of the Y-HZO film annealed in vacuum at 800 °C, which indicates the ferroelectricity of the Y-HZO film annealed in N_2 or O_2 is inferior to that of the film annealed in vacuum.

Hence, vacuum annealed Y-HZO shows superior ferroelectric properties as a result of low C-O bonds, higher concentration of V_O, appropriate grain size, and lower leakage current. Therefore, the annealing environment plays an important role in enhancing ferroelectric properties.

3.12. Comparison of ferroelectric properties of HZO

Table 3.1. summarizes ferroelectric properties of HZO for comparison between previous report and current work. Best P-E loops reported so far is for 10 nm thick ALD HZO films which have low crystallization temperature with high P_r of 17 μC/cm^2. P-E loops in this work is not good but comparable in terms of P_r, especially when thickness of HZO films is around 40 nm. In case of CSD HZO films, reported P_r value of 8 μC/cm^2 is much lower than P_r value of Y-HZO films observed in this work. Most of the reports requires PMA to observed

ferroelectricity in HZO films whereas in this work ferroelectricity in Y-HZO can be observed even after PDA.

Table 3.1 Comparison of ferroelectric properties of HZO deposited by various deposition techniques.

Deposition method	Thickness (nm)	Annealing environment / temperature/ Time	Top electrode/ Bottom electrode	P_r ($\mu C/cm^2$)	E_c (MV/cm)	Ref.
ALD	9.5	N_2/500 °C	TiN/TiN	17	1	[1]
ALD	40	N_2/500 °C/ 30 sec	Pt/TiN	11.4	1.4	[26]
Sputtering	40	N_2/700°C/ 1 min	TaN/TaN	10	1	[31]
Sputtering	30	N_2/750 °C/ 10 sec	Pt/TiN	9.5	1.6	[18]
PLD	7.7	650 °C	Pt/(LSMO /STO/Si(001)	15	2.8	[3]
MOCVD	16	N_2/700 °C/10 mins	Pt/Pt	5	2.5	[17]
CSD	40	N_2/700 °C/10 mins	Pt/Pt	2.1	0.6	[9]
CSD	40	N_2/700 °C/10 mins	Pt/Pt	8	-	[10]
CSD	33	Vacuum/800 °C/3 mins	Pt/Pt	15	1.2	This work

3.13. Conclusion

CSD Y-HZO films were deposited on platinized substrate and followed by annealing in vacuum, N_2 and O_2 environment. Effect of annealing temperature on vacuum, N_2 and O_2 annealed Y-HZO was demonstrated. Vacuum annealed sample shows good ferroelectric properties with increasing annealing temperature of Y-HZO films. Later ferroelectric properties of Y-HZO films annealed in various annealing environment at 800 ^{o}C was compared. It was found that Vacuum annealed Y-HZO films show good ferroelectric properties with clear hysteresis and switch current response due to lower leakage current as compared to samples annealed in the N_2 and O_2 environment. This chapter clearly demonstrates that the ferroelectric properties of Y-HZO films largely influenced by the annealing environment and annealing Y-HZO films in vacuum environment is an effective way in order to obtain good ferroelectric properties. P-E loops in this work is not good but comparable in terms of P_r, especially when thickness of HZO films is around 40 nm. Most of the previous reports requires PMA to observed ferroelectricity in HZO films whereas in this work ferroelectricity in Y-HZO can be observed even after PDA.

References

[1] J. Müller *et al.*, "Ferroelectricity in simple binary ZrO2and HfO2," *Nano Lett.*, vol. 12, no. 8, pp. 4318–4323, 2012, doi: 10.1021/nl302049k.

[2] X. Tian, S. Shibayama, T. Nishimura, T. Yajima, S. Migita, and A. Toriumi, "Evolution of ferroelectric HfO2 in ultrathin region down to 3 nm," *Appl. Phys. Lett.*, vol. 112, no. 10, 2018, doi: 10.1063/1.5017094.

[3] T. Li *et al.*, "Epitaxial ferroelectric Hf0.5Zr0.5O2 thin film on a buffered YSZ substrate through interface reaction," *J. Mater. Chem. C*, vol. 6, no. 34, pp. 9224–9231, 2018, doi: 10.1039/c8tc02941e.

[4] S. Starschich and U. Boettger, "An extensive study of the influence of dopants on the ferroelectric properties of HfO2," *J. Mater. Chem. C*, vol. 5, no. 2, pp. 333–338, 2017, doi: 10.1039/c6tc04807b.

[5] S. Starschich, D. Griesche, T. Schneller, and U. Böttger, "Chemical Solution Deposition of Ferroelectric Hafnium Oxide for Future Lead Free Ferroelectric Devices," *ECS J. Solid State Sci. Technol.*, vol. 4, no. 12, pp. P419–P423, Sep. 2015, doi: 10.1149/2.0061512jss.

[6] H. Liu *et al.*, "Structural and ferroelectric properties of Pr doped HfO2 thin films

fabricated by chemical solution method," *J. Mater. Sci. Mater. Electron.*, vol. 0, no. 0, p. 0, 2019, doi: 10.1007/s10854-019-00874-4.

[7] A. Wei, C. Chen, L. Tang, K. Zhou, and D. Zhang, "Chemical solution deposition of ferroelectric Sr:HfO2 film from inorganic salt precursors," *J. Alloys Compd.*, vol. 731, pp. 546–553, Jan. 2018, doi: 10.1016/j.jallcom.2017.09.264.

[8] X. Wang *et al.*, "Ferroelectric yttrium doped hafnium oxide films from all-inorganic aqueous precursor solution," *Ceram. Int.*, vol. 44, no. 12, pp. 13867–13872, 2018, doi: 10.1016/j.ceramint.2018.04.233.

[9] C. Abe *et al.*, "Crystal structure and dielectric/ferroelectric properties of CSD-derived HfO2-ZrO2 solid solution films," *Ceram. Int.*, vol. 43, no. May, pp. S501–S505, 2017, doi: 10.1016/j.ceramint.2017.05.253.

[10] S. Nakayama, H. Funakubo, and H. Uchida, "Crystallization behavior and ferroelectric property of HfO2-ZrO2 films fabricated by chemical solution deposition," *Jpn. J. Appl. Phys.*, vol. 57, no. 11, pp. 2–7, 2018, doi: 10.7567/JJAP.57.11UF06.

[11] T. Suzuki, T. Shimizu, T. Mimura, H. Uchida, and H. Funakubo, "Epitaxial ferroelectric Y-doped HfO 2 film grown by the RF magnetron sputtering," *Jpn. J. Appl. Phys.*, vol. 57, no. 11, pp. 1–2, 2018, doi: 10.7567/JJAP.57.11UF15.

[12] T. Shimizu *et al.*, "Contribution of oxygen vacancies to the ferroelectric behavior of Hf0.5Zr0.5O2 thin films," *Appl. Phys. Lett.*, vol. 106, no. 11, pp. 0–5, 2015, doi: 10.1063/1.4915336.

[13] M. H. Park, H. J. Kim, Y. J. Kim, W. Lee, H. K. Kim, and C. S. Hwang, "Effect of forming gas annealing on the ferroelectric properties of Hf 0.5 Zr 0.5 O 2 thin films with and without Pt electrodes," *Cit. Appl. Phys. Lett*, vol. 102, p. 112914, 2013, doi: 10.1063/1.4798265.

[14] M. Yano, Y. H. Hirofuji, M. K. Koyama, and K. K. Oike, "溶液塗布熱分解法で作製した Hf0.5Zr0.5O2薄膜の特性評価," *J. Soc. Mater. Sci.*, vol. 68, no. 10, pp. 745–750, 2019.

[15] Mohit, K. Haga, and E. Tokumitsu, "Electrical properties of yttrium-doped hafnium-zirconium dioxide thin films prepared by solution process for ferroelectric gate insulator TFT application," *Jpn. J. Appl. Phys.*, Jul. 2020, doi: 10.35848/1347-4065/ab86de.

[16] A. G. Chernikova *et al.*, "Improved Ferroelectric Switching Endurance of La-Doped Hf 0.5 Zr 0.5 O 2 Thin Films," *ACS Appl. Mater. Interfaces*, vol. 10, no. 3, pp. 2701–2708, 2018, doi: 10.1021/acsami.7b15110.

[17] C. Y. Huang, C. Y. Huang, T. L. Tsai, C. A. Lin, and T. Y. Tseng, "Switching mechanism of double forming process phenomenon in ZrOx/HfOy bilayer resistive switching memory structure with large endurance," *Appl. Phys. Lett.*, vol. 104, no. 6, 2014, doi: 10.1063/1.4864396.

[18] D.-H. Min, T.-H. Ryu, S.-J. Yoon, S.-E. Moon, and S.-M. Yoon, "Improvements in the synaptic operations of ferroelectric field-effect transistors using Hf0.5Zr0.5O2 thin films controlled by oxygen partial pressures during the sputtering deposition process," *J. Mater. Chem. C*, vol. 8, no. 21, pp. 7120–7131, 2020, doi: 10.1039/D0TC01105C.

[19] Y. Zhou *et al.*, “The effects of oxygen vacancies on ferroelectric phase transition of HfO2-based thin film from first-principle,” *Comput. Mater. Sci.*, vol. 167, no. March, pp. 143–150, 2019, doi: 10.1016/j.commatsci.2019.05.041.

[20] H. Chen *et al.*, “Obvious ferroelectricity in undoped HfO2 films by chemical solution deposition,” *J. Mater. Chem. C*, vol. 8, no. 8, pp. 2820–2826, 2020, doi: 10.1039/C9TC06400A.

[21] P. Jain and E. Tokumitsu, “Doctoral Thesis JAIST D-MS. 2019年度(R01) (Jun.2019 - Mar.2020),” p. 78, 2019, doi: 10.1088/1751-8113/44/8/085201.

[22] S. I. Ohmi, H. Yamamoto, J. Taguchi, K. Tsutsui, and H. Iwai, “Effects of post dielectric deposition and post metallization annealing processes on metal/Dy2O3/Si(100) diode characteristics,” *Japanese J. Appl. Physics, Part 1 Regul. Pap. Short Notes Rev. Pap.*, vol. 43, no. 4 B, pp. 1873–1878, 2004, doi: 10.1143/JJAP.43.1873.

[23] H. Yamamoto, S. I. Ohmi, and H. Iwai, “A Study on the Ultra-High Vacuum Anneal Method For the Rare Earth Gate Dielectrics,” p. 77, 2003, [Online]. Available: www.iwailab.ep.titech.ac.jp/pdf/200303mthesis/yamamoto.pdf.

[24] M. H. Park *et al.*, “Surface and grain boundary energy as the key enabler of ferroelectricity in nanoscale hafnia-zirconia: A comparison of model and experiment,” *Nanoscale*, vol. 9, no. 28, pp. 9973–9986, 2017, doi: 10.1039/c7nr02121f.

[25] D. Nečas and P. Klapetek, “Gwyddion: An open-source software for SPM data analysis,” *Cent. Eur. J. Phys.*, vol. 10, no. 1, pp. 181–188, 2012, doi: 10.2478/s11534-011-0096-2.

[26] H. J. Kim *et al.*, “Grain size engineering for ferroelectric Hf0.5Zr0.5O2 films by an insertion of Al2O3 interlayer,” *Appl. Phys. Lett.*, vol. 105, no. 19, pp. 1–6, 2014, doi: 10.1063/1.4902072.

[27] T. Mimura *et al.*, “Effects of heat treatment and in situ high-temperature X-ray diffraction study on the formation of ferroelectric epitaxial Y-doped HfO2 film,” *Jpn. J. Appl. Phys.*, vol. 58, no. SB, 2019, doi: 10.7567/1347-4065/aafed1.

[28] T. S. Böscke, J. Müller, D. Bräuhaus, U. Schröder, and U. Böttger, “Ferroelectricity in hafnium oxide thin films,” *Appl. Phys. Lett.*, vol. 99, no. 10, p. 102903, Sep. 2011, doi: 10.1063/1.3634052.

[29] T. S. Böscke *et al.*, “Phase transitions in ferroelectric silicon doped hafnium oxide,” *Appl. Phys. Lett.*, vol. 99, no. 11, pp. 10–13, 2011, doi: 10.1063/1.3636434.

[30] B. S. Kim *et al.*, “A Comparative Study on the Ferroelectric Performances in Atomic Layer Deposited Tetrakis (ethylmethylamino) and Tetrakis (dimethylamino) Precursors,” 2020.

[31] S. Migita, H. Ota, H. Yamada, K. Shubuya, A. Sawa and A. Torumi, Polarization switching behavior of Hf–Zr–O ferroelectric ultrathin films studied through coercive field characteristics,Jpn. J. Appl. Phys. 57 04FB01, (2018)

Chapter 4

Stability of ferroelectric phase in HZO films

A comparative study

4. Stability of ferroelectric phase in HZO films

4.1. Motivation

As discussed in Chapter 1, the ferroelectricity in HfO_2 films originates from the non-centrosymmetric $Pca2_1$ orthorhombic phase (o-phase). Therefore, the stabilization of o-phase is required during the device fabrication process for certain applications such as oxide channel ferroelectric gate transistor (FGT). Kim et al. observed ferroelectricity in 5 nm thick HZO films prepared by atomic layer deposition (ALD) even when the films re-annealed in case of MFM structure [1]. On the other hand, Migita et al. reported that the orthorhombic phase of sputtered HZO film was transferred to the monoclinic phase by further annealing for MFM structure [2]. However, an in-depth investigation on the re-annealing effect has not been reported yet for MFM and MFS structure. Oxide semiconductor channel FGT with bottom gate structure requires second time annealing or re-annealing for the oxide semiconductor channel. Therefore, the robustness of the ferroelectric properties of HZO becomes important.

Previously in this thesis, ferroelectric properties were demonstrated for solution-processed yttrium doped HZO (Y-HZO) films annealed in O_2 environment with solution-processed ITO as a top electrode with a relatively high-temperature annealing process [3]. It was found that ferroelectricity remained which was confirmed by P-V loops and C-V curves. Even though oxygen annealed Y-HZO films show rounded P-V loops due to high leakage, but the clear butterfly curves were observed in C-V curves which will be discussed later. In previous chapter 3, we discussed. P-E loops and leakage current of Y-HZO films prepared by chemical solution deposition (CSD) can be drastically improved by vacuum annealing of Y-HZO films [4]. In this chapter, a comparative study on stability of ferroelectricity of the sputtered HZO and CSD Y-HZO films in metal-ferroelectric-metal (MFM) and metal-ferroelectric-semiconductor (MFS) structure has been performed. In addition, effect of plasma damage on ferroelectric properties in MFM structure of the sputtered HZO and CSD Y-HZO films was also evaluated. A thin ITO layer, which corresponds to the channel layer of FGT, was deposited by sputtering on sputtered HZO and CSD Y-HZO films. Then, the fabricated MFM and MFS structures were annealed at 400 and 600 ^{O}C in N_2 for 15 min and the effect of the re-annealing process on ferroelectric properties of ferroelectric layer was evaluated.

4.2. Experimental

The sputtered HZO films were prepared in AIST as reported previously[2], [5]. Figure 4.1 shows fabrication process flow for MFM structure. At first, heavily doped n-type silicon was used as a substrate. Diluted HF solution was used to remove native oxide from the silicon surface. The bottom electrode TaN was deposited by DC sputtering on a silicon substrate, using Ta target and Ar/N_2 mixture gas. The thickness of TaN bottom electrode was 10 nm as shown in figure 4.1(b). Next, 10 nm thick $Hf_{0.54}Zr_{0.46}O_2$ film was deposited on TaN film by rf sputtering using the co-sputtering technique of HfO_2 and ZrO_2 targets as shown in figure 4.1(b). Then, the HZO/TaN/Si sample was annealed at 700 ^oC in an N_2 environment for 10 mins without a metal cap as shown in figure 4.1(c).

As described in chapter 2, a platinized silicon substrate (Pt/Ti/SiO_2/Si) with dimensions of 1.5×1.5 cm^2 was used to deposit thin films by CSD. The precursor solution was prepared using hafnium (IV) acetylacetonate (Hf(acac)$_4$), zirconium (IV) acetylacetonate (Zr(acac)$_4$), and yttrium (III) acetylacetonate (Y(acac)$_3$) as starting materials [3]. The source solution was prepared in air. First, a precursor solution of 5% Y-HZO was prepared by mixing Hf(acac)$_4$, Zr(acac)$_4$ and Y(acac)$_3$ in propionic acid for 1 h at 120 °C. Then, the precursor solution was spin-coated on a platinized substrate, followed by drying at 225 °C for 3 min in air[16].The crystallization was performed using rapid thermal annealing (RTA) at 800 °C for 3 min in a vacuum environment at 2.3 Pa as shown in figure 4.2 [4]. The thickness of the Y-HZO films was 33 nm. To evaluate the effect of plasma damage on sputtered HZO and CSD Y-HZO, Sample were exposed to plasma for 2 mins under O_2 gas flow with shutter close. A top electrode of Pt with a thickness of 100 nm and a diameter of 250 μm was deposited through a metal mask using sputtering on CSD Y-HZO and sputtered HZO for MFM structure as shown in Fig 1(d) and fig 2(c). Then, the samples were re-annealed in RTA at 400 and 600 ^oC for 15 min in N_2 atmosphere for MFM structure (without plasma exposure and with plasma exposure).

To fabricate MFS structures, 7.5 percent doped indium-tin-oxide (ITO) was deposited at room temperature by RF sputtering on a thickness of 10 nm on sputtered HZO and CSD Y-HZO films. as shown in figure 4.3(e) and 4.4(c). Then, the samples were re-annealed in RTA at 400 and 600 ^oC for 15 min in N_2 atmosphere as shown in figure 4.3(e) and 4.4(c). The sample without re-annealing process was also fabricated for comparison. Top Pt electrodes are patterned by the lift-off process as shown in Figs. 1 (a) and (d), and the area of the MFS structures was 10000 μm^2 as shown in figure 3(f) and 4(d).

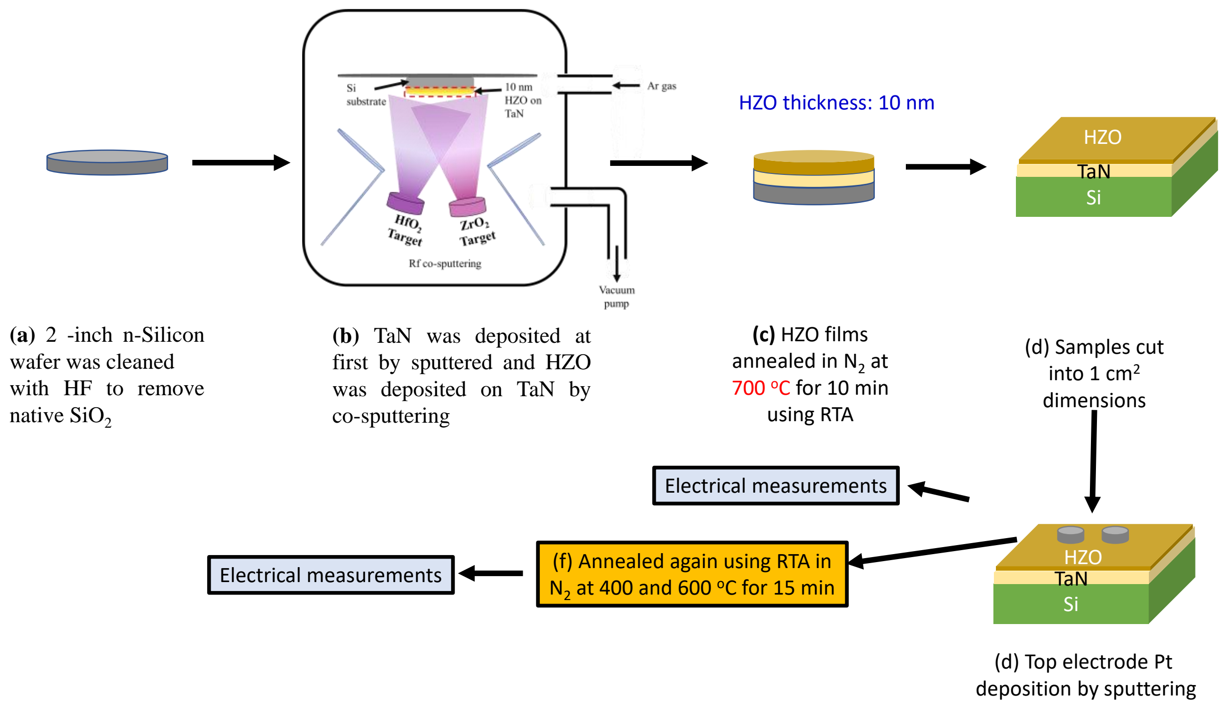

Figure 4.1 Fabrication process flow of MFM structure of Sputtered HZO (a) Cleaning of Si wafer (b) Deposition of TaN and HZO by sputtering (c) Crystallization of HZO at 700 °C in N_2 (d) cutting wafter into smaller substrate (e)

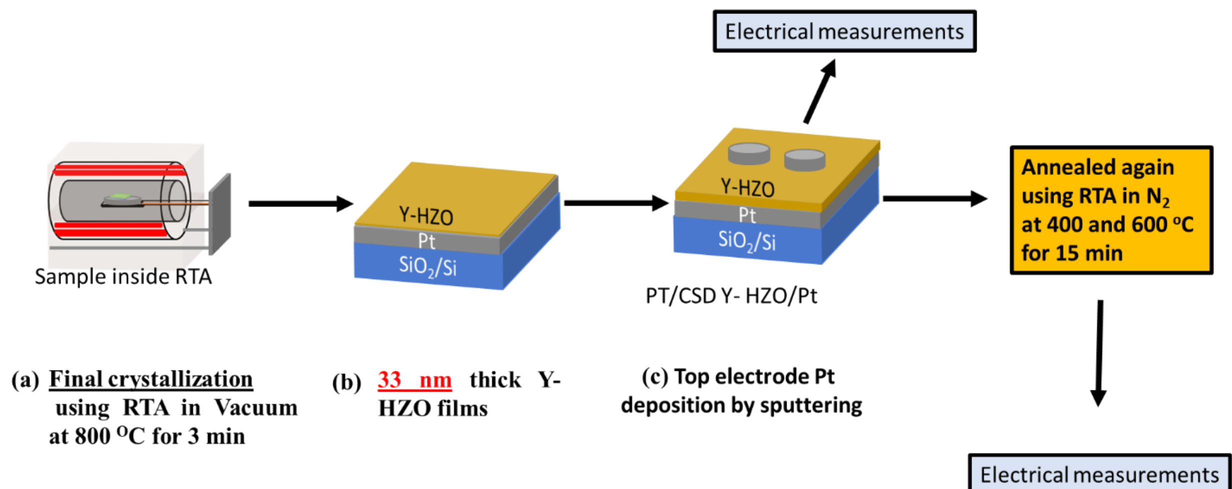

Figure 4.2 Fabrication process flow of MFM CSD Y-HZO structure (a) Crystallization of Y-HZO using XRD (b) Y-HZO film after crystallization (c) Top electrode Pt deposition by sputtering

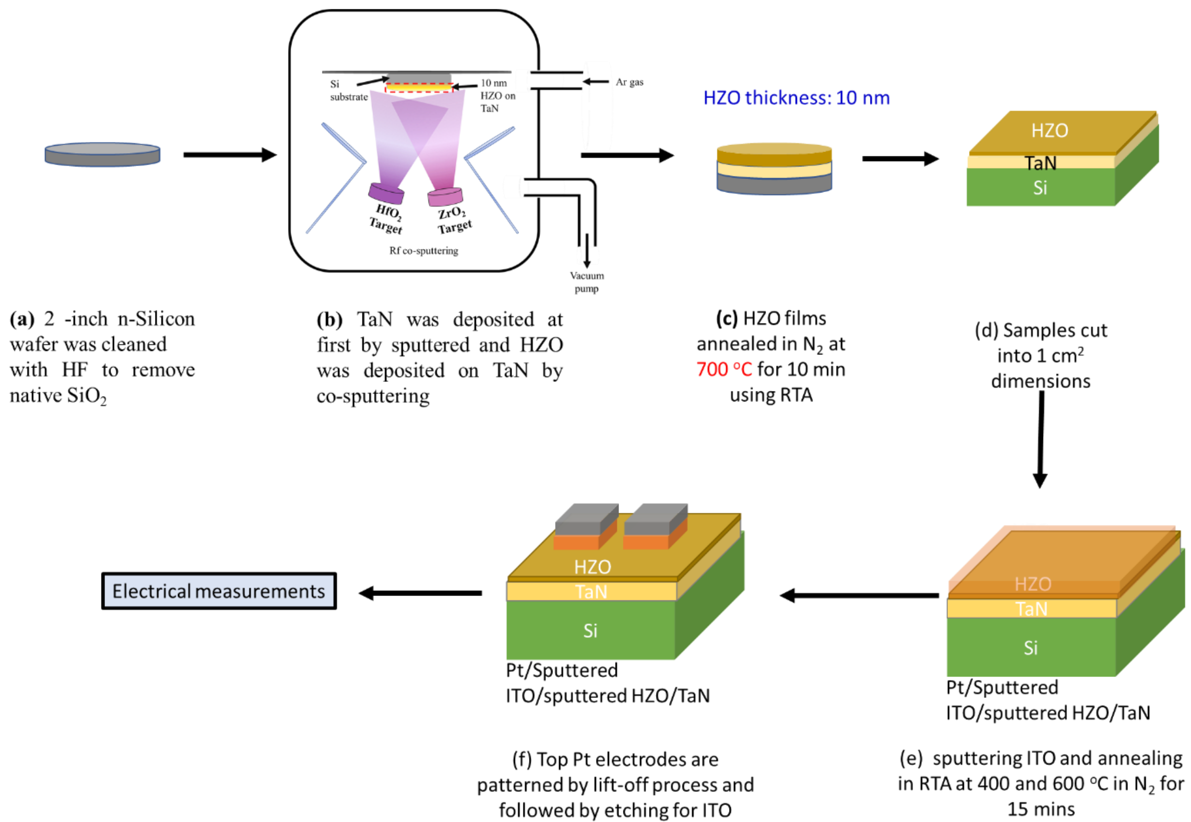

Figure 4.3 Fabrication process flow of MFS structure of Sputtered HZO (a) Cleaning of Si wafer (b) Deposition of TaN and HZO by sputtering (c) Crystallization of HZO at 700 °C in N_2 (d) cutting wafter into smaller substrate (e) deposition of ITO by sputtered on sputtered HZO (f) top Pt electrodes are patterned by etching ITO.

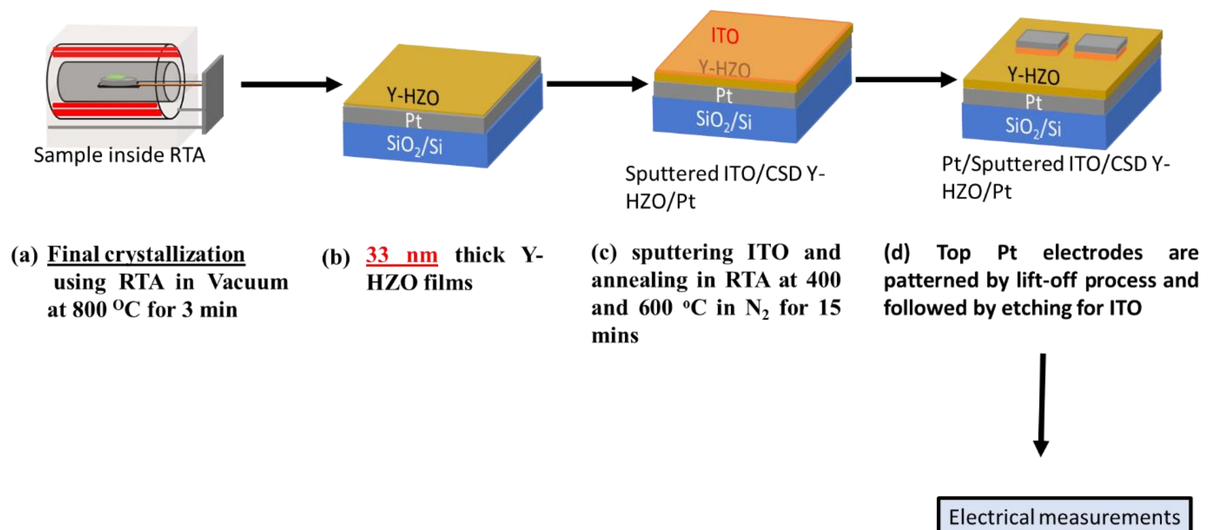

Figure 4.4 Fabrication process flow of MFS CSD Y-HZO structure (a) Crystallization of Y-HZO using XRD (b) Y-HZO film after crystallization (c) Top electrode Pt deposition by sputtering. deposition of ITO by sputtered on sputtered HZO (d) top Pt electrodes are patterned by etching ITO.

4.3. Crystallinity of films

The XRD patterns of sputtered HZO films for MFM (without plasma exposure), MFM structure (with plasma exposure) and MFS structure are shown in Fig. 4.5(a.), 4.5(b) and 4.5(c) respectively. Pt/sputtered HZO/TaN MFM structure (without plasma exposure) no re-annealed (black line) shows a diffraction peak around 30.5^o which corresponds to 111 of the O-phase or tetragonal phase (T-phase) or cubic phase (C-phase). A diffraction peak of around 28.5 ^{o} with relatively low intensity was also observed which corresponds to 111 of the monoclinic phase (M-phase). Hence, it is confirmed the sputtered HZO film annealed at 700 ^{o}C in N_2 has O/T/C phase along with M-phase. But when sample were re-annealed at 400 and 600 ^{o}C, the peak intensity of 28.5^o increased which correspond to 111 of M-phase of HZO. In case of MFM structure (with plasma exposure), diffraction peak results show transfer of crystalline phase to 111 of M-phase even before the re-annealing and the peak intensity increased when re-annealed at 400 and 600 ^{o}C too. When the ITO layer was deposited, as shown in the black line (Pt/ITO/sputtered HZO/TaN MFS structure) of Fig.5(c), both diffraction peaks around 28.5 ^{o} and 30.5 ^{o} were observed. It is interesting to note that the peak intensity of 28.5^o peak increased which correspond to 111 of M-phase of HZO. In addition, a peak around 30.5^o corresponds to 111 of O/T/C-phase of HZO films or 222 of cubic bixbyite of ITO layer. As expected, result shows crystalline phase of the sputtered HZO film was affected by the deposition of ITO layer even before re-annealing process. After the sample was re-annealed at 400 ^{o}C, the diffraction peak intensity at 28.5^o increases, which suggests the M-phase was increased by the re-annealing. Note that the peak around 30.5^o is partly due to the ITO layer. When the sample was annealed at 600 ^{o}C, the diffraction peak at at 28.5^o was observed, which suggests the presence of M-phase. In addition, peak intensities are decreased, which suggests degradation of crystallinity as the electrical properties are discussed later.

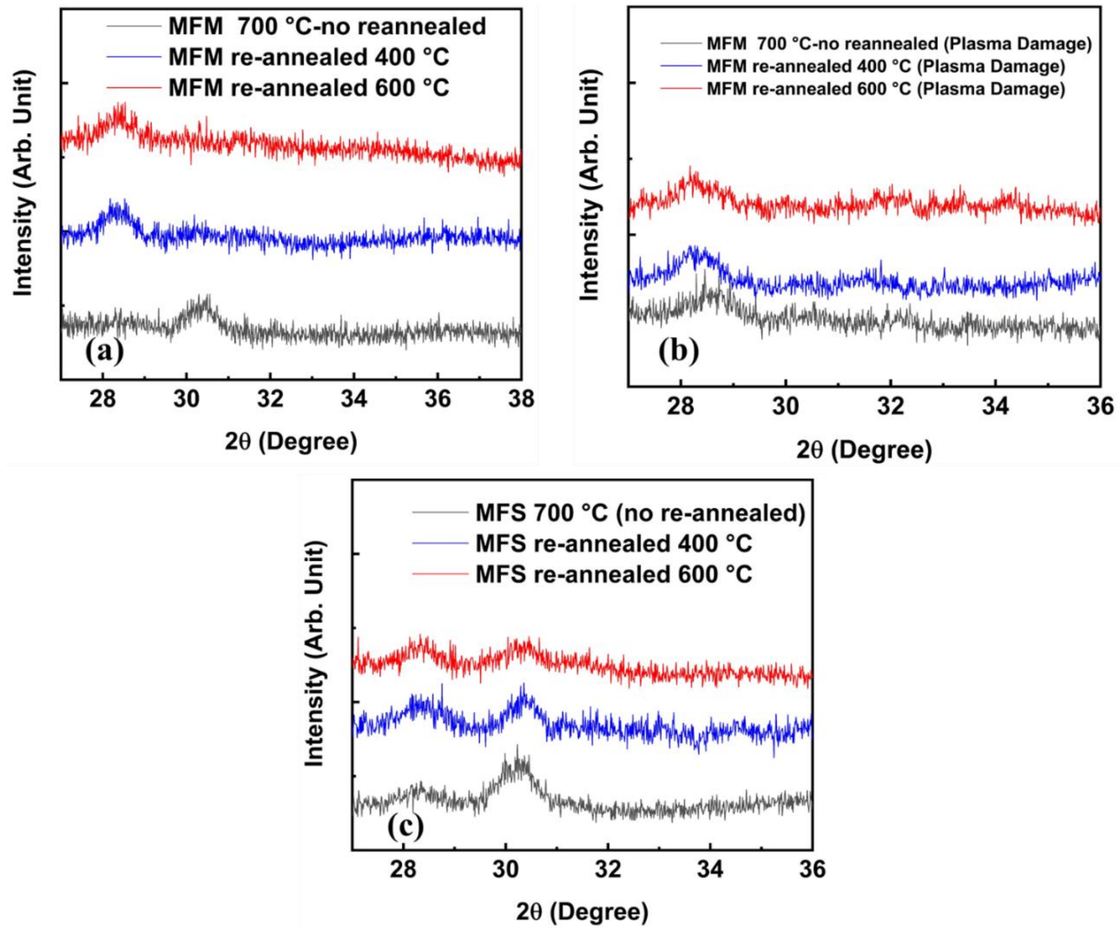

Fig. 4.5. XRD patterns of sputtered HZO (a) MFM structure (without plasma exposure) (b) MFM (with plasma exposure) (c) MFS structure.

Figure 6 (a), (b) and (c) shows CSD Y-HZO films for MFM (without plasma exposure), MFM structure (with plasma exposure) and MFS structure, respectively. All samples show a diffraction peak around 30.5 which corresponds to 111 of O/T/C-phase of CSD Y-HZO or 222 of cubic bixbyite of ITO in as of MFS. It is worth noting that negligible M-phase is observed for all samples of CSD Y-HZO films even after the re-annealing process of the MFS structure. This indicates the O-phase of the Y-HZO films prepared by CSD are robust against the plasma exposure and the re-annealing process.

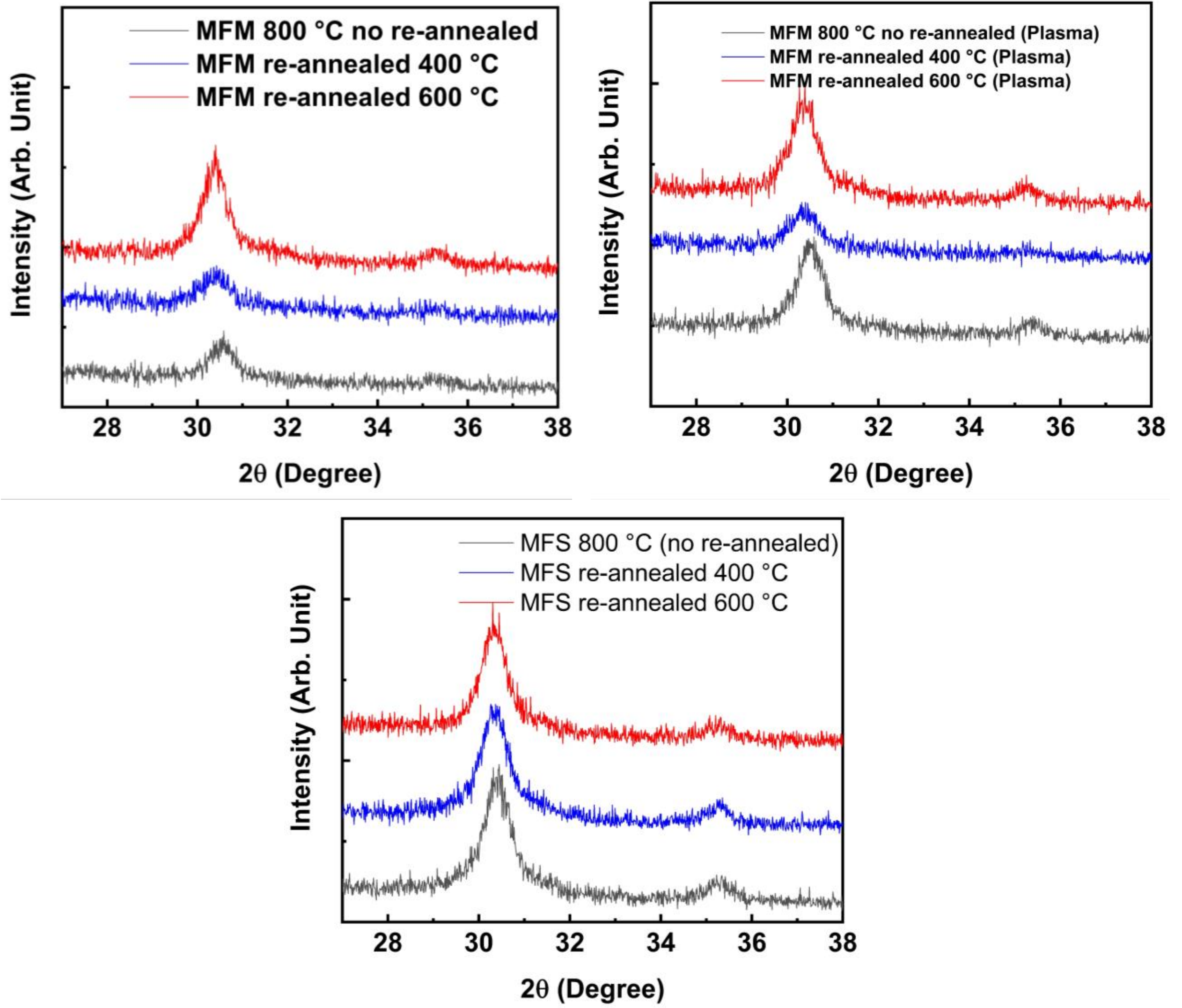

Fig. 4.6. XRD patterns of CSD Y-HZO (a) MFM (without plasma exposure) (b) MFM (with plasma exposure) (c) MFS.

4.4. Electrical properties

4.4.1. Sputtered HZO

4.4.1.1. MFM (without plasma exposure)

To confirm the ferroelectricity, P-E characteristics were measured for sputtered HZO for MFM structure. Figures 4.7(a), 4.7(c) and 4.7(e) show P-E loops of sputtered HZO with the corresponding current response of sputtered HZO MFM no re-annealing, re-annealing 400 and 600 ^{o}C, respectively. Ferroelectric nature was observed with clear hysteresis and switching response for sputtered HZO without re-annealing sample, which is consistent with previous

report[2], [5]. The remnant polarization (P_r) and coercive field (E_C) of sputtered HZO for MFM structure deduced from Figs. 7(a) are approximately 3.6 μC/cm^2 and 1.1 MV/cm.

When the sample were re-annealed at 400 and 600 ^{o}C, P-E loops shows linear response to applied electric field due to paraelectric nature of sputtered HZO which is consistent with XRD results. When re-annealing temperature increased to 600 ^{o}C, the dielectric constant becomes smaller, suggesting sputtered HZO films have been affected by thermal damage.

In addition to P-V loops, C-V measurements were carried. Figures 4.7(b), 4.7(d), and 4.7(e) show C-V curves of Pt/sputtered HZO films without re-annealing, with re-annealed at 400 ^{o}C and 600 ^{o}C in N_2 for 15 min, respectively. C-V curves show clear butterfly shape due to ferroelectric nature for sample without re-annealed as shown in figure 4.7 (b). On contrary, C-V curves shows a straight line for the samples re-annealed at 400 ^{o}C and 600 ^{o}C due to the paraelectric nature of sputtered HZO films as shown in Figs. 4.7(d) and 4.7(f).

.

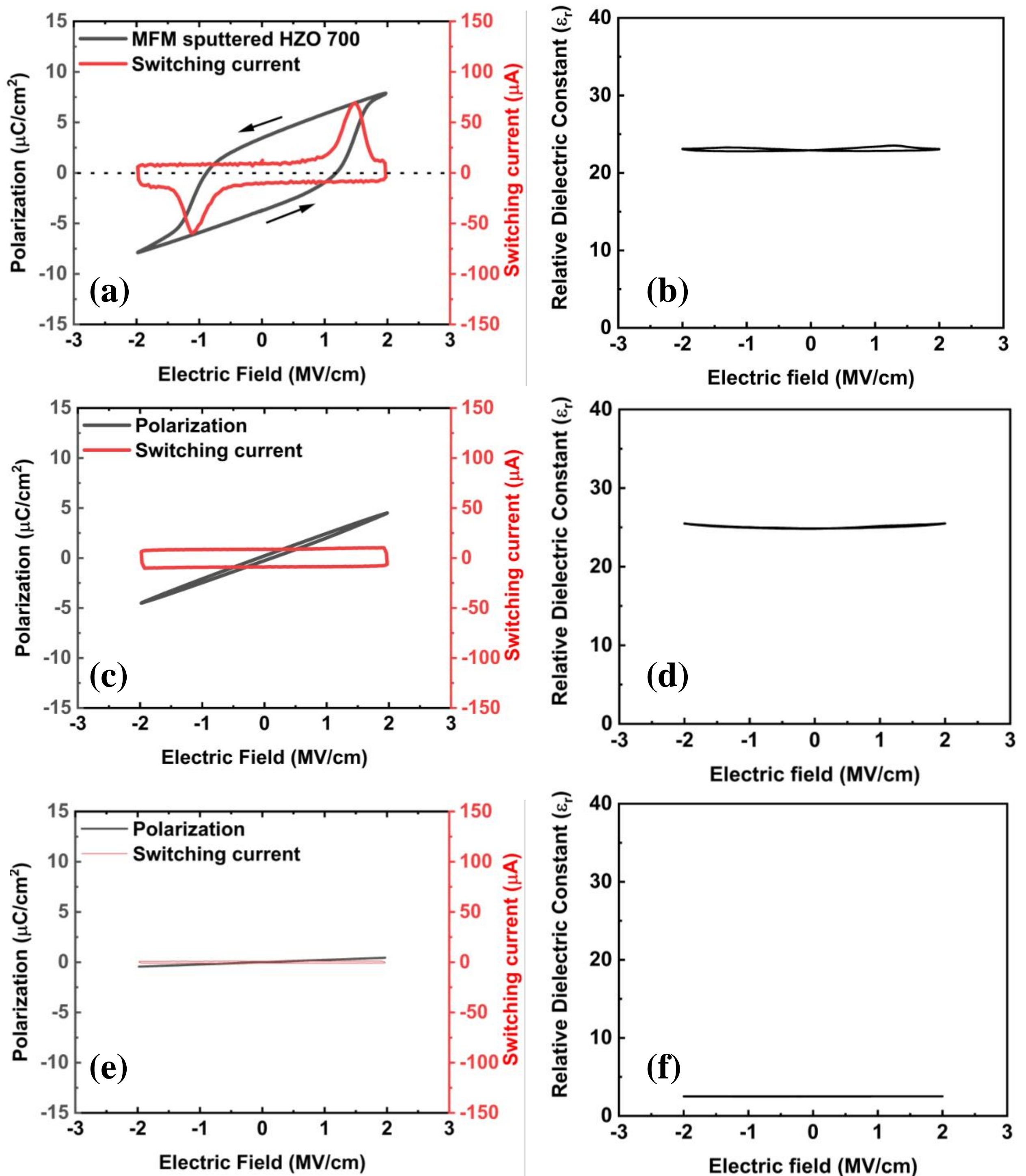

Figure 4.7 Electrical properties of MFM structure with sputtered HZO (without plasma exposure) (a) P-E loop and (b) C-V curve of the sample without re-annealing, (c) P-E loop and (d) C-V curve of the sample re-annealed at 400 ^{o}C in N_2 for 15 min. (e) P-E loop and (f) C-V curve of the sample re-annealed at 600 ^{o}C in N_2 for 15 min.

4.4.1.2.Sputtered HZO MFM plasma damage

To confirm the effect of plasma, P-E measurement were carried out for sputtered HZO for MFM structure. Figures 4.8(a), 4.8(c) and 4.8(e) show P-E loops of sputtered HZO with the corresponding current response of sputtered HZO MFM no re-annealing, re-annealing 400 and 600 ^{o}C, respectively. Surprisingly, all samples show paraelectric nature was observed with linear hysteresis and no switching response for sputtered HZO probably due to plasma damage. When re-annealing temperature increased to 600 ^{o}C, the dielectric constant becomes smaller, suggesting sputtered HZO films have affected by thermal damage.

To confirm the paraelectric nature and plasma damage, C-V measurements were carried. Figures 4.8(b), 4.8(d), and 4.8(e) show C-V curves of Pt/sputtered HZO films without re-annealing, with re-annealed at 400 ^{o}C and 600 ^{o}C in N_2 for 15 min respectively. C-V curves shows a straight line for all samples due to the paraelectric nature of sputtered HZO films.

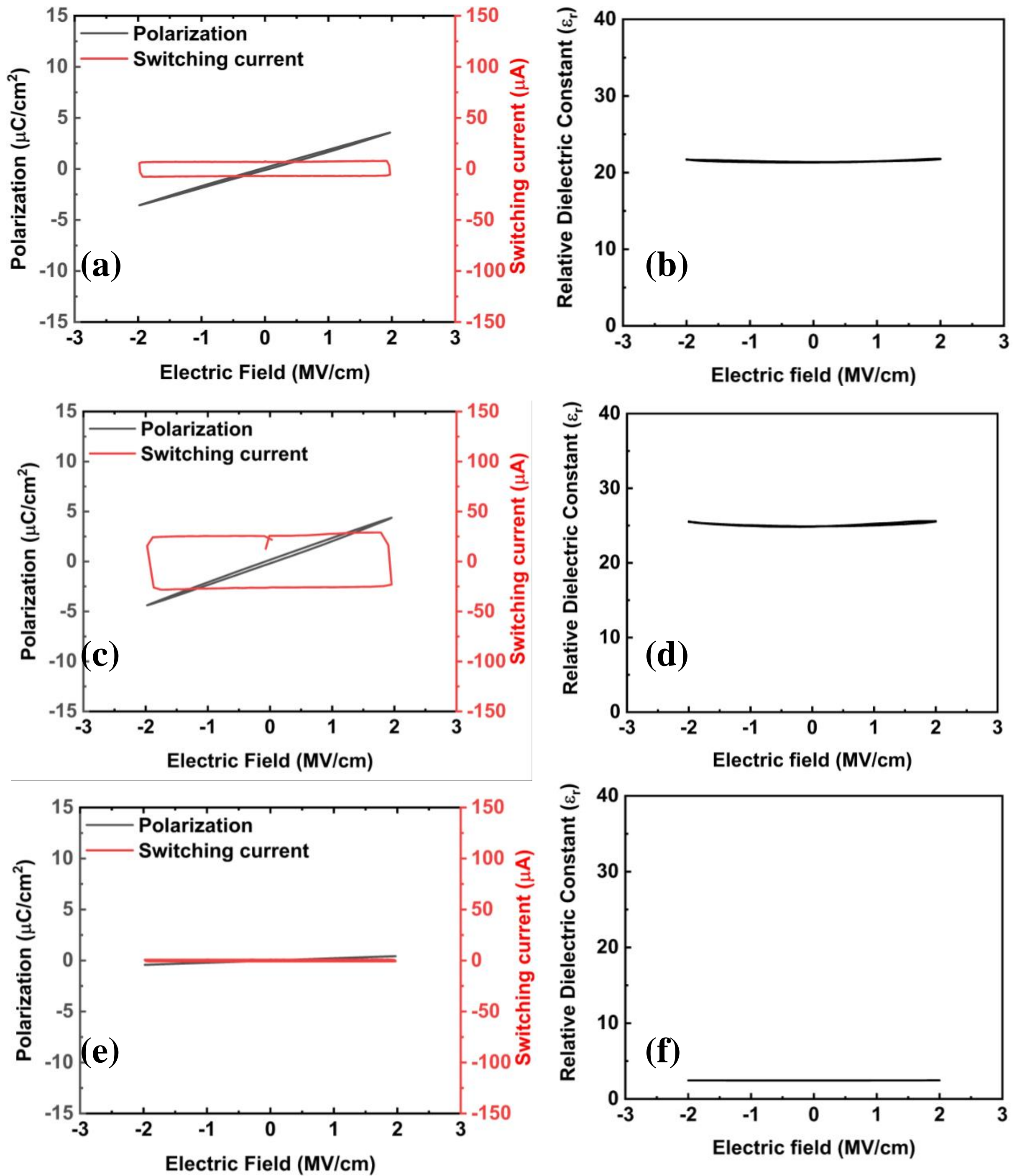

Figure 4.8 Electrical properties of MFM structure with sputtered HZO (plasma damage) (a) P-E loop and (b) C-V curve of the sample without re-annealing, (c) P-E loop and (d) C-V curve of the sample re-annealed at 400 ^{o}C in N_2 for 15 min. (e) P-E loop and (f) C-V curve of the sample re-annealed at 600 ^{o}C in N_2 for 15 min.

4.4.1.3.MFS

To clarify the effect of re-annealing on ferroelectricity, P-V and C-V measurement of MFS structure were carried out for sputtering HZO films with ITO. Since the thin ITO layer may be depleted in the MFS structure, we use voltage instead of electric field as horizontal axis. Figures 4.9(a), 4.9(c) and 4.9(e) shows P-V loops with the switching current of ITO/sputtered HZO MFS structure without re-annealing, with re-annealed at 400 ^{o}C, and 600 ^{o}C in N_2 for 15 min, respectively. Paraelectric nature was confirmed for all samples from P-V loops with no switching current. Surprisingly, sputtered HZO films just after the ITO deposition without re-annealing shows paraelectric nature probably due to the plasma damage. With increasing re-annealing temperature, the dielectric constant becomes smaller, suggesting sputtered HZO films have affected by thermal damage

In addition to P-V loops, C-V measurements were carried. Figures 4.9(b), 4.9(d), and 4.9(e) show C-V curves of ITO/sputtered HZO films without re-annealing, with re-annealed at 400 ^{o}C and 600 ^{o}C in N_2 for 15 min respectively. C-V curves shows a straight line for the samples re-annealed at 400 ^{o}C and 600 ^{o}C due to the paraelectric nature of sputtered HZO films as shown in Figs. 4.9(d) and 4.9(f). In the case of the MFS structure without re-annealing, the decrease in capacitance is observed on the positive voltage side due to the depletion of ITO with a hysteresis, because the carrier concentration of as deposited ITO without annealing is not so high. However, the C-V loop shows charge-injection type hysteresis whose direction is opposite to ferroelectric hysteresis. Equivalent dielectric constants (ε_r) were deduced from Figs. 9(b), 9(d) and 9(e), these are 19.3, 14.6 and 2.5 respectively. Low ε_r values suggest that the monoclinic phase becomes dominant which shows good agreement with XRD peaks. Dielectric constant value decreases with increasing re-annealing temperature from 400 to 600 ^{o}C which indicates that sputtered HZO films are vulnerable to thermal damage.

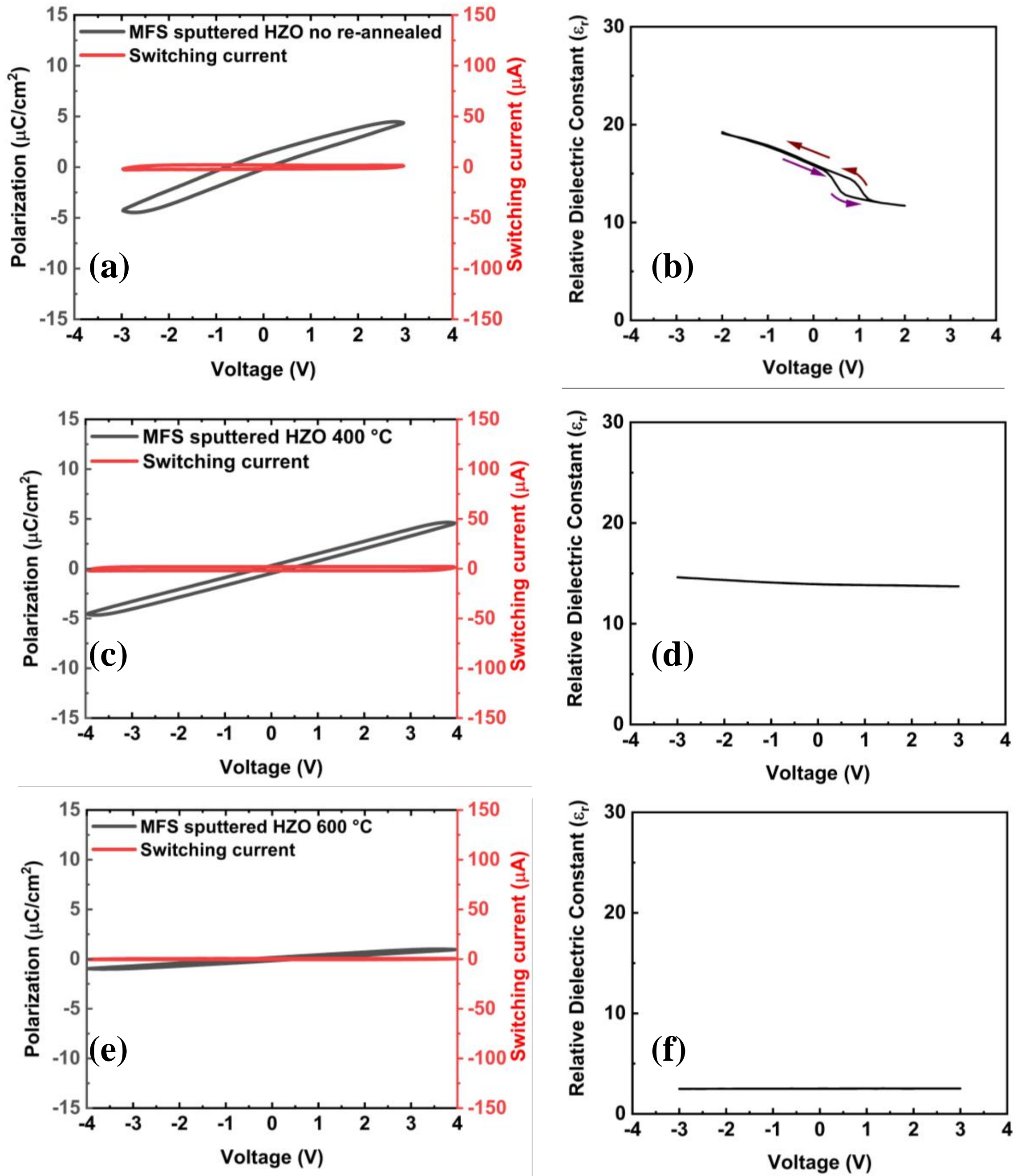

Figure 4.9 Electrical properties of MFS structure with sputtered HZO (a) P-V loop and (b) C-V curve of the sample without re-annealing, (c) P-V loop and (d) C-V curve of the sample re-annealed at 400 ^{o}C in N_2 for 15 min. (e) P-V loop and (f) C-V curve of the sample re-annealed at 600 ^{o}C in N_2 for 15 min.

4.4.2. CSD Y-HZO

4.4.2.1.MFM (without plasma exposure)

To confirm the ferroelectricity, P-E characteristics were measured for CSD Y-HZO for MFM structure (without Plasma exposure). Figures 4.10(a), 4.10(c) and 4.10(e) show P-E loops of with switching current of MFM CSD Y-HZO films without re-annealing, with re-annealing at 400 and 600 ^{o}C in N_2 for 15 min, respectively. P-E loops shows clear hysteresis loops with the clear switching current for without re-annealing sample. When samples re-annealed at 400 and 600 °C show rounded P–E loops due to leakage current. However, we can see the trace of switching current response due to ferroelectric nature. The remnant polarization (P_r) and coercive field (E_C) of sputtered HZO for MFM structure deduced from Fig. 4.10 (a) are approximately 4.4 μC/cm^2 and 0.9 MV/cm, respectively.

In addition to P-E loops, C-V curves were also measured to further confirm ferroelectricity of MFM CSD Y-HZO. Figures 4.10(b), 4.10(d) and 4.10(f) show the *C–V* curves of MFM CSD Y-HZO films without re-annealing, with re-annealing at 400 and 600 ^{o}C in N_2 for 15 min, respectively, demonstrating a clear butterfly shape due to the ferroelectric nature of Y-HZO films. The coercive field E_c was estimated from the peaks, and these were 1.1 MV cm^{-1}, 1 MV cm^{-1} and 0.9 MV cm^{-1} of MFM CSD Y-HZO films without re-annealing, with re-annealing at 400 and 600 ^{o}C in N_2 for 15 min, respectively. Therefore, CSD Y-HZO show stable ferroelectric properties before and after re-annealing.

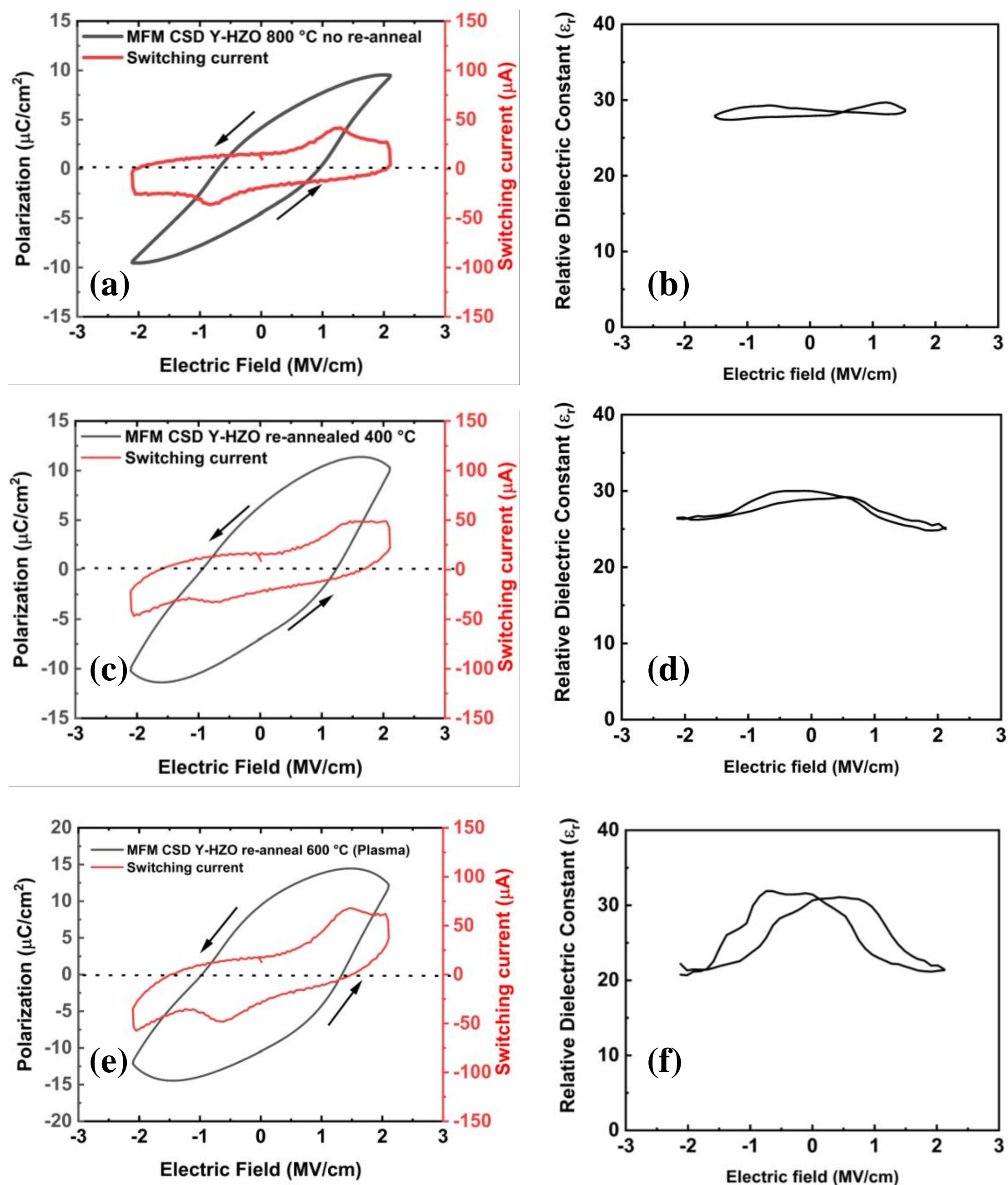

Figure 4.10 Electrical properties of MFM structure with CSD Y-HZO (a) P-E loop and (b) C-V curve of the sample without re-annealing, (c) P-E loop and (d) C-V curve of the sample re-annealed at 400 ^{o}C in N_2 for 15 min. (e) P-E loop and (f) C-V curve of the sample re-annealed at 600 ^{o}C in N_2 for 15 min.

4.4.2.2.MFM (with plasma exposure)

To confirm the ferroelectricity, P-E characteristics were measured for CSD Y-HZO for MFM structure (with Plasma exposure). Figures 4.11(a), 4.11(c) and 4.11(e) show P-E loops of with switching current of MFM CSD Y-HZO films without re-annealing, with re-annealing at 400 and 600 ^{o}C in N_2 for 15 min, respectively. P-E loops shows clear hysteresis loops with the clear switching current for without re-annealing sample. When samples re-annealed at 400 and 600 °C show rounded P–E loops due to leakage current too. However, we can see the trace of switching current response due ferroelectric nature. The origin of leakage current in MFM structure may be due to interface defects such as interface oxygen vacancies. The remnant polarization (P_r) and coercive field (E_C) of sputtered HZO for MFM structure deduced from Figs. 4.10 (a) are approximately 4 μC/cm^2 and 0.9 MV/cm, respectively.

In addition to P-E loops, C-V curves were also measured to further confirm ferroelectricity of MFM CSD Y-HZO (with Plasma exposure). Figures 4.11(b), 4.11(d) and 4.11(f) show the *C–V* curves of MFM CSD Y-HZO films without re-annealing, with re-annealing at 400 and 600 ^{o}C in N_2 for 15 min, respectively, demonstrating a clear butterfly shape due to the ferroelectric nature of Y-HZO films. The coercive field E_c was estimated from the peaks, and these were 1.1 MV cm^{-1}, 1 MV cm^{-1} and 0.9 MV cm^{-1} of MFM CSD Y-HZO films without re-annealing, with re-annealing at 400 and 600 ^{o}C in N_2 for 15 min, respectively. Therefore, CSD Y-HZO show stable ferroelectric properties before and after re-annealing and stable towards plasma damage.

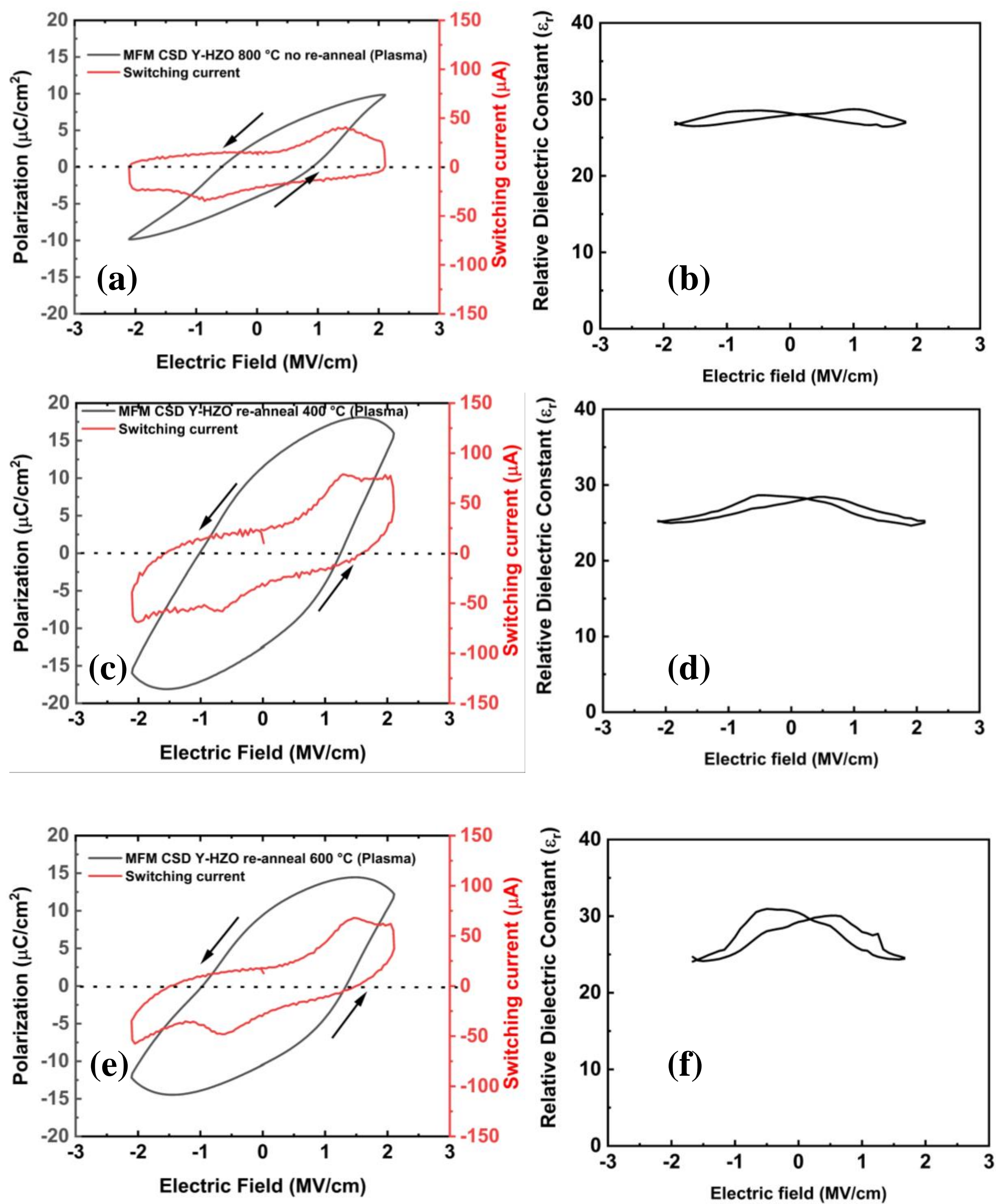

Figure 4.11 Electrical properties of MFM structure (with plasma exposure) with CSD Y-HZO (a) P-E loop and (b) C-V curve of the sample without re-annealing, (c) P-E loop and (d) C-V curve of the sample re-annealed at 400 ^{o}C in N_2 for 15 min. (e) P-E loop and (f) C-V curve of the sample re-annealed at 600 ^{o}C in N_2 for 15 min

4.4.2.3.MFS

Next, ferroelectric properties of CSD Y-HZO films of MFS structure were measured. Figures 4.12 (a), 4.12 (c), and 4.12 (e) shows P-V loops with switching current of ITO/sputtered HZO/CSD Y-HZO films without re-annealing, with re-annealing at 400 and 600 ^oC in N_2 for 15 mins, respectively. P-V loops shows clear hysteresis loops with the clear switching current for all samples. It is worth emphasizing that good ferroelectric properties were observed even after the re-annealing the MFS structure at 600 ^oC. P-V loops tend to improve for the MFS structure shown in Fig. 4.12(a) as compared to MFM structure shown in Fig. 4.10(a), presumably due to improvement of interface between top Pt electrode and CSD Y-HZO by inserting ITO, or capping effect of ITO [6]. The remnant polarization (P_r) and coercive field (E_C) of sputtered HZO and CSD Y-HZO for MFS structure deduced from Fig. 4.12(a), 4.12(c), and 4.12(e), and these are approximately 11 μC/cm^2 and 1.4 MV/cm^2, 9.0 μC/cm^2 and 1.3 MV/cm^2, 9.5 μC/cm^2 and 1.3 MV/cm^2 respectively. These results indicate that ferroelectricity in CSD Y-HZO is stable even after the-re-annealing and no plasma damage is observed.

To further confirm the stability of ferroelectric properties in CSD Y-HZO, C-V measurement was carried out. Figs. 4.12(b), 4.12(d), and 4.12(e) shows C-V curves of CSD Y-HZO without re-annealing, re-annealed at 400, and 600 ^oC in N_2 for 15 mins, respectively. All samples show clear butterfly loops with a decrease in capacitance on the positive voltage side due to the depletion of ITO layer. It was found by Hall measurements that the carrier concentration of ITO annealed 600 ^oC is 1.6 x 10^{20} cm^{-3} which is slightly higher than ITO annealed at 400 ^oC (1.1 x 10^{20} cm^{-3}). The Equivalent dielectric constants (ε_r) deduced from Figs. 4.12(b), 4.12(d) and 4.12(e), are 23.9, 23.5 and 23.8 at -11 V, respectively. It is clear from these values that Y-HZO films are stable to the plasma and thermal treatments.

CSD Y-HZO films have robust ferroelectric properties compared to the sputtered HZO films, presumably due to the residual carbon in the films. It was found from secondary ion mass spectrometry that the residual carbon content of CSD Y-HZO films were as large as 5%.[4], [7] Such a large amount of carbon content could help prevent the formation of low symmetry phase or m-phase[8]. In addition, we previously observed that oxygen vacancies exist in the vacuum annealed CSD Y-HZO film which shows good ferroelectric properties [4] from the O 1s spectrum measured by X-ray photoelectron spectrometry (XPS). On the other hand, it was found that the oxygen vacancy related peak of O 1s spectrum for the sputtered HZO film was much less than that of the CSD Y-HZO film as shown in Fig. 4.13. A theoretical consideration suggests that the presence of the oxygen vacancies is preferable to stabilize the O-phase of

HfO_2-based ferroelectrics[9]. Such a difference is one of the reasons for robust ferroelectricity in the CSD-YHZO films. Furthermore, since we observed clear depletion of the ITO layer in MFS structure when we used the CSD Y-HZO, transistor operation is expected, which will be discussed in next chapter.

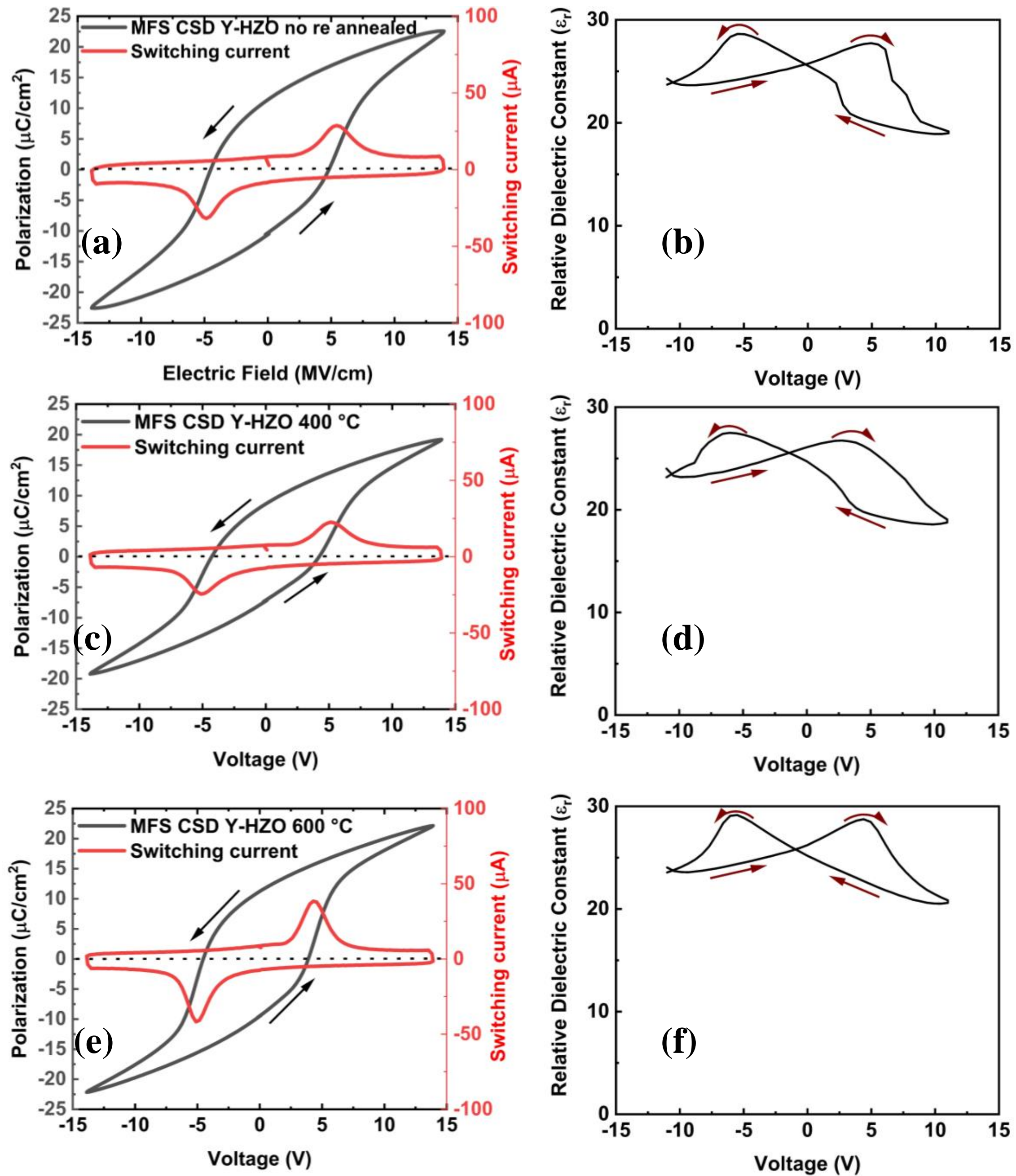

Figure 4.12. Electrical properties of MFS structure with CSD Y-HZO (a) P-V loop and (b) C-V curve of the sample without re-annealing, (c) P-V loop and (d) C-V curve of the sample re-annealed at 400 ^oC in N_2 for 15 min. (e) P-V loop and (f) C-V curve of the sample re-annealed at 600 ^oC in N_2 for 15 min.

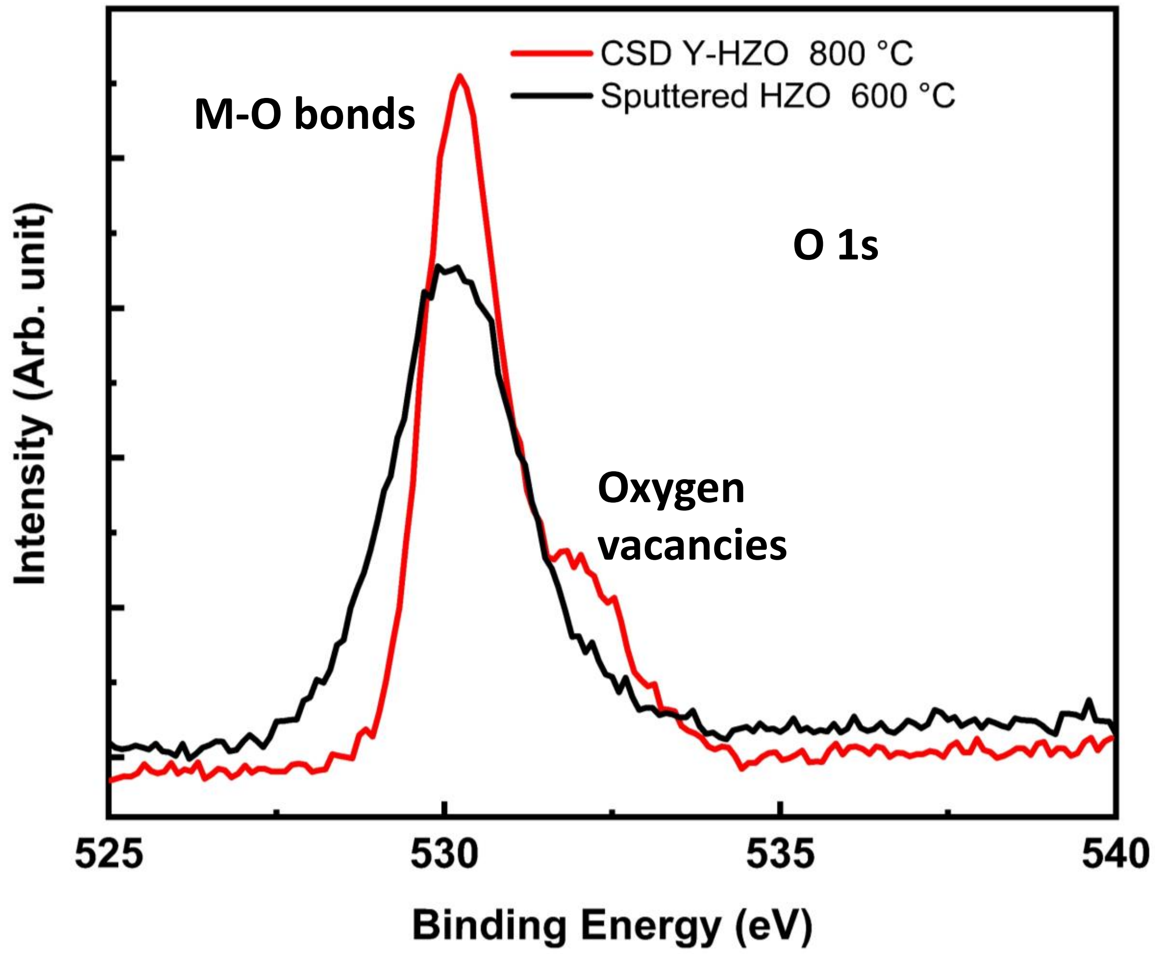

Figure 4.13 O 1s XPS spectra of CSD Y-HZO 800 ºC and Sputtered HZO 600 ºC

4.5. Conclusion

The stability of ferroelectricity of the MFM (without plasma exposure), MFM (with plasma damage), and MFS structures with sputtered HZO and CSD Y-HZO films was investigated. A thin ITO layer is deposited by sputtering on sputtered HZO or CSD Y-HZO to fabricate MFS structures. It was found that the sputtered HZO becomes paraelectric after re-annealing, MFM (without plasma exposure), MFM (with plasma damage) and MFS structure at 400 and 600°C in N_2 for 15 min. Paraelectric behavior was observed even in MFM (with plasma damage) and MFS structure after the ITO deposition before the re-annealing process. On the other hand, it was demonstrated that the CSD Y-HZO films have robust ferroelectric properties even after the re-annealing process at 600°C. C-V curves of the MFS structure with CSD Y-HZO clearly showed ferroelectric hysteresis with depletion of the ITO semiconducting layer. Therefore, the CSD Y-HZO films are promising for oxide channel ferroelectric gate transistor application.

References.

[1] S. J. Kim *et al.*, "Low-voltage operation and high endurance of 5-nm ferroelectric Hf 0.5 Zr 0.5 O 2 capacitors," *Cit. Appl. Phys. Lett*, vol. 113, p. 182903, 2018, doi: 10.1063/1.5052012.

[2] S. Migita *et al.*, "Phase transformation behavior of ultrathin Hf0.5Zr0.5O2 films investigated through wide range annealing experiments," *Jpn. J. Appl. Phys.*, vol. 58, no. SB, pp. 0–6, 2019, doi: 10.7567/1347-4065/ab00f6.

[3] Mohit, K. Haga, and E. Tokumitsu, "Electrical properties of yttrium-doped hafnium-zirconium dioxide thin films prepared by solution process for ferroelectric gate insulator TFT application," *Jpn. J. Appl. Phys.*, Jul. 2020, doi: 10.35848/1347-4065/ab86de.

[4] Mohit, T. Murakami, K. Haga, and E. Tokumitsu, "Impact of annealing environment on electrical properties of yttrium-doped hafnium zirconium dioxide thin films prepared by the solution process," *Jpn. J. Appl. Phys.*, vol. 59, no. SP, p. SPPB03, Nov. 2020, doi: 10.35848/1347-4065/aba50b.

[5] X. Tian, S. Shibayama, T. Nishimura, T. Yajima, S. Migita, and A. Toriumi, "Evolution of ferroelectric HfO2 in ultrathin region down to 3 nm," *Appl. Phys. Lett.*, vol. 112, no. 10, 2018, doi: 10.1063/1.5017094.

[6] F. Mo, T. Saraya, T. Hiramoto, and M. Kobayashi, "Reliability characteristics of metal/ferroelectric-HfO 2 /IGZO/metal capacitor for non-volatile memory application," 2020, doi: 10.35848/1882-0786/ab9a92.

[7] M. Mohit, K. Haga, and E. TOKUMITSU, "Electrical properties of yttrium-doped hafnium-zirconium dioxide thin films prepared by solution process for ferroelectric gate insulator TFT application.," *Jpn. J. Appl. Phys.*, 2020, doi: 10.35848/1347-4065/ab86de.

[8] H. Chen *et al.*, "Obvious ferroelectricity in undoped HfO2 films by chemical solution deposition," *J. Mater. Chem. C*, vol. 8, no. 8, pp. 2820–2826, 2020, doi: 10.1039/C9TC06400A.

[9] Y. Zhou *et al.*, "The effects of oxygen vacancies on ferroelectric phase transition of HfO2-based thin film from first-principle," *Comput. Mater. Sci.*, vol. 167, no. March, pp. 143–150, 2019, doi: 10.1016/j.commatsci.2019.05.041.

Chapter 5

Indium oxide and indium-tin-oxide channel ferroelectric gate thin film transistors with yttrium doped hafnium-zirconium dioxide gate insulator prepared by chemical solution process

5. MFS and FGT using CSD Y-HZO

5.1. Motivation

As discussed in section 1.5, in the case of Si-based ferroelectric FETs, firstly, an interfacial SiO_2 layer is formed between Si channel and ferroelectric layer during the HfO_2 deposition and annealing process, which reduces the voltage applied to the ferroelectric layer and sometimes exhibits poor electrical properties. Secondly, the channel charge of Si-MOSFET does not match the ferroelectric polarization (charge mismatch problem). Most of the ferroelectric materials have spontaneous remnant polarization about 10-30 μC/cm^2, whereas the charge available for controlling the channel conductivity in case of MOSFET is generally less than 1 μC/cm^2. Therefore , Si-channel based FGT can only utilize minor loops of the ferroelectric gate insulator, which result in the reduction of the memory window (MW) (corresponding to threshold voltage shift in FGT)[1]. One way to solve the problem of charge mismatch in FGT is to utilize oxide semiconductor as a channel. Even thin conductive ITO film can be used as a channel in ferroelectric gate thin film transistor (hereafter called FGTs) [2] due to the large charge controllability of ferroelectric gate insulator and charge density induced is much larger than the conventional gate insulator such as SiO_2. If we consider a charge density of 10 μC cm^{-2} in HfO_2-based ferroelectric films, it relates to a sheet carrier density of channel, n_s, of 6.2×10^{13} cm^{-2}, which is substantial higher compared to that used in conventional Si-MOSFET. Therefore, Si channel based FGT can utilized minor loops of the ferroelectric gate insulator, results in reduction of the memory window (MW) (threshold voltage shift), because the MW is given by $2V_C$, where V_C means the coercive voltage of the polarization–voltage (P–V) loop used in the device operation. On the other hand, large MW can be obtained in case of FGTs based on ITO channel because full polarization or saturated P–V loop of the ferroelectric gate insulator can be utilized. This is one of the major benefits of FGT with an ITO oxide channel. Hence, it is interesting to realize ITO channel thin film transistor (TFT) with ferroelectric HZO since the ferroelectric material can induce large charge density due to the presence of remnant polarization and even conductive oxide can be used as a channel.

However, in contrast to the large number of reports in Si-based FGTs, there are only a few reports on oxide-channel FGT with HfO_2-based ferroelectric materials [3]–[5]. In these reports, two things are common, firstly HZO films were deposited by atomic layer deposition (ALD), and secondly, the oxide channel layer was deposited by sputtering. In this work, we prepared

both HZO gate insulator and oxide channel by chemical solution deposition (CSD). There is no report on HZO based oxide channel FGTs prepared by CSD.

As we discussed in chapter 3, P-E loops and leakage current of CSD Y-HZO films can be improved drastically by vacuum annealing process [6]. Moreover, oxygen annealed Y-HZO sample show trace of switching current. In chapter 4, we discussed Y-HZO with sputtered ITO shows robust ferroelectricity. At first, we first evaluate CSD Y-HZO films with 110 nm thick CSD ITO for FGT applications. Additionally, undoped HZO with 110 nm thick CSD ITO were fabricated [7]. Later, vacuum and oxygen annealed Y-HZO MFS structure with thin CSD In_2O_3 and ITO were fabricated for comparison. In this chapter, we will discuss about bottom gate FGTs using CSD Y-HZO (vacuum and oxygen annealed) as a gate insulator and CSD indium oxide (In_2O_3) or indium-tin-oxide (ITO) with thickness of 5-22 nm and 6-24 nm, respectively.

5.2. Experimental details

5.2.1. Fabrication of MFS with 110 nm thick CSD ITO as a top electrode (oxygen annealed)

The precursor/source solution was prepared as discussed in chapter 2. The precursor solution of Y-HZO were spin coated on platinized substrate with dimensions of 1.5 x 1.5 cm^2 as illustrated in Figure 5.1 (a) and then followed by drying wet film on a hot plate in the air at 225 ^oC for 3 min as depicted in Figure 5.1 (b). Y-HZO films were annealed in oxygen environment to perform crystallization step by using rapid thermal annealing (RTA) 800 ^oC for 3 min in the O_2 atmosphere as demonstrated in Figure 5.1(c). The thickness of the edge area of the film formed on the square-shape substrate by spin coating is usually thicker than that of the other part of the film. Therefore, Y-HZO films annealed in oxygen were patterned by using photolithography and the edge area was removed by using HF (chemical etching) to precisely evaluate the thickness of the Y-HZO films and to access bottom electrode Pt for measurement of the electrical property as shown in Figure 5.1 (d). The thickness of Y-HZO and undoped HZO was roughly 40 nm. In order, to fabricate MFS structures, the source solution of ITO was spin-coated on Y-HZO and undoped HZO as depicted in Figure 5.1 (e), followed by drying of wet ITO film on a hot plate at 100 ^oC for 3 min in the air. Finally, ITO film annealing was carried out in O_2 atmosphere at 600 ^oC for 15 min. Thickness of top ITO electrodes was 110

nm and an area of 4500 c.m^2 were patterned by using photolithography and chemical etching using Hydrochloric acid (HCL). Figure 1(f) shows final structure of sample after the deposition of the top electrode. Figure 1(g) shows Electrical measurement of Y-HZO films to measure P-E loops and C-V curves between top electrode ITO and bottom Pt electrode.

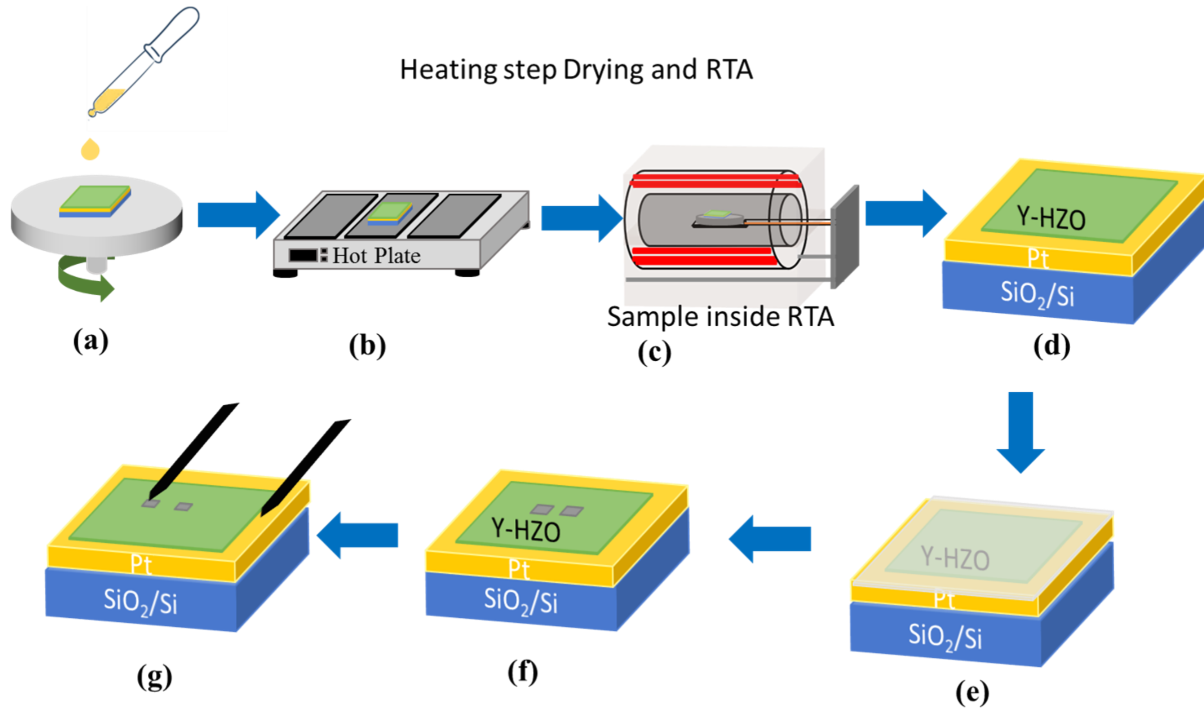

Figure 5.1 Schematic illustration of sample fabrication process; (a) spin coating of source solution, (b) drying on hot plate, (c) crystallization of films by using RTA, (d) patterning of films by photolithography followed by the etching, (e) deposition of top electrode, ITO or Pt, (f) patterning of top electrode, and (g) electrical measurements.

5.2.2. Fabrication of FGT

Figure 5.2 (a) shows the process flow for FGT fabrication. The precursor solution was spin-coated on a platinized substrate, followed by drying at 225 °C for 3 min in air. The crystallization was done by using RTA at 800 °C for 3 min in a vacuum and oxygen environment. Thickness of Y-HZO films was 33 nm. In_2O_3 and ITO source solution with various solution concentrations was prepared by mixing In (acac)$_3$ in PrA and In(acac)$_3$ and Sn(acac)$_2$ in PrA respectively at 120 °C for 1 hour. The thickness of In_2O_3 and ITO was controlled by changing precursor solution concentration as shown in Figure 5.2 (b). The thickness of In_2O_3 was 5, 12, 22, 39 and 57 nm for the source solution concentration of 0.025,

0.05. 0.10, 0.20 and 0.30 mol/kg, respectively, while the thickness of ITO was 6, 13, 24, 40 and 58 nm for 0.025, 0.05. 0.10, 0.20 and 0.30 mol/kg, respectively. As shown in Fig.5.2(b), the thickness of In_2O_3 and ITO are about the same and we use In_2O_3 and ITO layer whose thickness is less than 24 nm for FGT fabrication.

Precursor solution of In_2O_3 and ITO with a concentration of 0.025-0.10 mol/kg was spin-coated on Y-HZO films, followed by drying at 100 °C for 3 min in air, Then, the samples were annealed at 600 °C for 15 min in an O_2 environment. Pt source and drain electrodes were deposited by sputtering and patterned by the lift-off process. Next, the device region was isolated by wet etching. The channel length and width are 5 and 100 µm, respectively. Finally, the bottom gate electrode is accessed by photolithography and etching. The fabricated FGTs structure is shown in Figure 5.2 (d) and (e). Pt/ITO/Y-HZO/Pt capacitors were also fabricated to measure the ferroelectric properties of the MFS structures as shown in Figure 5.2 (c).

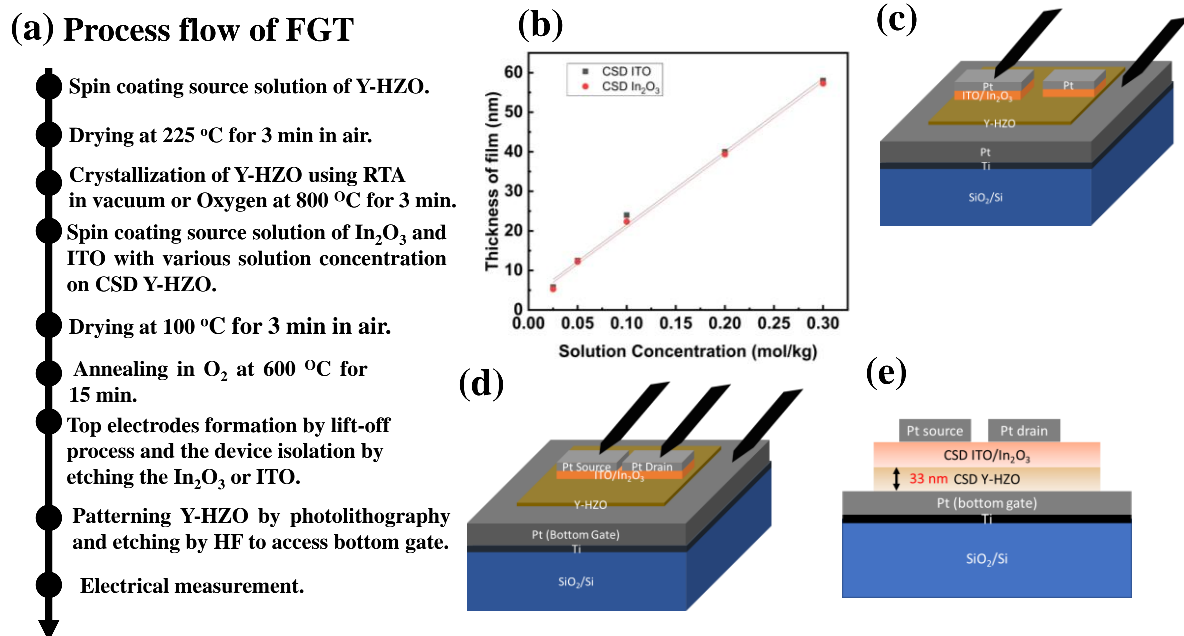

Figure 5.3 (a) Process flow of FGT (b) In_2O_3 and ITO film thickness as a function of source solution concentration, (c) schematic illustration of Pt/In_2O_3 or ITO/Y-HZO/Pt MFS structure (d) schematic illustration of FGT (e) schematic of FGT (cross section)

5.3. Ferroelectric properties of MFS structure

5.3.1. 110 nm thick CSD ITO (as metal electrode)

P-V and C-V measurements were measured for oxygen annealed Y-HZO and undoped films with CSD ITO as top electrode for MFS structure. Y-HZO films demonstrates ferroelectric behavior which was confirmed by P-V and C-V measurements as shown in Figure 5. 4 (a) and (b). P-V loops depicts ferroelectric behavior even though affected by leakage current. To evaluate the effect of doping, the P-V and C-V characteristics were also carried out for oxygen annealed undoped HZO film at 800 ^{o}C for 3 min. Figure 5.4(c) shows P-V loops of undoped HZO with sweeping voltage -12 to 12 V. P-V loops illustrate the presence of ferroelectricity and C-V curves shows clear butterfly shape was observed with decrease in capacitance on the positive side due to depletion of ITO top electrode as shown in Figure 5.4 (d), also observed in the case of Y-doped HZO. In comparison to Y-HZO films, P-E loops of HZO are slim and the ferroelectric nature is not so strong. Moreover, dielectric constant, namely slope of the P-E curve, of the undoped HZO film is smaller than that of the Y-HZO film. Therefore, CSD Y-HZO is promising for CSD oxide channel FGT.

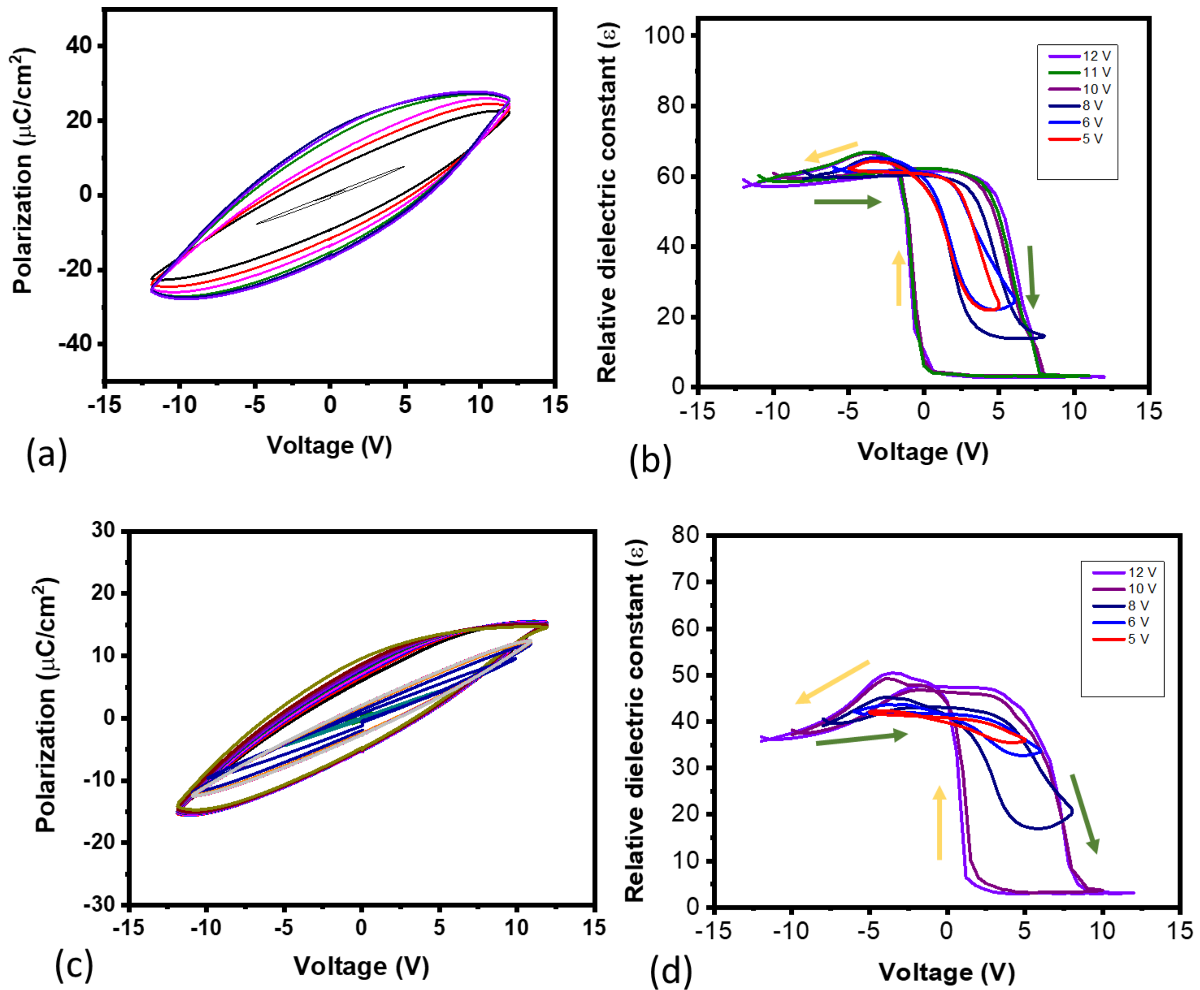

Figure 5.4 Electrical properties of Y-HZO and HZO with CSD ITO as top electrode for MFS structure; (a) P–V loops and (b) C-V of the MFS structure of Y-HZO, (c) P–V loops and (d) C-V of HZO,

5.3.2. 5-22 nm thick CSD In2O3 /Y-HZO (Vacuum annealed) MFS structure

In order to confirm the ferroelectricity of the Y-HZO films, the P-V and C-V characteristics were measured for the In_2O_3/Y-HZO MFS structures with various thicknesses of In_2O_3. Since the thin In_2O_3 layer may be depleted in the MFS structure, we use voltage instead of the electric field as a horizontal axis. Figures 5.5 (a), (c), and (e) shows P-V loops, and Figures 5.5 (b), (d), and (f) show the corresponding current response of Y-HZO films with an In_2O_3 thickness of 5, 12, and 22 nm respectively. As shown in Figures 5.5 (a) and 3(b), the P-V loops with 5-nm-thick In_2O_3 show clear ferroelectric hysteresis loops with corresponding switching current response. The P-V loops of the MFS structure with 12-nm-thick In_2O_3 also show clear

ferroelectric hysteresis loops with a slight increase in saturated polarization and switching current response. When the In_2O_3 thickness was 22 nm, as shown in Figures 5.5 (e), P-V loops become slightly rounded, which is probably due to an increase of leakage current as shown later in Figure 5.6. Figures 5.4 (e) shows corresponding switching current where switching current can be observed.

Figure 5.6 shows the leakage current density of the In_2O_3/Y-HZO MFS structures with 5 nm (dotted line) and 22 nm (solid line) thick In_2O_3. Leakage current at 1 MV/cm for the In_2O_3/Y-HZO MFS structure with 5-nm-(dotted line) and 22-nm-(solid line) thick In_2O_3 are 7.4 x 10^{-6} and 1.2 x 10^{-4} A/cm^2, respectively. The increase in leakage current when the thickness of In_2O_3 increased to 22 nm is consistent with the rounded P-V loops observed in Fig.5.5(e). In_2O_3/Y-HZO MFS structure with 12 nm In_2O_3 shows similar leakage current density of Y-HZO films with 5 nm thick In_2O_3 (not shown in the figure). In addition, remnant polarization (P_r) of Y-HZO films with different sweep voltage for different thicknesses of In_2O_3 is plotted in Figure 5.7. It was found that Y-HZO film with In_2O_3 thickness of 5 and 12 nm shows good saturation of P_r as observed in other HfO_2 based ferroelectric films [34]. In contrast, Y-HZO films with an In_2O_3 thickness of 22 nm shows no saturation of P_r, probably due to increase of the leakage current. Remnant polarization P_r and coercive field (E_c) of Y-HZO films with different thicknesses of In_2O_3 deduced from Figures 5.5 (a), (c) and (e), are approximately 8.7 μC/cm^2 and 1.3 MV/cm, 9.3 μC/cm^2 and 1.3 MV/cm, 14.3 μC/cm^2 and 2.1 MV/cm, respectively.

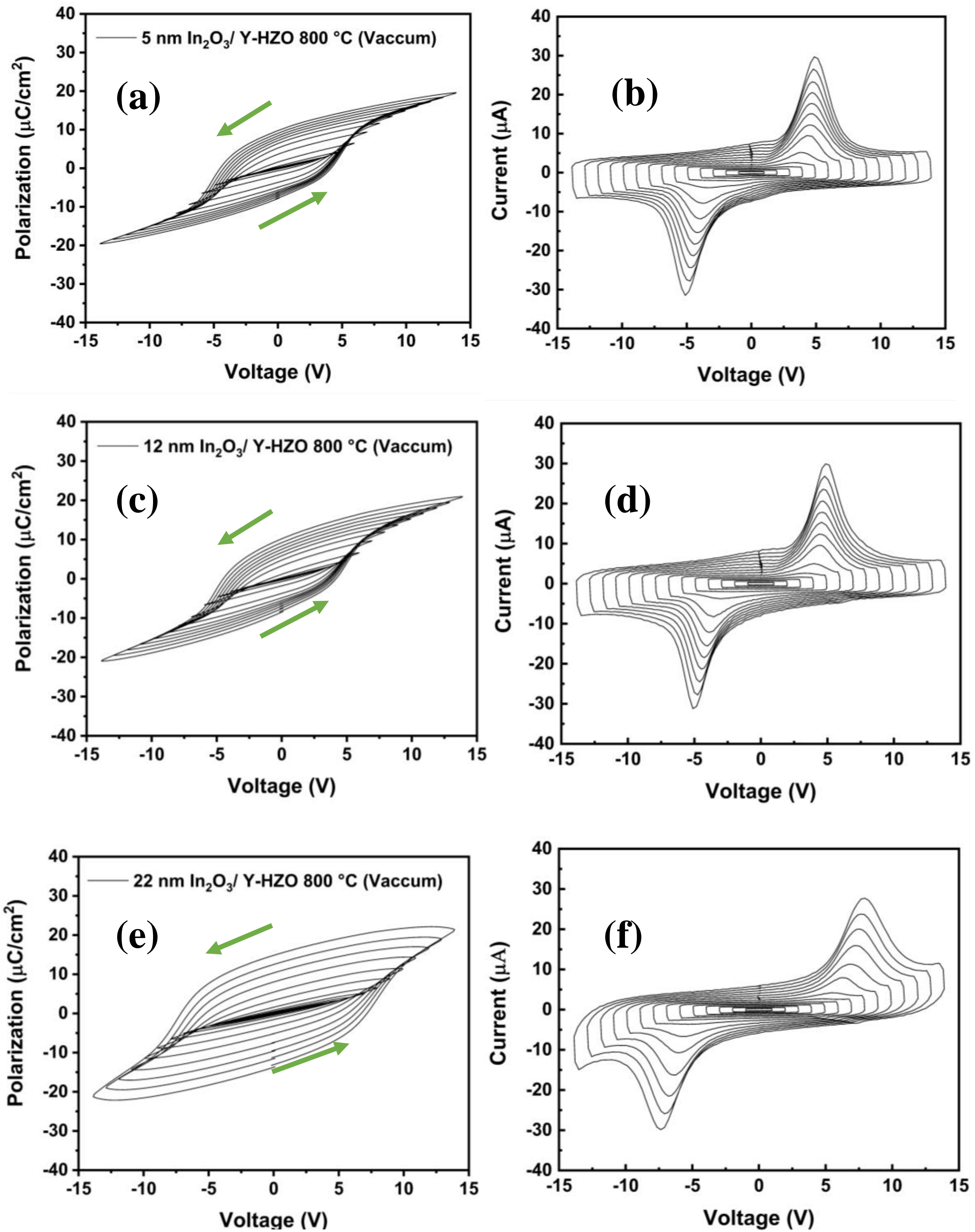

Fig. 5.5 Electrical properties of In_2O_3/Y-HZO MFS structures with different thickness of In_2O_3; (a) P–V loops and (b) current response of the MFS structure with 5-nm-thick CSD In_2O_3, (c) P–V loops and (d) current response with 12-nm-thick CSD In_2O_3, and (e) P–V loops and (f) current response with 22-nm-thick CSD In_2O_3.

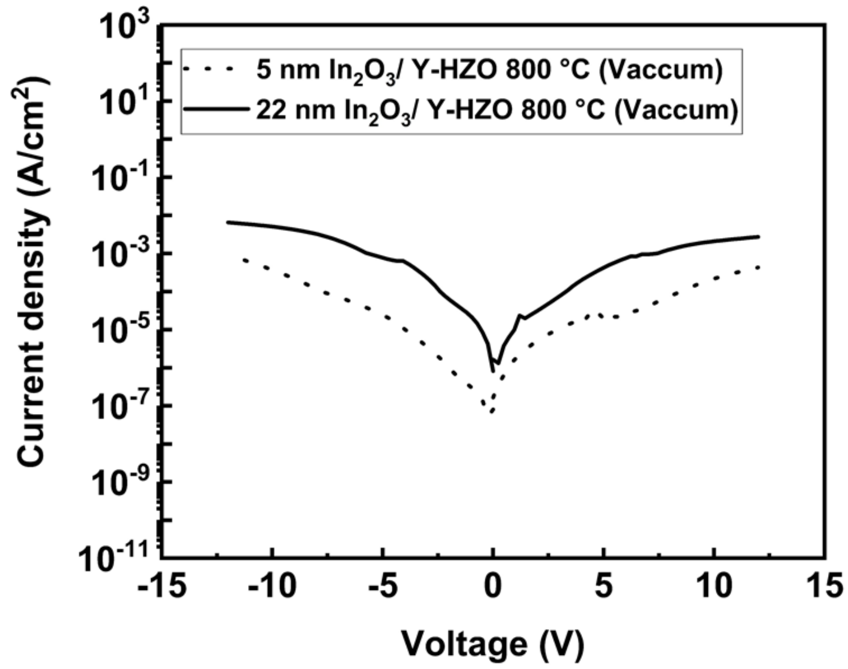

Fig. 5.6 Leakage current density as a function of voltage for the In_2O_3/Y-HZO MFS structures with In_2O_3 thickness of 5 nm (dotted line) and 22 nm (solid line).

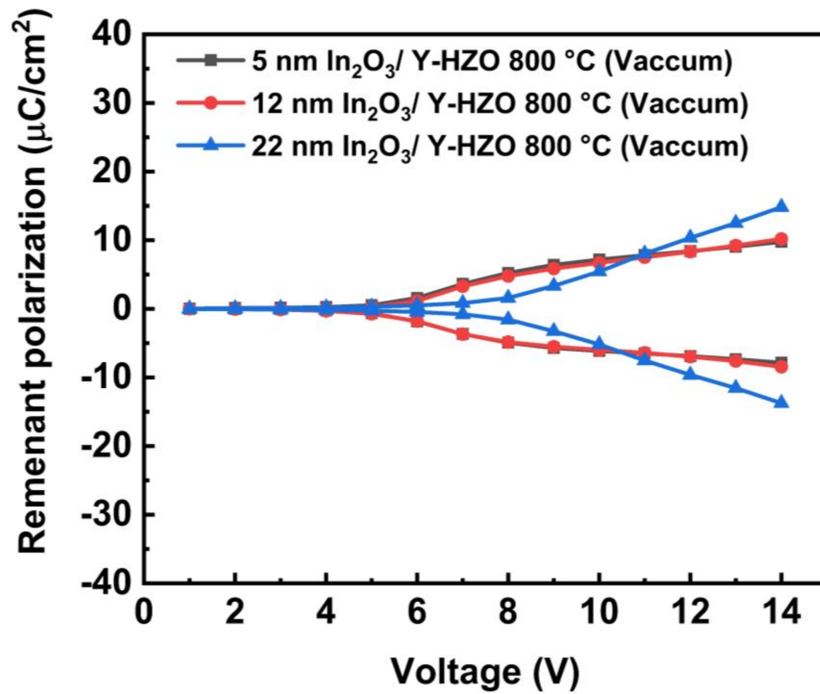

Fig. 5.7 Observed P_r value of the In_2O_3/Y-HZO MFS structures with different In_2O_3 thickness as a function of applied voltage.

In addition to P-V loops, C-V measurement was carried out to confirm the ferroelectric nature of Y-HZO with different thicknesses of In_2O_3. Figures 5.8(a), 5.8(b), and 5.8(c) shows C-V curves of the In_2O_3/Y-HZO MFS structures with an In_2O_3 thickness of 5, 12, and 22 nm, respectively. All samples show clear butterfly-shaped loops with a decrease in capacitance on the positive side, which demonstrates ferroelectric properties of Y-HZO films clearly. Since positive voltage is applied to top electrode, the observed decrease in capacitance value is due to the depletion of In_2O_3. A memory window (MW), width of the hysteresis loop in C–V curve which relates to the threshold voltage shift in the device, was estimated for a sweep voltage of ± 8 V from Figure 5.8 (a), 5.8 (b) and 5.8 (c), and these are approximately 1.9 V, 3.6 V and 3.9 V, respectively

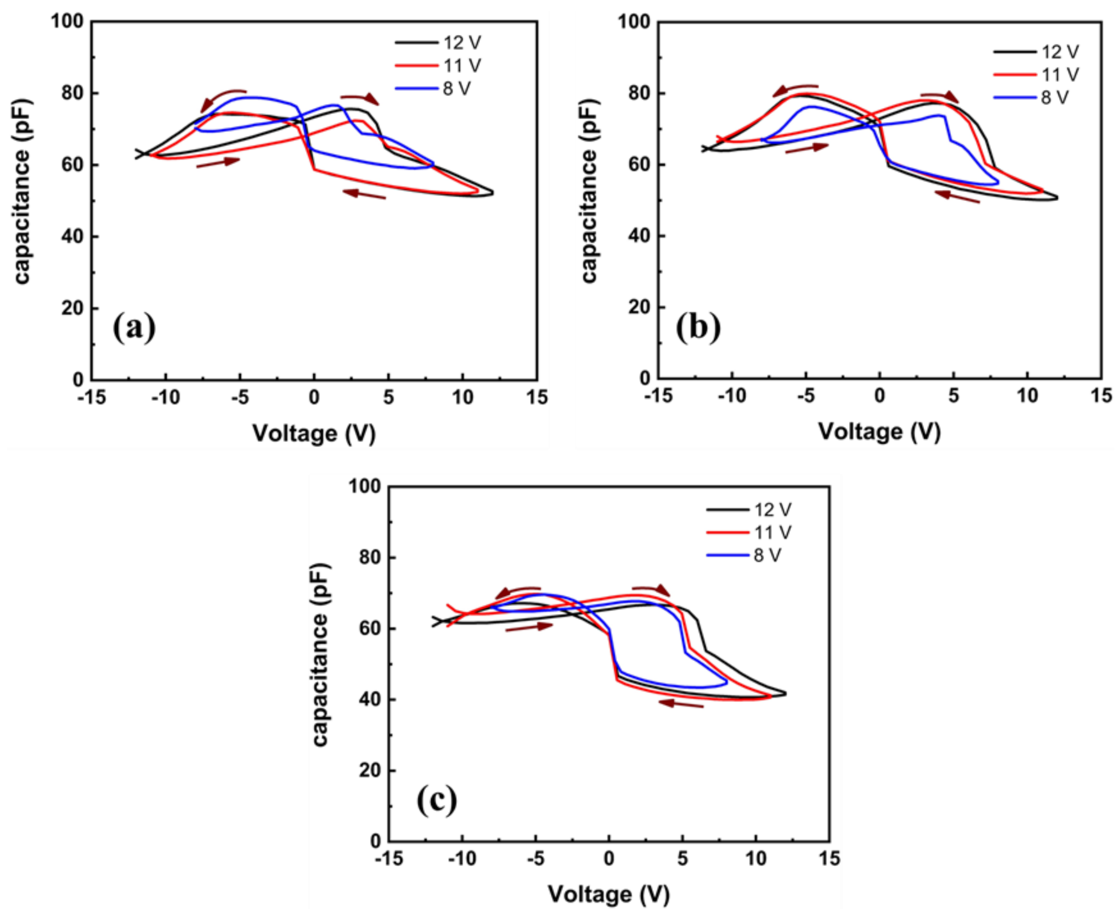

Fig. 5.8 Capacitance-voltage (C-V) curves of In_2O_3/Y-HZO MFS structures with different thickness of In_2O_3, (a) 5 nm (b) 12 nm and (c) 22 nm.

5.3.3. 6-24 nm thick CSD ITO /Y-HZO (Vacuum annealed) MFS structure

As discussed in the previous section, P-V and C-V measurement were performed to verify the ferroelectric nature of Y-HZO with In_2O_3, and the similar measurements were carried out for ITO/Y-HZO MFS structures with different thickness of ITO. Figures 5.9(a), 5.9(c), and 5.9(e) show P-V loops, and Figures 5.9(b), 5.9(d), and 5.9(f) show P-V corresponding current response of ITO/Y-HZO MFS structures with 6, 13, and 24 nm thick ITO, respectively. P-V loops of ITO/Y-HZO MFS structure with 6-nm-thick ITO shows clear hysteresis loops and I-V loops show clear switching response as shown in Figures 5.9(a) and 5.9(b), respectively. Likewise, P-V and I-V loops of ITO/Y-HZO MFS structures with 13-nm-thick ITO show clear ferroelectric hysteresis loop and clear switching response as depicted in Figures 5.9(c) and 5.9(d). When the thickness of the ITO layer was increased to 24 nm, P-V loops of ITO/Y-HZO MFS structure become slightly rounded due to an increase in leakage current, while the clear switching response still can be observed as shown in Figure 5.9(f). This is similar to the trend observed for the In_2O_3/Y-HZO MFS structures.

Figure 5.10 shows the leakage current density of-ITO/Y-HZO MFS structure with 6-nm-(dotted lines) and 24-nm-(solid line) thick ITO layer. The leakage current at 1 MV/cm for Y-HZO films with 6-nm and 24-nm-thick ITO layer deduced from Figure 5.10 are 1.34×10^{-6} and 1.2×10^{-5} A/cm^2, respectively, which suggests that leakage current was increased when the thickness of the ITO layer is 24 nm. ITO/Y-HZO MFS structure with 13 nm ITO shows similar leakage current density of ITO/Y-HZO MFS structure with 6 nm thick ITO. Hu et al., reported diffusion of In into HfO_2 film from InAs substrate [8]. Similar tendency for the MFS structure with thicker ITO or In_2O_3 could be possible which would cause the increase of leakage current, but further investigation is required to clarify the reason for the increase of leakage current for the MFS structure with relatively thick In_2O_3 or ITO layer. In addition, remnant polarization (Pr) of Y-HZO films as a function of sweep voltage for the ITO/Y-HZO MFS structures with different thicknesses of the ITO layer is shown in Figure 5.11. It was found that MFS structures with 6 and 13-nm-thick ITO show good saturation of P_r. On the other hand, the saturation of the P_r is not good for the MFS structures with 24-nm-thick ITO layer due to an increase of leakage current. P_r and Ec value estimated from Figs. 5.9(a), 5.9(c), 5.9(e) were approximately 9 μC/cm^2 and 1.3 MV/cm, 10 μC/cm^2 and 1.3 MV/cm, 18.5 μC/cm^2 and 1.9 MV/cm for Y-HZO films with 6, 13 and 24 nm thick ITO layer respectively.

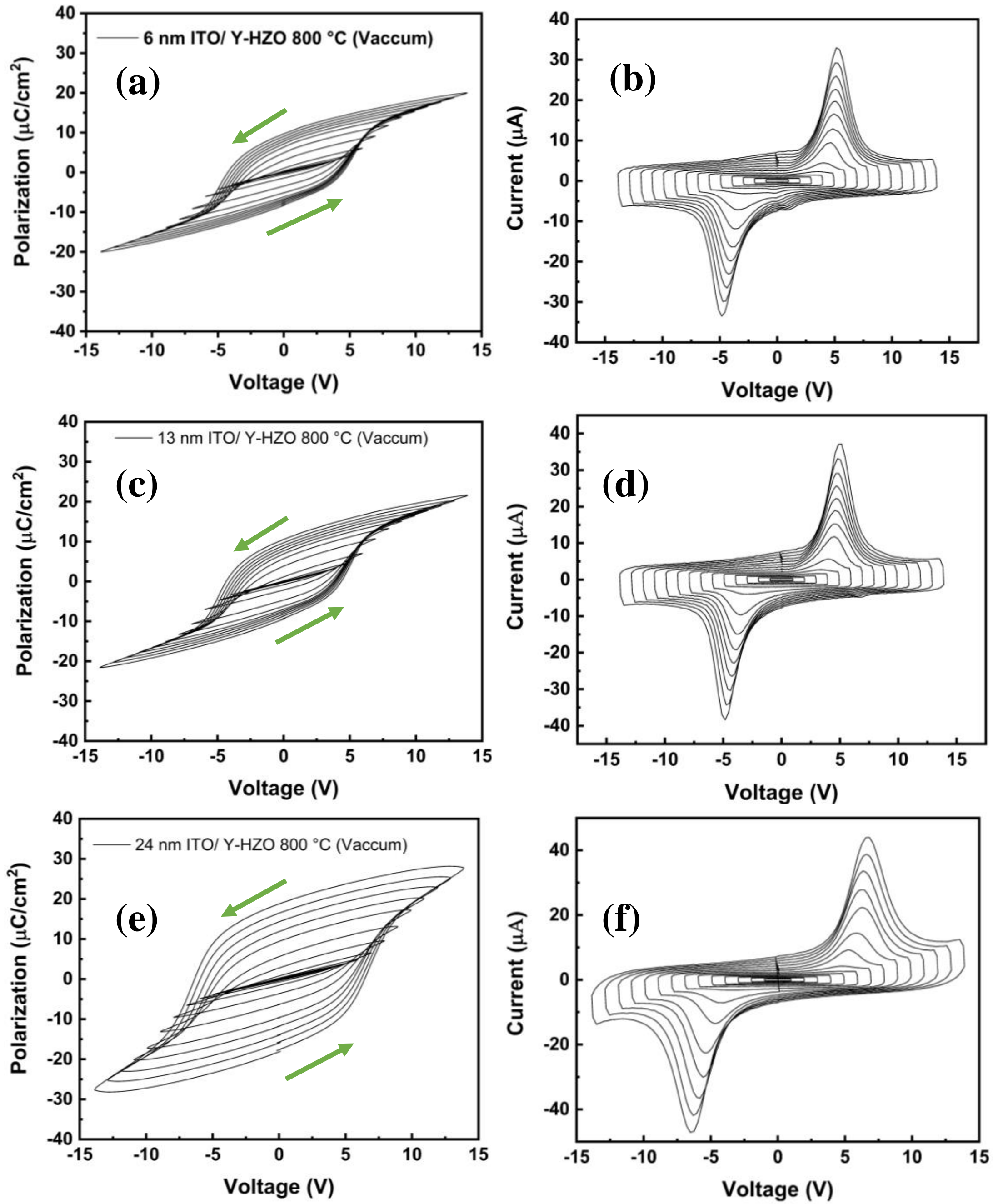

Fig. 5.9 Electrical properties of ITO Y-HZO MFS structures with different thickness of ITO; (a) P–V loops and (b) current response of the MFS structure with 6-nm-thick CSD ITO, (c) P–V loops and (d) current response with 13-nm-thick ITO, and (e) P–V loops and (f) current response with 24-nm-thick ITO.

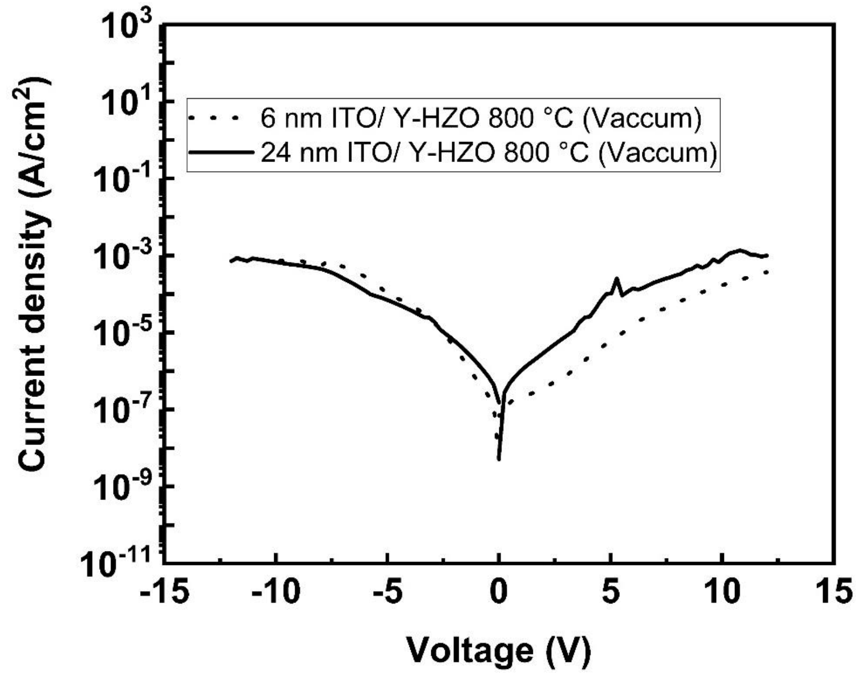

Fig. 5.10 Leakage current density as a function of voltage for the ITO/Y-HZO MFS structures with ITO thickness of 6 nm (dotted line) and 24 nm (solid line).

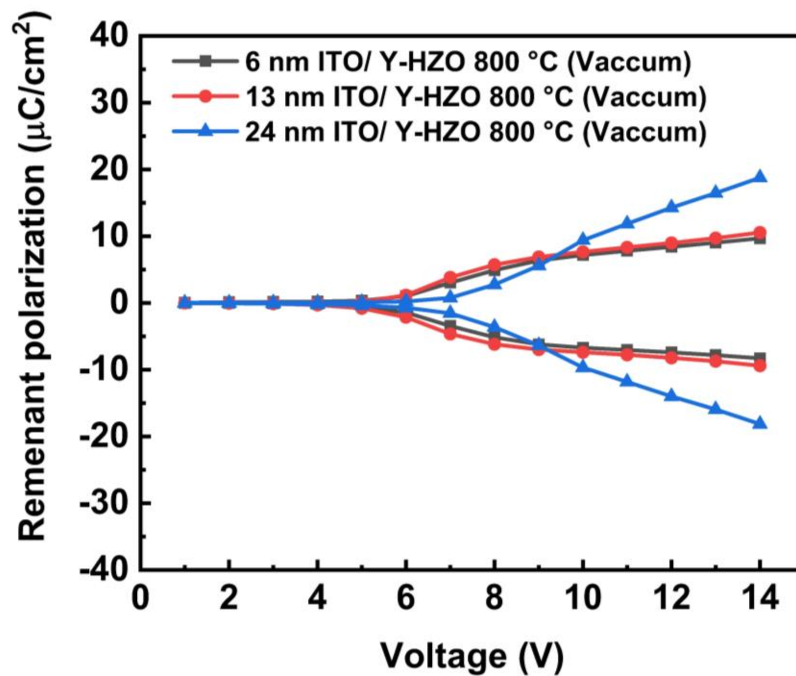

Fig. 5.11 Observed P_r value of the ITO/Y-HZO MFS structures with different ITO thickness as a function of applied voltage.

In addition to P-V loops, we evaluated C-V characteristics for ITO/Y-HZO MFS structures, too. Figures 5.12(a), 5.12(b), and 5.12(c) show C-V curves of Y-HZO films with a thickness of ITO 6, 13, and 24 nm respectively. All samples depict clear butterfly-shaped loops with a decrease in capacitance on the positive side. The observed decrease in capacitance value is due

to the depletion of ITO. The MW of Y-HZO films with 6, 13, and 24-nm-thick ITO layer estimated for a sweep voltage of ± 8 V in Figure 5.9 (a), 5.9(b), and 5.9(c), are approximately 2.2 V, 3.7 V, and 4.7 V respectively.

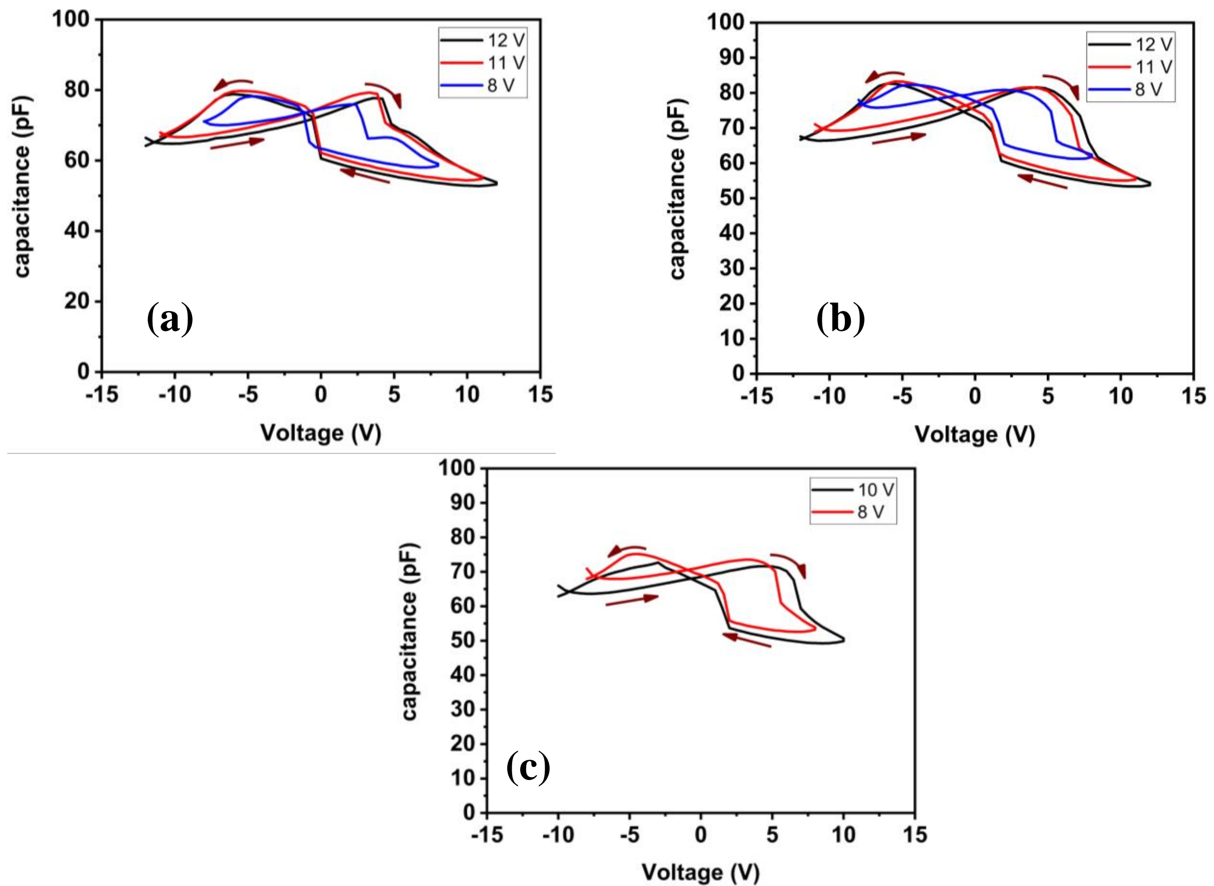

Fig. 5.12 Capacitance-voltage (C-V) curves of Y-HZO with different thicknesses of ITO (a) 6 nm (b) 13 nm (c) 24 nm.

5.3.4. 5-22 nm thick CSD In_2O_3 /Y-HZO (oxygen annealed) MFS structure.

In order to confirm the ferroelectricity of the Y-HZO films, the P-V and C-V characteristics were measured for the In_2O_3/Y-HZO (oxygen annealed) MFS structures with various thicknesses Figures 5.13 (a), (c), and (e) shows P-V loops, and Figures 5.13 (b), (d), and (f) show the corresponding current response of Y-HZO films with an In_2O_3 thickness of 5, 12, and 22 nm respectively. As shown in Figures 3(a) and 3(b), the P-V loops with 5-nm-thick In_2O_3 show small ferroelectric hysteresis loops with small trace of switching current response along with leakage current. The P-V loops of the MFS structure with 12-nm-thick In_2O_3 also show slightly better ferroelectric hysteresis loops with a slight increase in saturated polarization and switching current response as also observed in previous section. When the In_2O_3 thickness was 22 nm, as shown in Figure 3 (e), P-V loops become rounded, which is probably due to an increase of leakage current. P-V loops of vacuum annealed with 22 nm thick In_2O_3 were much superior as compared to oxygen annealed sample because oxygen annealed sample have leakage compared to vacuum annealed as discussed in chapter 3.

Figure 5.14 shows the leakage current density of the In_2O_3/Y-HZO MFS structures with 5 nm. Leakage current at 1 MV/cm for the In_2O_3/Y-HZO MFS structure with 5-nm-(dotted line) and 22-nm-(solid line) thick In_2O_3 are 6.3 x 10^{-5} which is higher than vacuum annealed. In addition, remnant polarization (P_r) of oxygen annealed Y-HZO films with different sweep voltage for different thicknesses of In_2O_3 is plotted in Figure 5.15. It was found that oxygen annealed Y-HZO film with different In_2O_3 thickness shows no saturation of P_r probably due to increase of the leakage current. In contrast, Vacuum Y-HZO films with an In_2O_3 thickness of 5 and 12 nm shows good saturation of P_r, Remnant polarization P_r and coercive field (E_c) of Y-HZO films with different thicknesses of In_2O_3 deduced from Figure 3 (a), (c) and (e), are approximately 2.5 μC/cm^2 and 1.2 MV/cm, 4.5 μC/cm^2 and 1.4 MV/cm, 6.84 μC/cm^2 and 1.9 MV/cm, respectively.

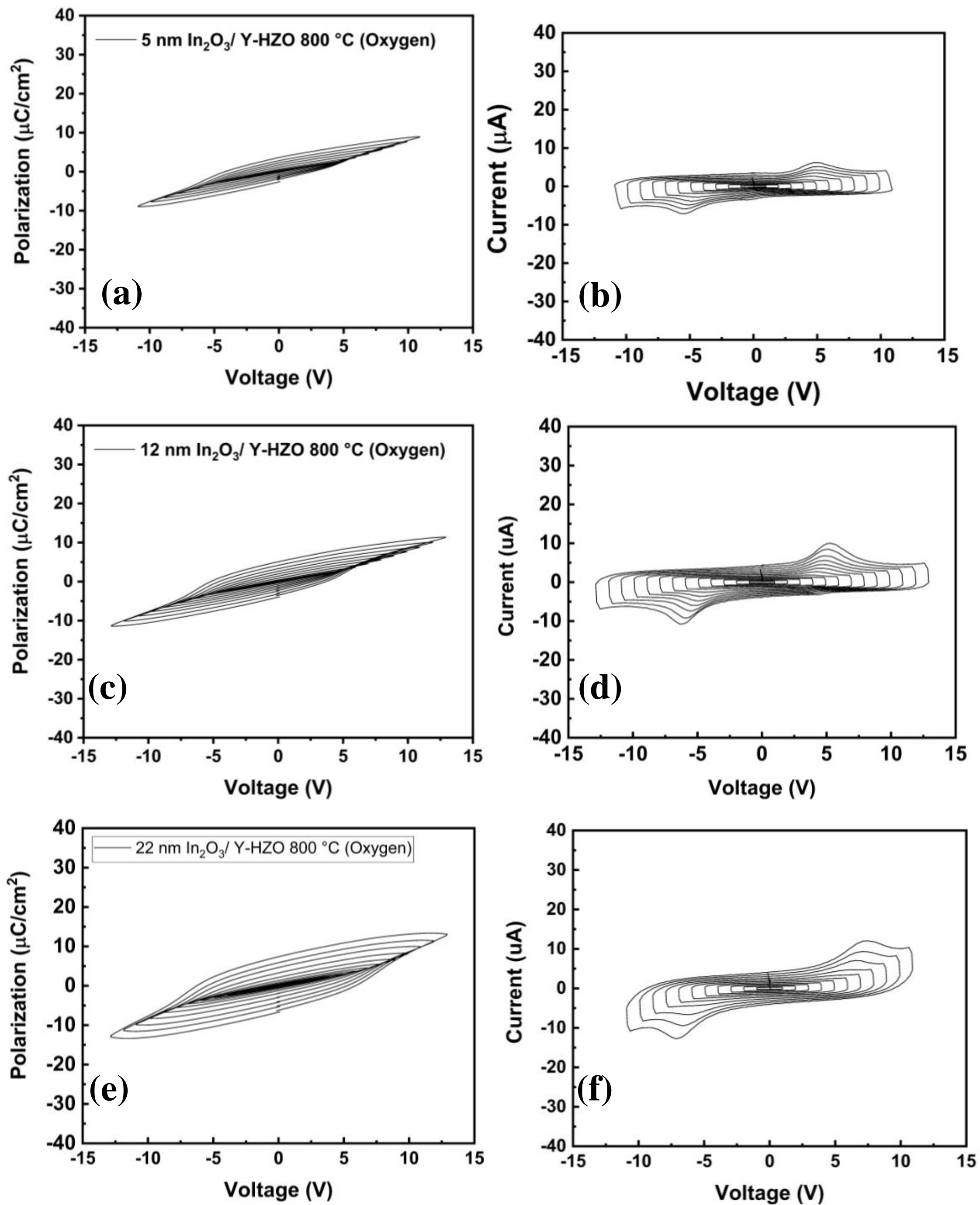

Fig. 5.13 Electrical properties of In_2O_3/Y-HZO MFS structures with different thickness of ITO; (a) P–V loops and (b) current response of the MFS structure with 5-nm-thick CSD In_2O_3, (c) P–V loops and (d) current response with 13-nm-thick In_2O_3, and (e) P–V loops and (f) current response with 24-nm-thick In_2O_3.

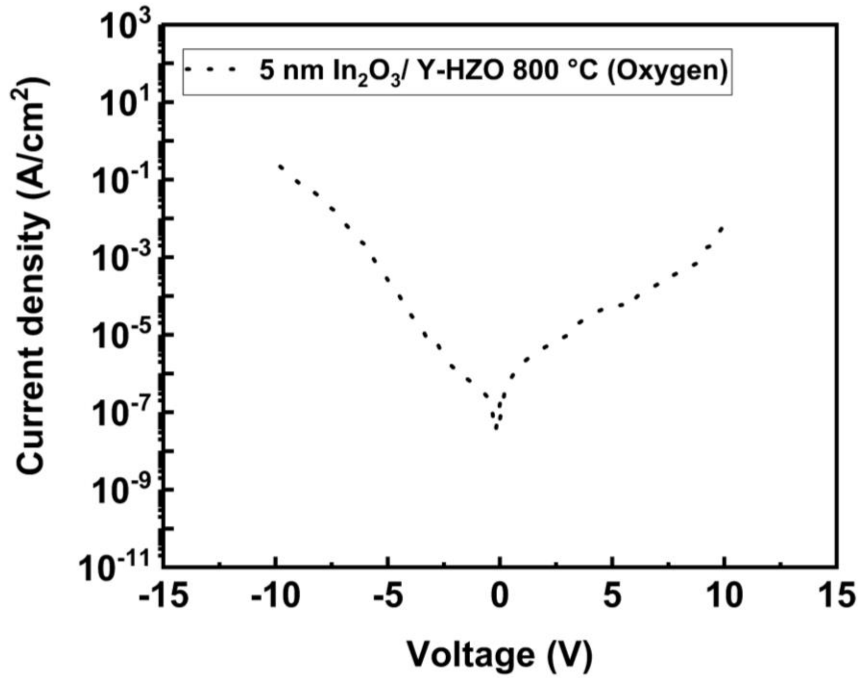

Fig. 5.14 Leakage current density as a function of voltage for the In_2O_3/Y-HZO MFS structures with In_2O_3 thickness of 5 nm.

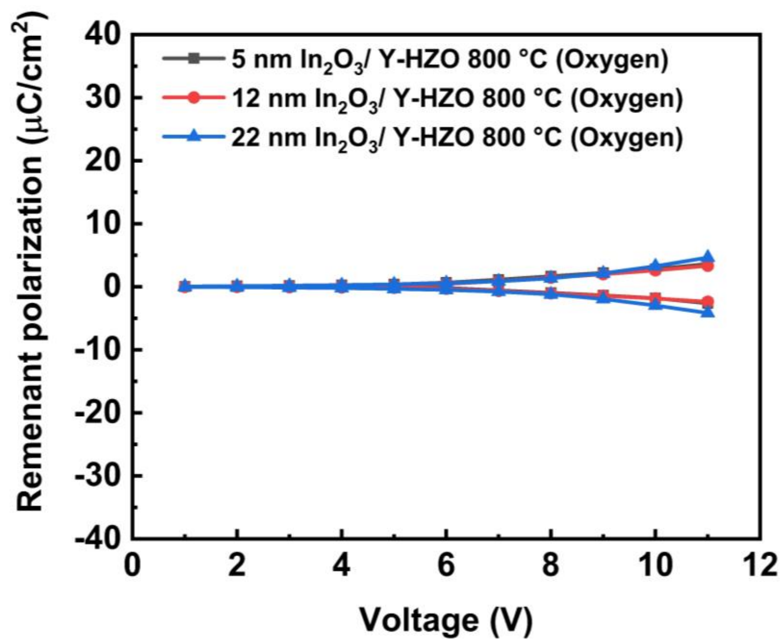

Fig. 5.15 Observed Pr value of the ITO/Y-HZO MFS structures with different ITO thickness as a function of applied voltage.

In addition to P-V loops, C-V measurement was carried out to confirm the ferroelectric nature of Oxygen annealed Y-HZO with different thicknesses of In_2O_3. Figures 5.16 (a), 5.16 (b), and 5.16 (c) shows C-V curves of the In2O3/Y-HZO MFS structures with an In2O3 thickness of 5,

12, and 22 nm, respectively. All samples show clear butterfly-shaped loops with a decrease in capacitance on the positive side, which demonstrates ferroelectric properties of Y-HZO films clearly. Since positive voltage is applied to top electrode, the observed decrease in capacitance value is due to the depletion of In_2O_3. A memory window (MW), width of the hysteresis loop in C–V curve which relates to the threshold voltage shift in the device, was estimated for a sweep voltage of ± 6 V from figure 6 (a), 6 (b) and 6 (c), and these are approximately 1.5 V, 2.9 V and 3.5 V, respectively . It is interesting to note that, the change is capacitance in vacuum anneal sample is larger than oxygen annealed samples which due to better ferroelectric properties, also observed for MFM structure in chapter 3.

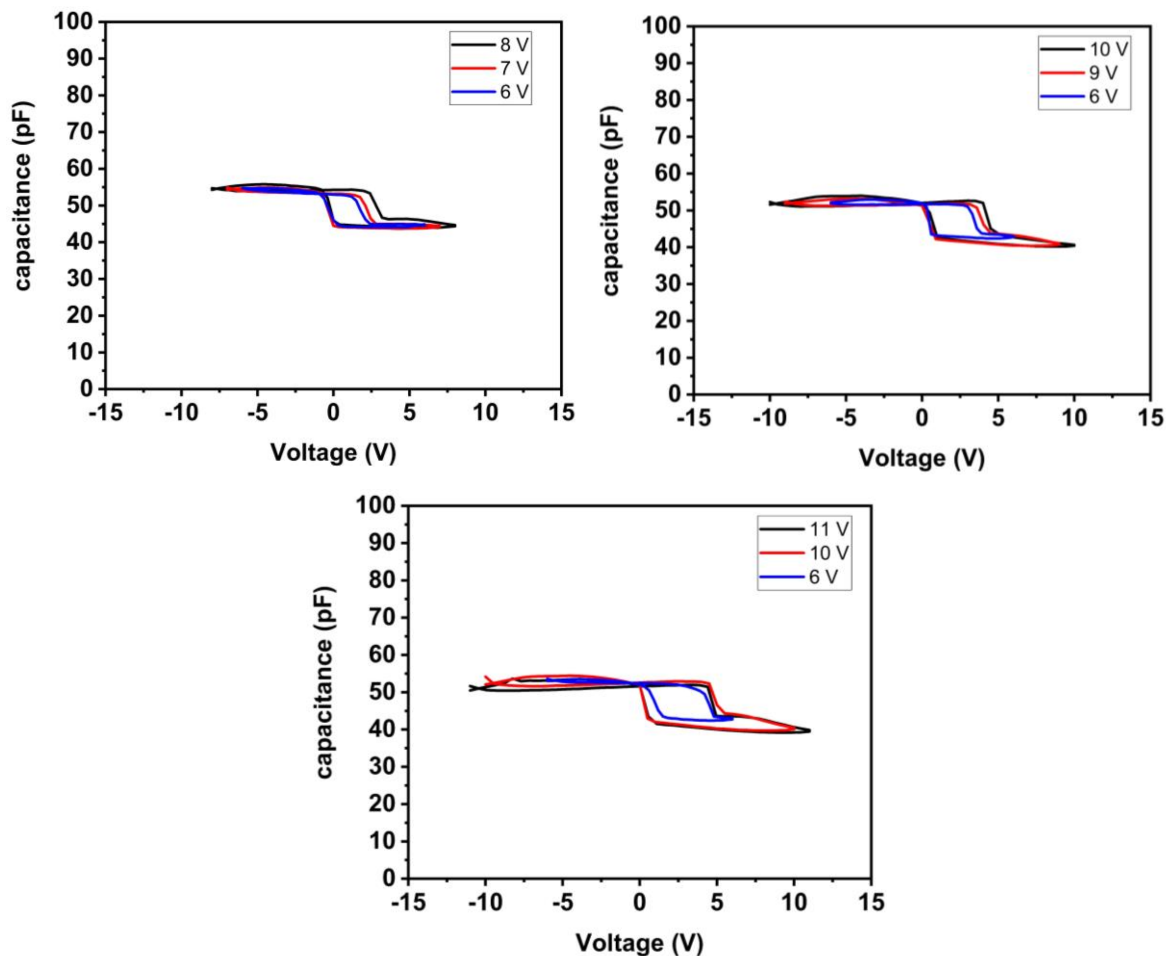

Fig. 5.16 Capacitance-voltage (C-V) curves of In_2O_3/Y-HZO MFS structures with different thickness of In_2O_3, (a) 5 nm (b) 12 nm and (c) 22 nm.

5.3.5. 6-24 nm thick CSD ITO /Y-HZO (oxygen annealed) MFS structure.

As discussed in the previous section, P-V and C-V measurement were performed to verify the ferroelectric nature of oxygen annealed Y-HZO with In_2O_3, and the similar measurements were carried out for ITO/Y-HZO (oxygen annealed) MFS structures with different thickness of ITO. Figures 5.17(a), 5.17(c), and 5.17(e) show P-V loops, and Figures 5.17 (b), 5.17(d), and 5.17(f) show P-V corresponding current response of ITO/Y-HZO MFS structures with 6, 13, and 24 nm thick ITO, respectively. P-V loops of ITO/Y-HZO MFS structure with 6-nm-thick ITO shows small hysteresis loops and I-V loops show small trace of switching response as shown in Figures 5.17 (a) and 5.17 (b), respectively. On the other hand, P-V and I-V loops of ITO/Y-HZO MFS structures with 13-nm-thick ITO shows slightly better ferroelectric hysteresis loop and slightly better switching response as depicted in Figures 5.17(c) and 5.17(d). When the thickness of the ITO layer was increased to 24 nm, P-V loops of ITO/Y-HZO MFS structure become rounded due to an increase in leakage current even though trace of switching response still can be observed as shown in Figure 7(f). Similar trend like this was also observed in previous section.

Figure 5.18 shows the leakage current density of-ITO/Y-HZO MFS structure with 6-nm ITO/ The leakage current at 1 MV/cm for Y-HZO films with 6-nm thick ITO was deduced from Figure 5.18 are 1.04 x 10^{-5} In addition, remnant polarization (Pr) of oxygen annealed Y-HZO films as a function of sweep voltage for the ITO/Y-HZO MFS structures with different thicknesses of the ITO layer is shown in Figure 5.19. It was found that the saturation of the P_r is not good for all samples with the MFS structures due to leakage current. P_r and Ec value estimated from Figs. 5.17(a), 5.17(c), 5.17(e) were approximately 4.73 μC/cm^2 and 1.3 MV/cm, 5.36 μC/cm^2 and 1.5 MV/cm, 7.7 μC/cm^2 and 1.8 MV/cm for Y-HZO films with 6, 13 and 24 nm thick ITO layer respectively.

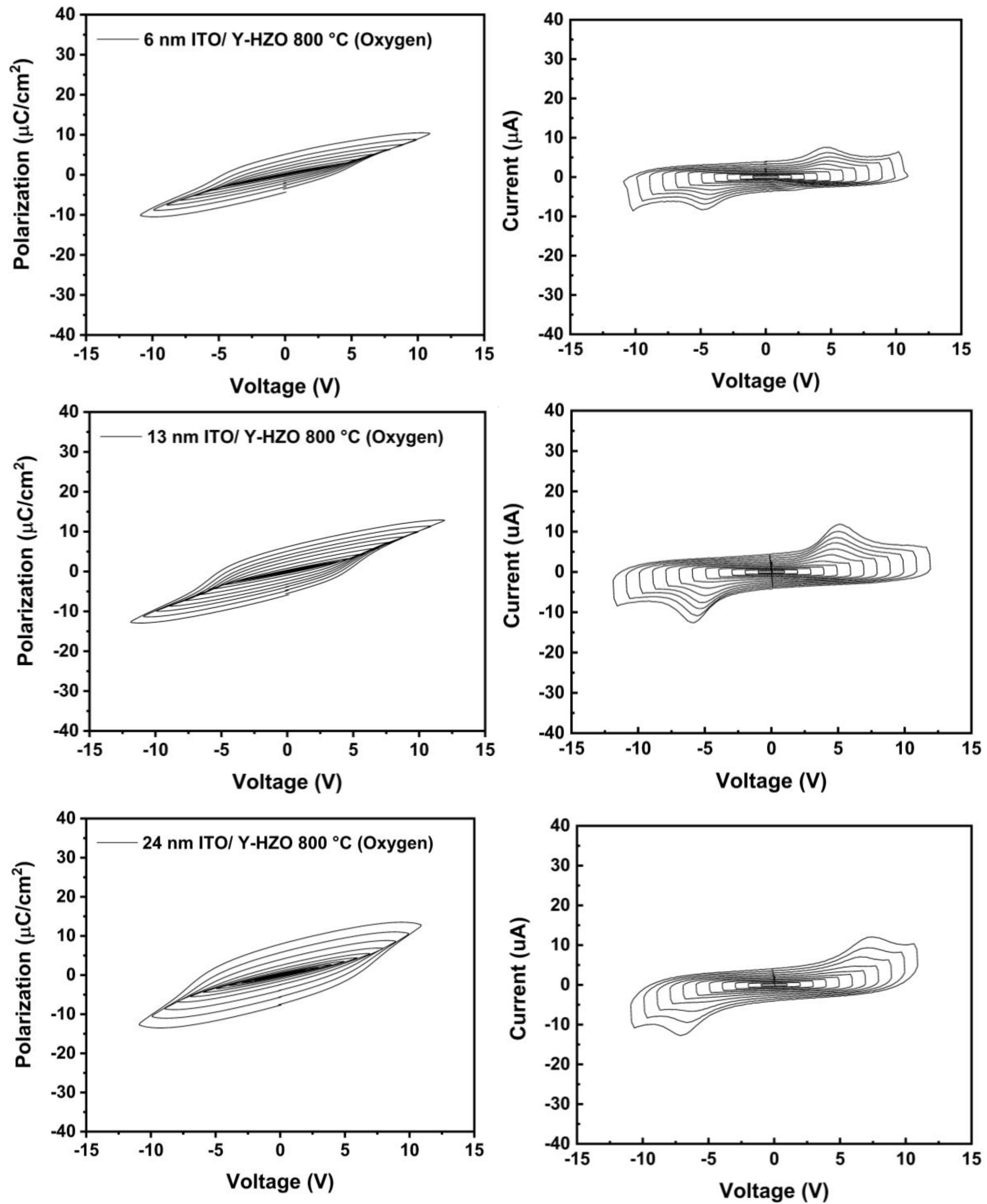

Fig. 5.17 Electrical properties of ITO/Y-HZO (oxygen) MFS structures with different thickness of ITO; (a) P–V loops and (b) current response of the MFS structure with 5-nm-thick CSD ITO, (c) P–V loops and (d) current response with 13-nm-thick ITO, and (e) P–V loops and (f) current response with 24-nm-thick ITO.

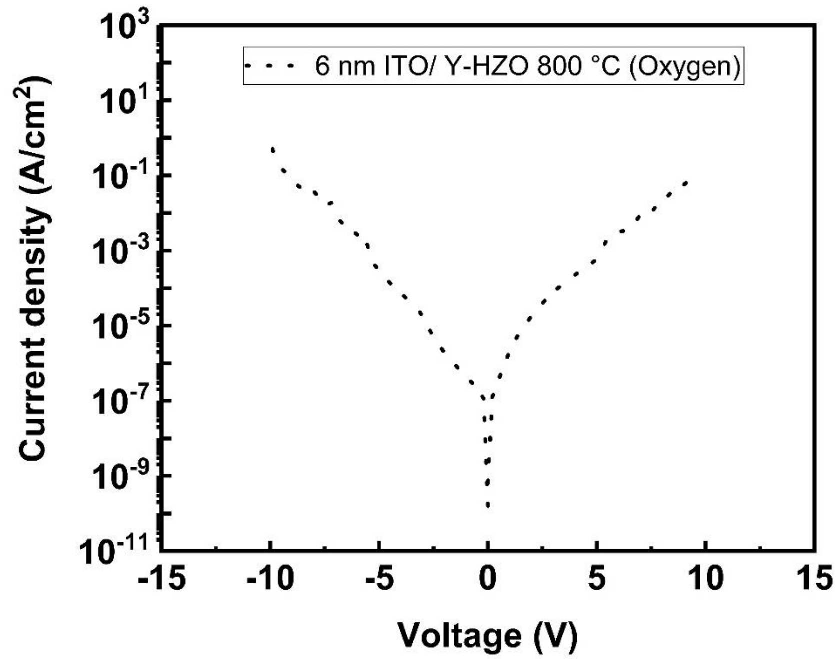

Fig. 5.18 Leakage current density as a function of voltage for the ITO/Y-HZO MFS structures with ITO thickness of 6 nm.

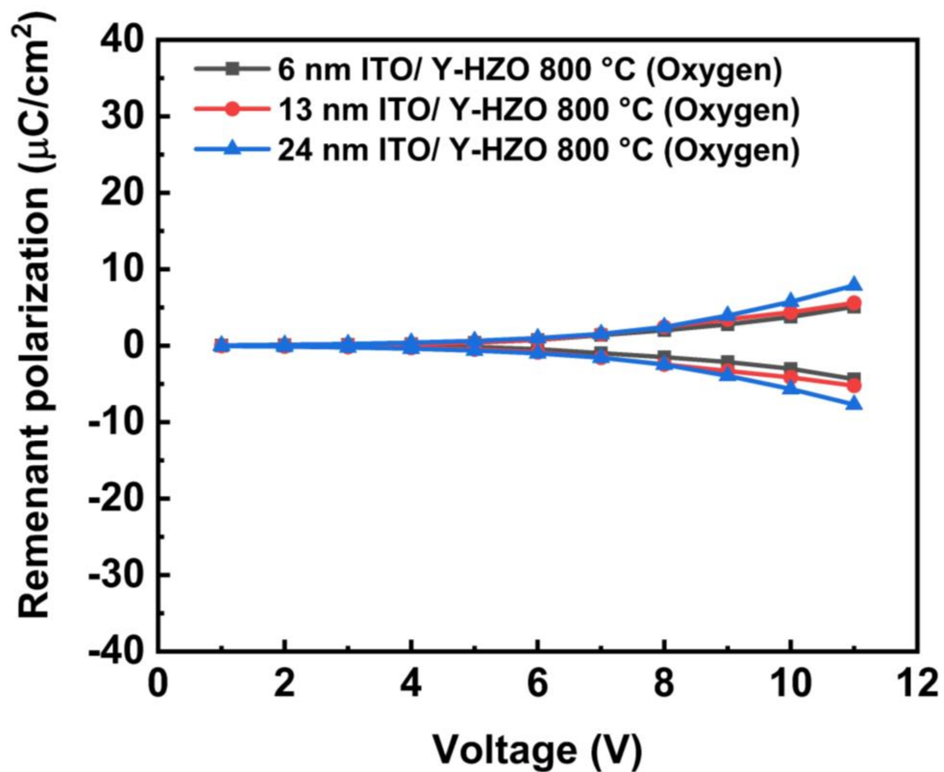

Fig. 5.19 Observed Pr value of the ITO/Y-HZO MFS structures with different ITO thickness as a function of applied voltage.

In addition to P-V loops, C-V measurement was carried out to confirm the ferroelectric nature of Oxygen annealed Y-HZO with different thicknesses of ITO. Figures 5.20 (a), 5.20 (b), and 5.20 (c) shows C-V curves of the ITO/Y-HZO MFS structures with an ITO thickness of 5, 12, and 22 nm, respectively. All samples show butterfly-shaped loops with a decrease in capacitance on the positive side, which demonstrates ferroelectric properties of Y-HZO films clearly. Since positive voltage is applied to top electrode, the observed decrease in capacitance value is due to the depletion of ITO. A memory window (MW), width of the hysteresis loop in C–V curve which relates to the threshold voltage shift in the device, was estimated for a sweep voltage of ± 6 V from Figure 5.20 (a), 5.20 (b) and 5.20 (c), and these are approximately 1.9 V, 2.3 V and 3.5 V, respectively. It is interesting to note that, the change is capacitance in vacuum anneal sample is larger than oxygen annealed samples which due to better ferroelectric properties, also observed for MFM structure in chapter 3.

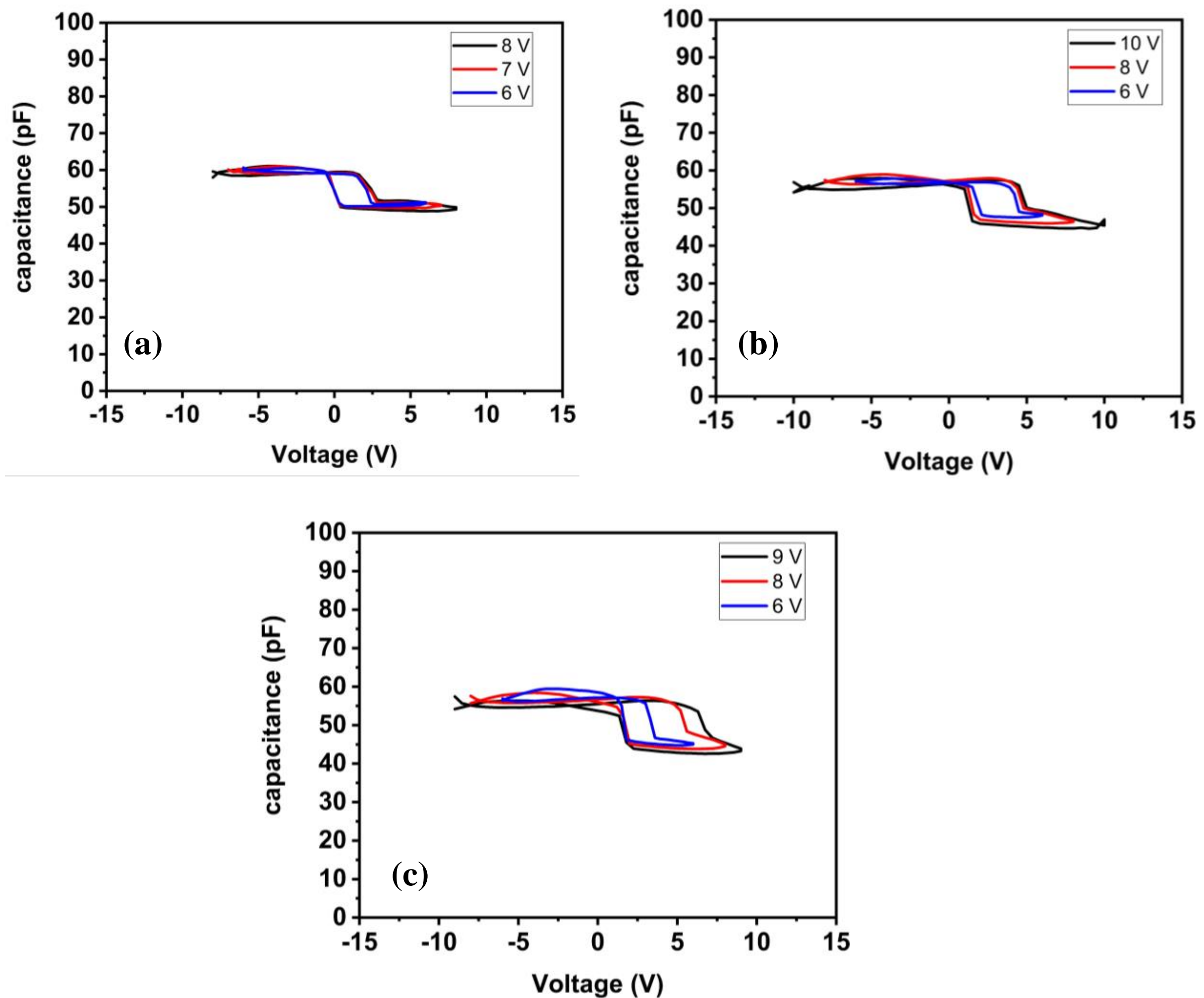

Fig. 5.20 Capacitance-voltage (C-V) curves of ITO/Y-HZO MFS structures with different thickness of ITO, (a) 5 nm (b) 12 nm and (c) 22 nm.

5.4. FGT

5.4.1. FGT with CSD In_2O_3 channel and vacuum annealed Y-HZO

Since we confirmed good ferroelectric properties of the Y-HZO films using the MFS structure, next we fabricated transistors. Figure 11 shows the electrical properties of FGT with a different channel thickness of In_2O_3 with output and transfer characteristics. Figures 5.21 (a), 5.21 (c), and 5.21 (e) shows I_D-V_D characteristics of FGT with In_2O_3 channel thickness of 5 nm, 12 nm, and 22 nm, respectively. I_D-V_D characteristics show typical n-channel field-effect transistor with linear behavior in the drain current at a low drain voltage, and at a high drain voltage, good saturation of the drain current for all samples. The channel length L and width W are 5 and 100 μm, respectively. A large saturated on current of approximately 8 mA (0.08 mA/μm) (at V_G 6V, 11 mA (0.11 mA/μm) at V_G 3V, and 11 mA (0.11 mA/ μm) at V_G 3V were obtained for channel thickness of 5, 12, and 22 nm, respectively. Figures 5.21 (b), 5.21 (d), and 5.21 (f) show I_D-V_G characteristics of FGT with In_2O_3 channel thickness of 5, 12, and 22 nm. I_D-V_G characteristics show a typical n-channel transfer curve for all samples with a counterclockwise hysteresis loop due to the ferroelectric nature of the Y-HZO gate insulator. FGT performance parameter such as on/off drain current ratio, subthreshold voltage swing (SS), and MW estimated from Figures 5.21 (b), 5.21 (d), and 5.21 (f), are approximately 7 x 10^6, 70 mV/dec and 0.66 V; 6.8 x 10^6, 172 mV/dec and 3.1 V; 1 x 10^6, 221 mV/dec and 3.4 V for channel thickness of 5, 12, and 22 nm, respectively. The SS increases with increasing channel thickness which is consistent with the previous report [3]. The SS value as low as 70 mV/dec and on/off ratio as high as 5.8 x 10^8 was obtained for channel thickness of 6 nm which is comparable to the best values reported so far [3], [5].The MW estimated from transfer characteristics shows good agreement with the MW estimated from C-V curves. However, in ideal case, the theoretical memory window is given by $2E_C \cdot d$ or $2V_C$, where d is thickness of the ferroelectric film, E_C is coercive field, and V_C is coercive voltage [9]. $2V_C$ values estimated from the P-V loop at ±8 V for Y-HZO films with different thicknesses of In_2O_3 shown in Figs. 5.5(a), 5.5(c), and 5.5(e), are approximately 5.2 V, 5.6 V and 7.1 V, respectively. The MW values from C-V curves and transfer characteristics are lower than $2V_C$, which might be due to the co-existence of charge injection which reduces the memory window especially for the device with 5-nm-thick In_2O_3 channel.

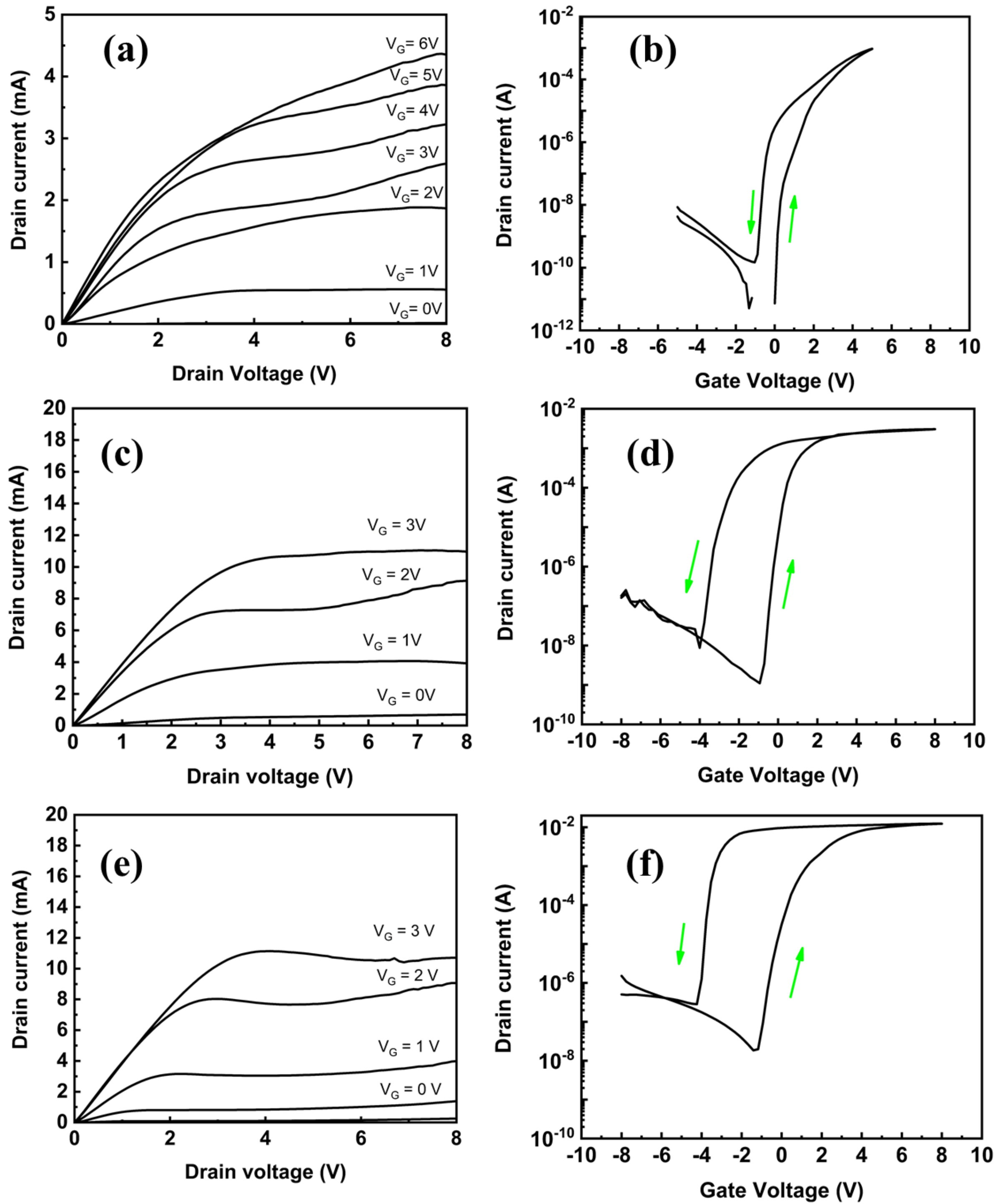

Fig. 5.21 Electrical properties of FGT with Y-HZO gate insulator (vacuum annealed) with different thickness of In_2O_3 channel, (a) I_D-V_D and, (b) I_D–V_G characteristics channel thickness of 5 nm, (c) I_D-V_D, and (d) I_D–V_G characteristics of the FGT with channel thickness 12 nm, (e) I_D-V_D, (f) I_D–V_G characteristics of the FGT with channel thickness 22 nm.

5.4.2. FGT with CSD ITO channel and vacuum annealed Y-HZO

Next, FGT with CSD ITO channel whose thickness is 6, 13, and 24 nm were also characterized. Figure 5.22 shows the output and transfer characteristics of FGTs with different channel thickness of ITO. Figures 5.22(a), 5.22(c) and 5.22(e) show I_D-V_D characteristics of FGT with In_2O_3 channel thickness of 6, 13 and 24 nm respectively. I_D-V_D characteristics clearly demonstrate standard n-channel MOSFET operation with good saturation of the drain current for all samples. Note that large saturated on drain current was obtained. The on current estimated from Figures 5.22(a), 5.22(c), and 5.22(e), are approximately 3 mA (0.03 mA/μm) at V_G 6V, 16 mA (0.16 mA/μm) at V_G 3V, and 18 mA (0.18 mA/ μm) at V_G 3V for the FGTs with channel thickness of 6, 13, and 24 nm, respectively. Figure 5.22 (b), 5.22 (d) and 5.22 (f) shows I_D-V_G characteristics of FGT with ITO channel thickness of 6, 13, and 24 nm respectively. I_D-V_G characteristics clearly exhibit a standard n-channel transfer curve with a counterclockwise hysteresis loop due to the ferroelectric nature of the Y-HZO. In the case of 6 nm thick ITO channel, the clockwise hysteresis was observed for the large gate voltage region, which is probably due to the charge injection which was also observed in 1 nm thick ITO channel FGTs reported previously [4]. On/off drain current ratio, SS, and MW estimated from Figures 5.22(b), 5.22(d), and 5.22(f), are approximately 5.8 x 10^6, 117 mV/dec and 1.1 V; 5.1 x 10^6, 198 mV/dec and 3.9 V; 1 x 10^6, 290 mV/dec and 4.5 V, for the FGTs with channel thickness of 6, 13, and 24 nm, respectively. The MW estimated from C-V curves shows good agreement with MW estimated from transfer characteristics. However, the MW values from transfer characteristics and CV curves are lower than $2V_C$ for the ITO channel devices, which is similar to the FGT with In_2O_3 channel. 2 V_C values estimated from the P-V loop at ±8 V of Figs. 5.9(a), 5.9(c), 5.9(e) are as large as 6 V, regardless of the ITO thickness. This indicate the charge injection co-exists and the charge injection effect is more serious when the ITO thickness is as thin as 6 nm. FGT with 6-nm-thick ITO channel shows low SS value but charge injection is dominant as result clockwise hysteresis as observed at higher voltage and the memory window decreases. When the channel thickness is increased to 24 nm, the off current and SS become large. Hence, the FGT with channel thickness around 13 nm shows comparatively good electrical properties with low SS value, high on/off drain current ratio and large MW.

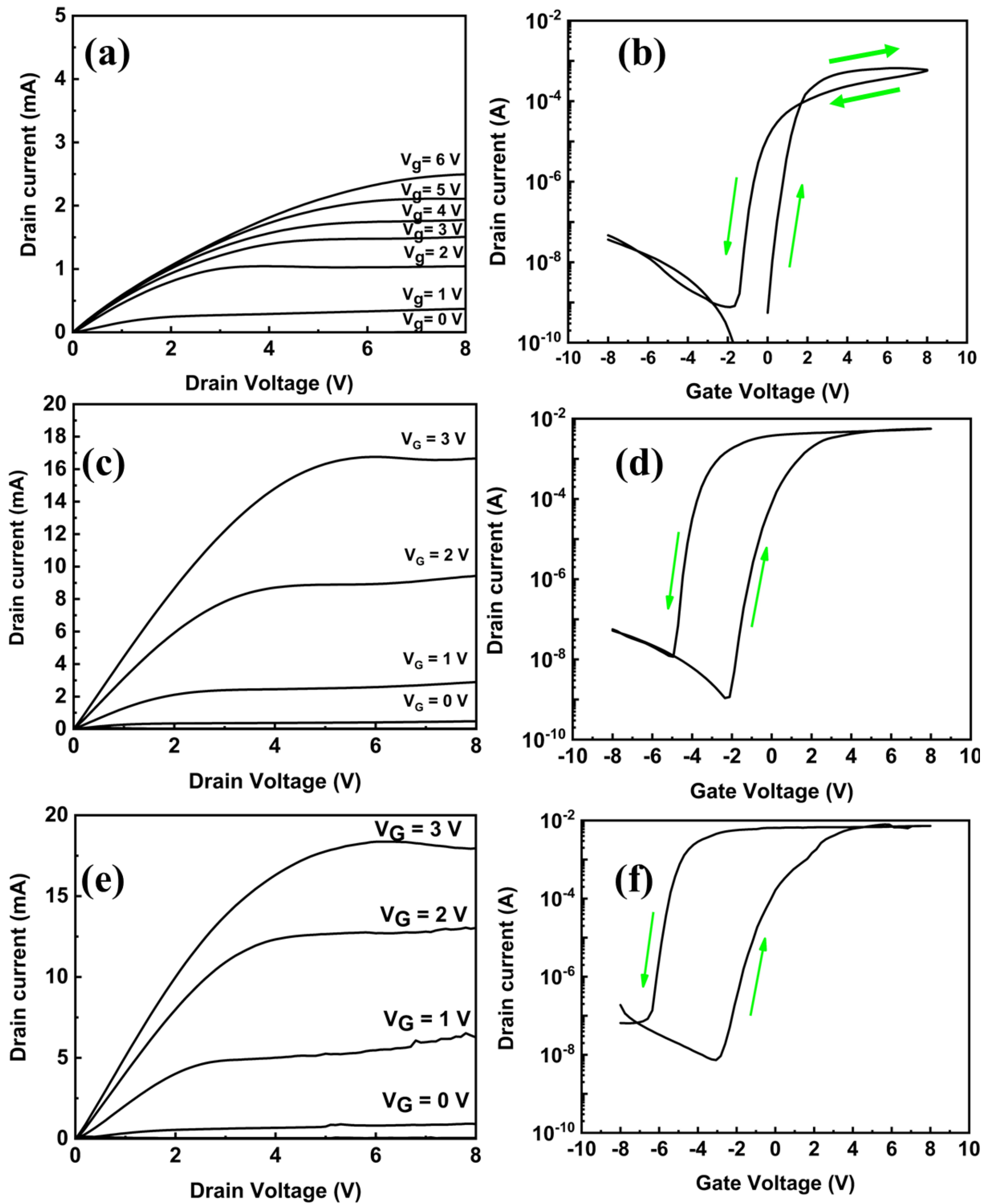

Fig. 5.22 Electrical properties of FGT with Y-HZO gate insulator (vacuum annealed) with different thickness of ITO channel, (a) I_D-V_D and (b) I_D–V_G characteristics of the FGT with channel thickness of 6 nm, (c) I_D-V_D and (d) I_D–V_G characteristics of the FGT with channel thickness 13 nm, (e) I_D-V_D and (f) I_D–V_G characteristics of the FGT with channel thickness 24 nm.

5.4.3. FGT with CSD In_2O_3 channel and oxygen annealed Y-HZO

Since we confirmed ferroelectric properties of the oxygen annealed Y-HZO films using the MFS structure, next we fabricated transistors. Figure 5.23 shows the electrical properties of FGT with a different channel thickness of In_2O_3 with output and transfer characteristics. Figures 5.23 (a), 5.23 (c), and 5.23 (e) shows I_D-V_D characteristics of FGT with In_2O_3 channel thickness of 5 nm, 12 nm, and 22 nm, respectively. I_D-V_D characteristics show typical n-channel field-effect transistor with linear behavior in the drain current at a low drain voltage, and at a high drain voltage, good saturation of the drain current for all samples. The channel length L and width W are 5 and 100 µm, respectively. A large saturated on current of approximately 1.72 mA (0.01 mA/µm) (at V_G 6V, 10 mA (0.10 mA/µm) at V_G 3V, and 13 mA (0.13 mA/ µm) at V_G 3V were obtained for channel thickness of 5, 12, and 22 nm, respectively. Figures 5.23 (b), 5.23 (d), and 5.23 (f) show I_D-V_G characteristics of FGT with In_2O_3 channel thickness of 5, 12, and 22 nm. I_D-V_G characteristics show a typical n-channel transfer curve for all samples with a counterclockwise hysteresis loop due to the ferroelectric nature of the Y-HZO gate insulator. FGT performance parameter such as on/off drain current ratio, subthreshold voltage swing (SS), and MW estimated from Figures 5.23 (b), 5.23 (d), and 5.23 (f), are approximately 1.1×10^6, 153 mV/dec and 0.83 V; 6.2×10^7, 310 mV/dec and 2,23 V; 2.08×10^5, 480 mV/dec and 2.5 V for channel thickness of 5, 12, and 22 nm, respectively. These results suggest that device performance degrade for oxygen annealed FGT as compared to vacuum annealed FGT.

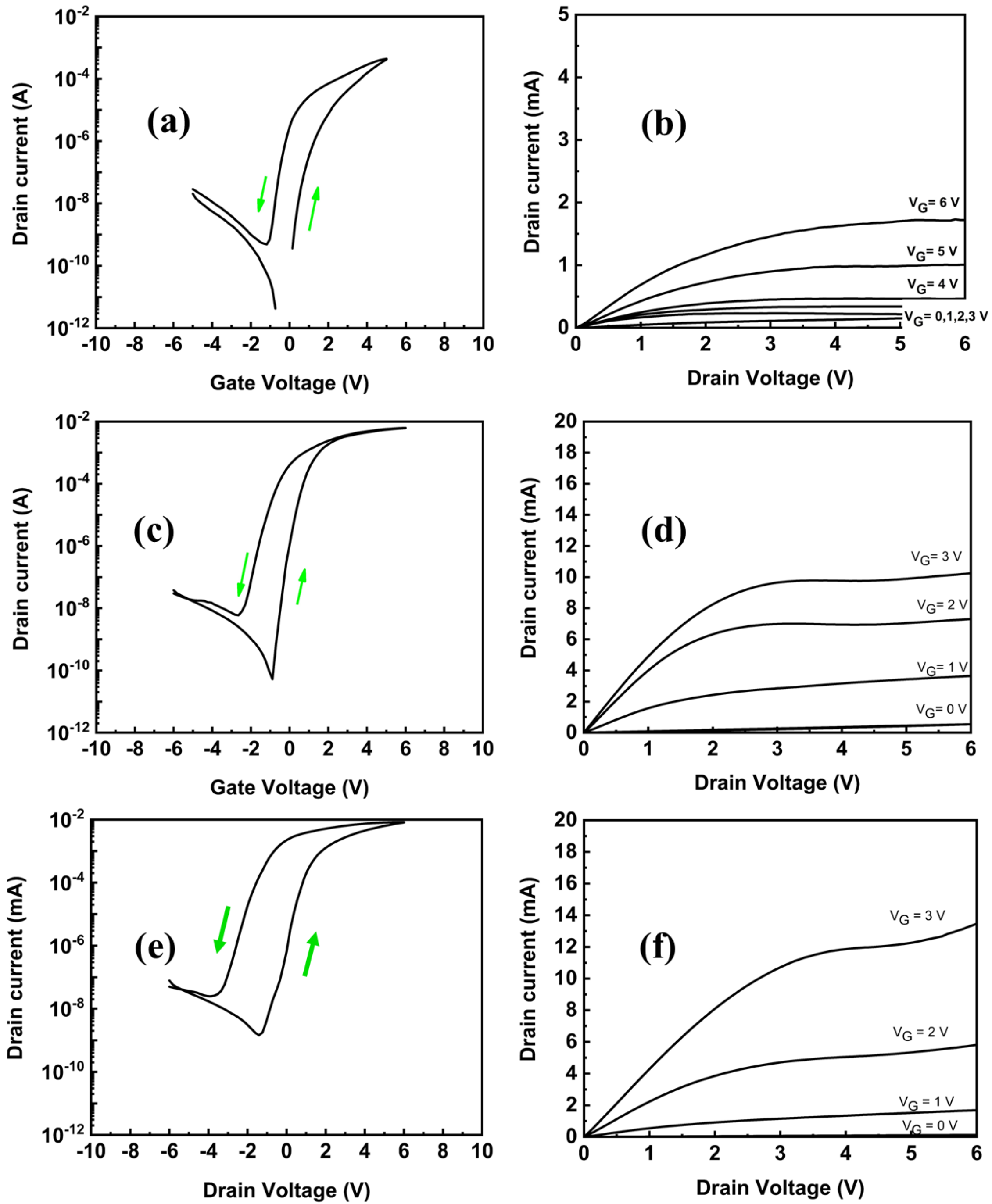

Fig. 5.23 Electrical properties of FGT with Y-HZO gate insulator (oxygen annealed) with different thickness of In_2O_3 channel, (a) I_D-V_D and, (b) I_D–V_G characteristics channel thickness of 5 nm, (c) I_D-V_D, and (d) I_D–V_G characteristics of the FGT with channel thickness 12 nm, (e) I_D-V_D, (f) I_D–V_G characteristics of the FGT with channel thickness 22 nm.

5.4.4. FGT with CSD ITO channel and oxygen annealed Y-HZO

Next, FGT with CSD ITO channel whose thickness is 6, 13, and 24 nm were also characterized. Figure 5.24 shows the output and transfer characteristics of FGTs with different channel thickness of ITO. Figures 5.24(a), 5.24(c) and 5.25(e) show I_D-V_D characteristics of FGT with In_2O_3 channel thickness of 6, 13 and 24 nm respectively. I_D-V_D characteristics clearly demonstrate standard n-channel MOSFET operation with good saturation of the drain current for all samples. Note that large saturated on drain current was obtained. The on current estimated from Figures 5.24(a), 5.24(c), and 5.24(e), are approximately 2.79 mA (0.02 mA/µm) at V_G 6V, 17 mA (0.17 mA/µm) at V_G 3V, and 17.5 mA (0.17 mA/ µm) at V_G 3V for the FGTs with channel thickness of 6, 13, and 24 nm, respectively. Figure 5.24 (b), 5.24 (d) and 5.24 (f) shows I_D-V_G characteristics of FGT with ITO channel thickness of 6, 13, and 24 nm respectively. I_D-V_G characteristics clearly exhibit a standard n-channel transfer curve with a counterclockwise hysteresis loop due to the ferroelectric nature of the Y-HZO. In the case of 6 nm thick ITO channel, the clockwise hysteresis was observed for the large gate voltage region, which is probably due to the charge injection which was also observed in 1 nm thick ITO channel FGTs reported previously [27]. On/off drain current ratio, SS, and MW estimated from Figures 5.24(b), 5.24(d), and 5.24(f), are approximately 1 x 10^5, 257 mV/dec and 1.14 V;1.06 x 10^6, 291 mV/dec and 1.59 V; 3.78 x 10^5, 336 mV/dec and 1.98 V, for the FGTs with channel thickness of 6, 13, and 24 nm, respectively. These results suggest that device performance degrade for oxygen annealed FGT as compared to vacuum annealed FGT. The interesting point about oxygen annealed FGT, most of device have high leakage current but when measurement is carried out several times, leakage current drastically reduced as shown in Figure 5.25. On contrary, Vacuum annealed FGT samples, most of devices were good. Overall, Vacuum annealed FGT shows good device performance compared to oxygen annealed samples due to better ferroelectric properties and lower leakage current.

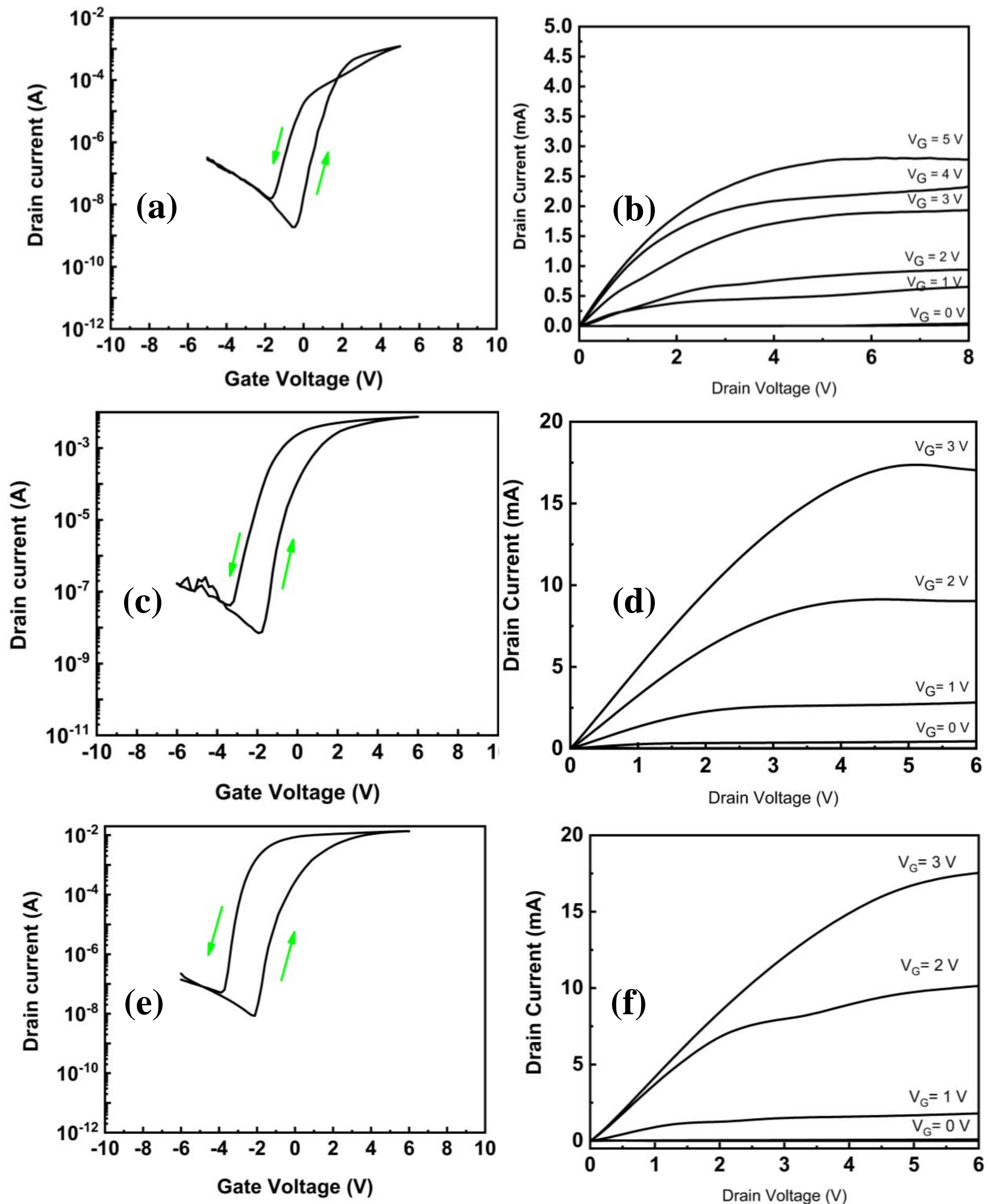

Fig. 5.24 Electrical properties of FGT with Y-HZO gate insulator (oxygen annealed) with different thickness of ITO channel, (a) I_D-V_D and, (b) I_D–V_G characteristics channel thickness of 5 nm, (c) I_D-V_D, and (d) I_D–V_G characteristics of the FGT with channel thickness 12 nm, (e) I_D-V_D, (f) I_D–V_G characteristics of the FGT with channel thickness 22 nm.

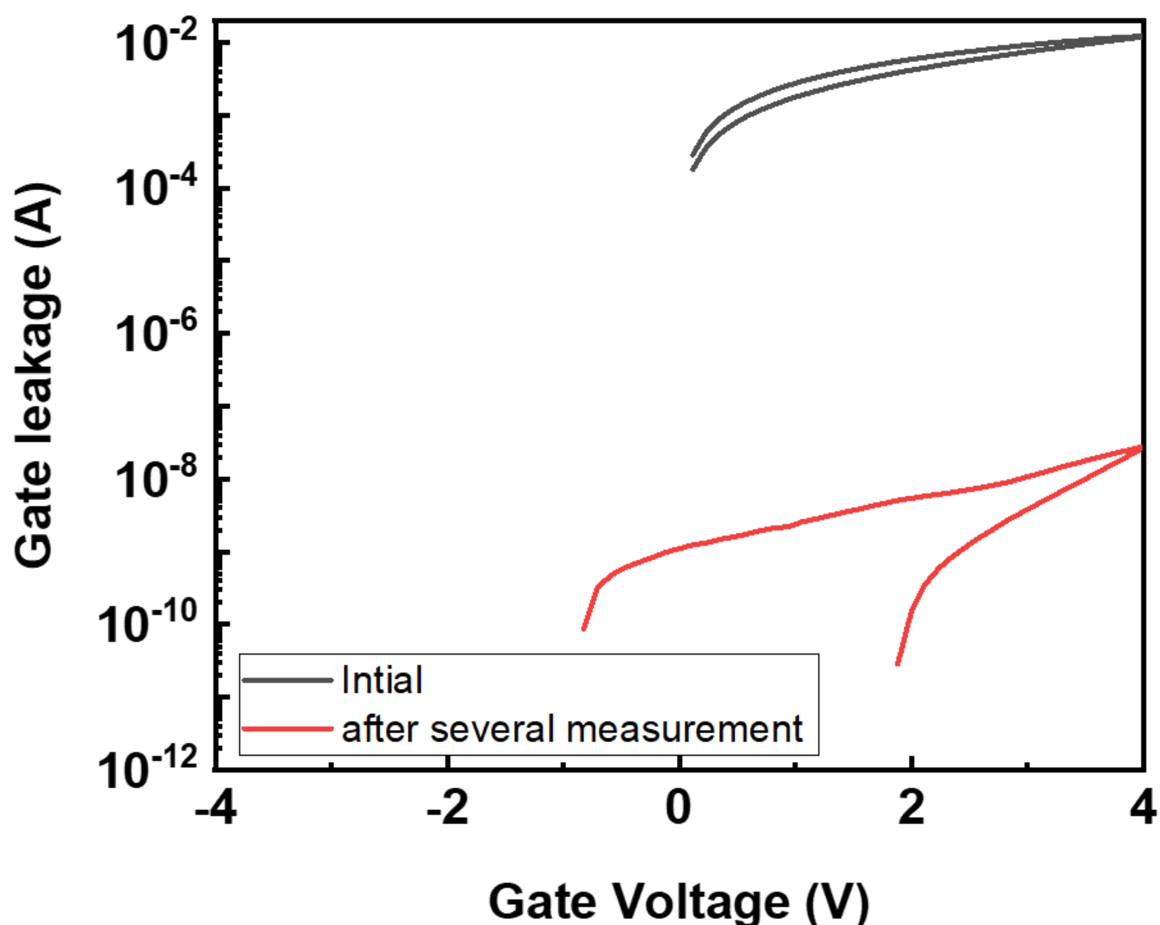

Fig. 5.25 Gate leakage of oxygen annealed initial and re-measured after several measurement.

5.4.5. FGT with sputtered ITO and CSD Y-HZO (vacuum annealed)/ sputtered HZO

As discussed in Chapter 4, CSD Y-HZO shows stable ferroelectricity with sputtered ITO layer even at high re-annealing temperature of 600 °C as compared to sputtered HZO. Hence, next, electrical properties of FGT were measured for sputtered ITO channel annealed at 600 °C in N_2 with CSD Y-HZO (vacuum annealed)/sputtered HZO. Figure 5.24 (a) and (b) shows transfer characteristics of FGTs for CSD Y-HZO and sputtered HZO, respectively. Figure 5.24 (a) shows I_D-V_G of FGTs with CSD Y-HZO and sputtered ITO channel. I_D-V_G clearly exhibits a standard n-channel transfer curve with a counterclockwise hysteresis loop due to the ferroelectric nature of the Y-HZO. However, FGTs with CSD Y-HZO and CSD ITO channel shows better device performance (see figure 5.22 (d)) compared to sputtered ITO channel. Possible reason for degraded performance for sputtered ITO channel FGT due to interface and

high carrier concentration. On the other hand, FGT with sputtered ITO and sputtered HZO can not be turned off and remains in on state even after 4 MV/cm electric field which is due to paraelectric nature of sputtered. These results suggest that CSD oxide channel with CSD Y-HZO (vacuum annealed) shows better device performance and sputtered HZO is not suitable for FGT applications.

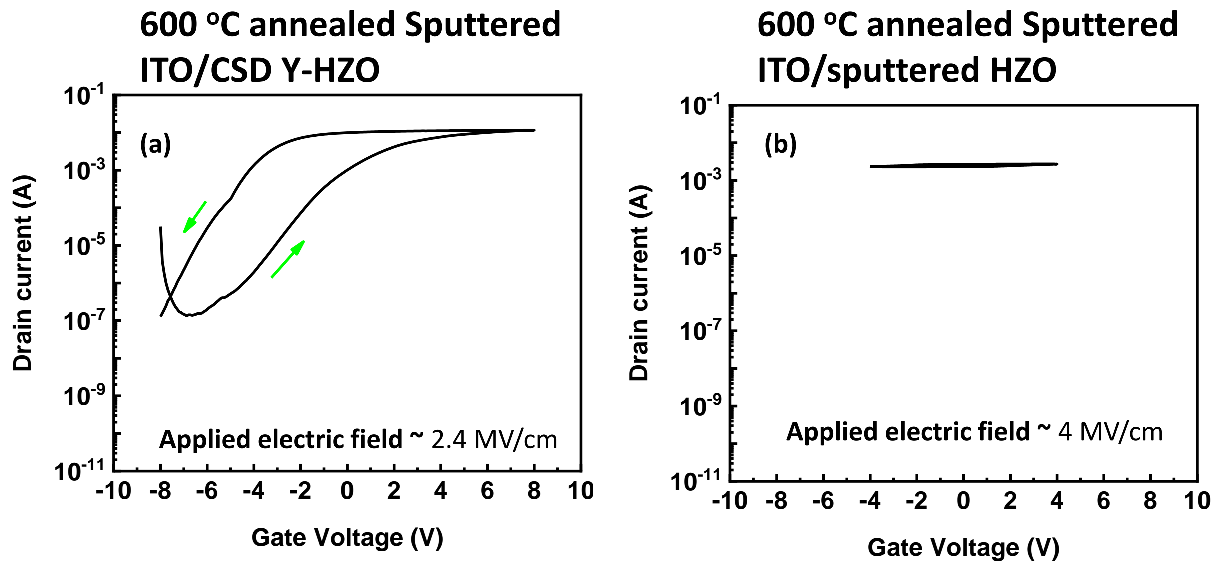

Fig. 5.24 Electrical properties of FGT with sputtered ITO annealed in N_2

5.4.6. Comparison of FGT performance with previous work

Table 5.1 summaries the FGT device performance with various parameters for comparison between previous report and current work. Most of these reports has one thing common HZO and oxide semiconductor channel is deposited by ALD and sputtering, respectively. In addition, low on current and small memory window was obtained. On contrary, in this work, both layers were deposited by CSD. On current and memory window of 16 mA and 3.9 V (ITO 13 nm channel) respectively, which is much larger than compared to previous report. On/off ratio of 10^6 and low SS value (5 nm CSD In_2O_3) of 70 mV/dec which is comparable to previous reports. Overall, CSD oxide channel with CSD Y-HZO shows better FGT performance.

Table 5.1. Comparison and summary of FGT device performance with previous reports and this work

Ferroelectric gate insulator material	Oxide channel material	W/L	SS (mV/dec)	On current (mA)	On/off ratio	Memory window (V)	Reference
ALD HZO	Sputtered IGZO (8 nm)	50/50	~60	~.001	~10^6	0.6	[3],[10]
ALD HZO	Sputtered IZO (15 nm)	1000/40	~82	~.015	~10^6	1	[5]
ALD HZO	Sputtered ITO (1 nm)	-	-	~.025	~10^6	0	[4]
CSD Y-HZO	CSD In_2O_3 (5 nm)	100/5	70	8	7 x 10^6	0.66	This work
CSD Y-HZO	CSD ITO (13 nm)	100/5	198	16	5 x 10^6	3.9	This work

5.5. Conclusion

We have fabricated bottom gated FGT with Y-HZO as a gate insulator and 5-24 nm thick In_2O_3 and ITO as a channel. At first, the ferroelectric properties of vacuum annealed and oxygen Y-HZO with different thickness of In_2O_3 and ITO were evaluated. It was found that vacuum annealed Y-HZO films shows good ferroelectric properties when the thickness of In_2O_3 and ITO was less than 13 nm and compared to oxygen annealed Y-HZO. When the thickness of In_2O_3 and ITO increased to 22-24 nm, the MFS structures showed ferroelectric nature but P-V loops became slightly rounded due to the increase of leakage current. The case of But Fabricated bottom gate FGTs with thin In_2O_3 and ITO channel, demonstrated normal n-channel transistor operation with hysteresis in the transfer curves due to the ferroelectric nature of the Y-HZO gate insulator. A low SS value of 70 mV/decade (5 nm In_2O_3 channel), high on/off ratio of 10^6, large memory window, and large on current were obtained and the FGT with a channel thickness around 13 nm shows better device performance. CSD oxide semiconductor channel with CSD Y-HZO shows better FGT performance compared to sputtered oxide channel or previous reports. Sputtered ITO with sputtered HZO is not suitable for FGT applications

Reference

[1] B. Park, *Topics in Applied Physics 131 Ferroelectric- Gate Field Effect Transistor Memories*. 2016.

[2] K. I. Haga, Y. Nakada, D. Ricinschi, and E. Tokumitsu, “Relationship between source/drain-contact structures and switching characteristics in oxide-channel ferroelectric-gate thin-film transistors,” *Jpn. J. Appl. Phys.*, vol. 53, no. 9, 2014, doi: 10.7567/JJAP.53.09PA07.

[3] F. Mo *et al.*, “Experimental Demonstration of Ferroelectric HfO2 FET with Ultrathin-body IGZO for High-Density and Low-Power Memory Application,” *Dig. Tech. Pap. - Symp. VLSI Technol.*, vol. 2019-June, pp. T42–T43, 2019, doi: 10.23919/VLSIT.2019.8776553.

[4] M. Si *et al.*, “Indium-Tin-Oxide Transistors with One Nanometer Thick Channel and Ferroelectric Gating,” *ACS Nano*, vol. 14, no. 9, pp. 11542–11547, 2020, doi: 10.1021/acsnano.0c03978.

[5] Y. Li *et al.*, “A Ferroelectric Thin Film Transistor Based on Annealing-Free HfZrO Film,” *IEEE J. Electron Devices Soc.*, vol. 5, no. 5, pp. 378–383, Sep. 2017, doi: 10.1109/JEDS.2017.2732166.

[6] Mohit, T. Murakami, K. Haga, and E. Tokumitsu, “Impact of annealing environment on electrical properties of yttrium-doped hafnium zirconium dioxide thin films prepared by the solution process,” *Jpn. J. Appl. Phys.*, vol. 59, no. SP, p. SPPB03, Nov. 2020, doi: 10.35848/1347-4065/aba50b.

[7] Mohit, K. Haga, and E. Tokumitsu, “Electrical properties of yttrium-doped hafnium-zirconium dioxide thin films prepared by solution process for ferroelectric gate insulator TFT application,” *Jpn. J. Appl. Phys.*, Jul. 2020, doi: 10.35848/1347-4065/ab86de.

[8] Y. Hu *et al.*, “Origin of Indium Diffusion in High-k Oxide HfO2,” *ACS Appl. Mater. Interfaces*, vol. 8, no. 11, pp. 7595–7600, 2016, doi: 10.1021/acsami.6b01068.

[9] T. Miyasako, M. Senoo, and E. Tokumitsu, “Ferroelectric-gate thin-film transistors using indium-tin-oxide channel with large charge controllability,” *Appl. Phys. Lett.*, vol. 86, no. 16, pp. 1–3, 2005, doi: 10.1063/1.1905800.

[10] F. Mo et al., “Low-Voltage Operating Ferroelectric FET with Ultrathin IGZO Channel for High-Density Memory Application,”

Chapter 6
Conclusion and future work

6. Conclusion and future work

6.1. Conclusion and summary of this research

Since the unexpected discovery of ferroelectricity in hafnium oxide-based materials, the interest in HfO_2 based ferroelectric films is continuously on the rise for various application such as Ferroelectric Gate Transistor (FGT). To fabricate HfO_2-based ferroelectric films, atomic layer deposition (ALD) and sputtering are usually used. On the other hand, chemical solution deposition (CSD) method provides the opportunity to fabricate inexpensive devices for various applications at low cost. There are only a few reports on CSD for ferroelectric HZO films and doping effect in HZO films by CSD has not been investigated. The objective of this research was to develop the chemical solution process for HfO_2-based ferroelectric films and to apply them to ferroelectric-gate transistors (FGTs). To realize FGTs, oxide semiconductor or conductor, In_2O_3 or In-Sn-O (ITO) was used as a channel and yttrium doped HZO was used as gate insulator material. Thin film transistors (TFTs) using solution processed HZO ferroelectric gate insulator with solution processed In_2O_3 or ITO oxide channel have not been reported.

Chapter 1

In this chapter, introduction to this research, the brief history of ferroelectricity was revisited. Structure and ferroelectricity of Conventional material and their disadvantages were reviewed. HfO_2 and ZrO_2 crystal structure and stabilization of ferroelectricity was summarized. The basic principle and requirement for FGT with oxde channel were elaborated in detail. The objective of this research is to fabricate FGT with CSD Y-HZO and CSD oxide channel.

Chapter 2

In this chapter, various deposition method for deposition of ferroelectric HfO_2 were discussed. General fabrication process used in this work for deposition of CSD thin film also describe. Later comparison of previous CSD ferroelectric HfO_2 with this work also discussed. Analytical methods which were used in this work also described in detail.

Chapter 3

In this chapter, Impact of annealing temperature and environment on ferroelectric Y-HZO were fabricated on $Pt/Ti/SiO_2/Si$ substrate by CSD, by annealing the films in vacuum, O_2, and N_2 environment. Effect of annealing temperature on vacuum annealed Y-HZO was demonstrated. Higher annealing temperature results in better ferroelectric properties. Vacuum annealed Y-HZO films show better properties and lower leakage current than the N_2 and O_2 annealed samples. This study clearly shows that the ferroelectric properties of Y-HZO films largely depends on the annealing environment and vacuum environment is effective to obtain good ferroelectric properties. This chapter clarifies important role of oxygen vacancy and carbon content on ferroelectric properties of Y-HZO. In addition, ferroelectric properties of HZO compared with previous report and current work. P-E loops in this work is not good but comparable in terms of P_r, especially when thickness of HZO films is around 40 nm. Most of the previous reports requires PMA to observed ferroelectricity in HZO films whereas in this work ferroelectricity in Y-HZO can be observed even after PDA.

Chapter 4

In this chapter, the stability of ferroelectricity of the MFM (without plasma exposure), MFM (with plasma damage), and MFS structures with sputtered HZO and CSD Y-HZO films was investigated. A thin ITO layer is deposited by sputtering on sputtered HZO or CSD Y-HZO to fabricate MFS structures. It was found that the sputtered HZO becomes paraelectric after re-annealing, MFM (without plasma exposure), MFM (with plasma damage) and MFS structure at 400 and 600°C in N_2 for 15 min. Paraelectric behavior was observed even in MFM (with plasma damage) and MFS structure after the ITO deposition before the re-annealing process. On the other hand, it was demonstrated that the CSD Y-HZO films have robust ferroelectric properties even after the re-annealing process at 600 ^{o}C, presumably due to the residual carbon in the films. It was found from secondary ion mass spectrometry that the residual carbon content of CSD Y-HZO films were as large as 5%. Such a large amount of carbon content could help prevent the formation of low symmetry phase or m-phase. C-V curves of the MFS structure with CSD Y-HZO clearly showed ferroelectric hysteresis with depletion of the ITO semiconducting layer. Therefore, the CSD Y-HZO films are promising for oxide channel ferroelectric gate transistor application.

Chapter 5

We have fabricated bottom gated FGT with Y-HZO as a gate insulator and 5-24 nm thick In_2O_3 and ITO as a channel. At first, the ferroelectric properties of Y-HZO with different thickness of In_2O_3 and ITO were evaluated. It was found that vacuum annealed Y-HZO films shows good ferroelectric properties when the thickness of In_2O_3 and ITO was less than 13 nm. When the thickness of In_2O_3 and ITO increased to 22-24 nm, the MFS structures showed ferroelectric nature but P-V loops became slightly rounded due to the increase of leakage current. Fabricated bottom gate FGTs with thin In_2O_3 and ITO channel, demonstrated normal n-channel transistor operation with hysteresis in the transfer curves due to the ferroelectric nature of the vacuum annealed Y-HZO gate insulator. A low SS value of 70 mV/decade (5 nm In_2O_3 channel), high on/off ratio of 10^6, large memory window, and large on current were obtained and the FGT with a channel thickness around 13 nm shows better device performance. CSD oxide semiconductor channel with CSD Y-HZO shows better FGT performance compared to sputtered oxide channel or previous reports. Sputtered ITO with sputtered HZO is not suitable for FGT applications.

6.2. Future work

In present study, FGTs were fabricated with oxide semiconductor or conductor, In_2O_3 or In-Sn-O (ITO) was used as a channel and yttrium doped HZO was used as gate insulator material by solution process. But there are several possibilities which needs to investigate.

First, it would be interesting to investigate ferroelectricity induced by other dopants such as Ce. Since Ce has two oxidation state which can act as oxygen scavenging. Hence stabilizing higher O-phase and results in high P_r. Later fabricate FGT with Ce doped HZO and compare with Y-HZO

Secondly, Pt(111) was used as in this work as bottom electrode. It would be interesting to investigate effect of different bottom electrode such TiN, TaN, W. TaN and TiN are well known oxygen scavenger which would help to enhance ferroelectricity.

Thirdly, realizing ferroelectricity in sub 10 nm and 1 µm Y-HZO films for ultra-thin FGT and piezoelectric applications.

Fourthly, in this work, we used CSD ITO and In_2O_3 as oxide channel for FGT. It would be interesting change to $BaSnO_3$ (BSO). Since BSO has high mobility compared to other oxide channel material.

Lastly, realizing ferroelectricity in undoped HfO_2 by vacuum annealing and fabricating FGT.

6.3. List of Accomplishments

A) Publications in peer-reviewed Scientific journals

1. Mohit, K. Haga, E. Tokumitsu, "Electrical properties of yttrium-doped hafnium-zirconium dioxide thin films prepared by solution process for ferroelectric gate insulator TFT application", *Jpn. J. Appl. Phys.,* 59, pp. SMMB02-1-9, 2020.

2. Mohit, T. Murakami, K. Haga and E. Tokumitsu, "Impact of annealing environment on electrical properties of yttrium-doped hafnium-zirconium dioxide thin films prepared by the solution process" *Jpn. J. Appl. Phys.* 59 SPPB03, 2020.

3. Mohit, Takaaki Miyasako and Eisuke Tokumitsu, "Indium oxide and indium-tin-oxide channel ferroelectric gate thin film transistors with yttrium doped hafnium-zirconium dioxide gate insulator prepared by chemical solution process", *Jpn. J. Appl. Phys*. 60 SBBM02, 2021.

4. Mohit, Shinji Migita, Hiroyuki Ota, Yukinori Morita and Eisuke Tokumitsu, "Thermal stability of ferroelectricity in hafnium-zirconium dioxide films deposited by sputtering and chemical solution deposition for oxide-channel ferroelectric-gate transistor applications" 14 041006, 2021.

B) Manuscripts under preparation

2) Mohit, Diasuke Hirose, Yuzuru Takamura and Eisuke Tokumitsu,"Development of novel DNA biosensor using HfO_2 gate insulator and In_2O_3 channel BioTFTs prepared by solution process"

C) Conferences

International Conferences:

1. Mohit, Ken-Ichi Haga, Eisuke Tokumitsu, "Preparation of Ferroelectric Yttrium-doped Hafnium-Zirconium Dioxide Thin Films by Solution Process", International Workshop on Dielectric Thin Films for Future Electron Devices: Science and Technology (IWDTF 2019), Tokyo, Japan, Nov 2019 (Poster)

2. Mohit, Takaaki Miyasako and Eisuke Tokumitsu, "Fabrication of Indium-Tin-Oxide Channel Ferroelectric-Gate Thin Film Transistors using Yttrium Doped Hafnium-Zirconium Dioxide by Chemical Solution Process", SSDM, Toyama September 2020 (Oral).

3. Mohit, Shinji Migita, Hiroyuki Ota, Yukinori Morita and Eisuke Tokumitsu, “Robustness of ferroelectricity in hafnium-zirconium dioxide films deposited by sputtering and chemical solution deposition for ferroelectric transistor applications”, ECS PRiME, Hawaii, USA, October 2020. (Poster)
4. Mohit, Daisuke Hirose, Eisuke Tokumitsu and Yuzuru Takamura, “DNA biosensing using Indium Oxide thin film transistor with HfO_2 as gate insulator prepared by solution process”, E-MRS spring 2021, France, May 2021. (Poster-accepted)
5. Mohit and Eisuke Tokumitsu “Preparation of ferroelectric lanthanum doped hafnium-zirconium oxide thin films by solution process”, EM-Nano 2021, May 2021. (Oral-accepted).

Domestic Conferences:

1. Mohit, Yoshiaki Sumitomo, Ken-chi Haga, Keisuke Ohdaira, Eisuke Tokumitsu, “Sub-20 nm thick ferroelectric Hf-Zr-O films fabricated by solution process for ferroelectric-gate TFT applications”, Thin Film Materials & Devices Meeting (TFMD 2019), Kyoto, Japan, November 2019 (Poster).

2. Mohit, Jyotish Patidar, Ken-Ichi Haga, Eisuke Tokumitsu, “Fabrication of ferroelectric hafnium-zirconium dioxide thin films by solution process”, JSAP spring meeting 2020, Tokyo, March 2020 (Oral)

3. Mohit, Ken-Ichi Haga, Eisuke Tokumitsu, “Effect of Annealing Environment on Ferroelectric Properties of Hf-Zr-O (HZO) Thin Films Prepared by Solution Process”, Ferroelectric Meeting and Their Applications (FMA 37), Kyoto, Japan, May 2020 (Oral).

4. Mohit, Eisuke Tokumitsu, “Ferroelectric Properties of Hafnium-Zirconium-Dioxide Prepared by Chemical Solution Process for MFM and MFS Structures”, JSAP autumn meeting 2020, Kyoto, September 2020 (Oral)

5. Mohit, Shinji Migita, Hiroyuki Ota, Yukinori Morita and Eisuke Tokumitsu, Fabrication of ferroelectric gate thin film transistors using CSD Y-HZO and sputtered HZO with sputtered ITO channel JSAP spring meeting 2021, Tokyo, March 2021 (Oral)

6. Yuki Hara, Mohit, Shinji Migita, Hiroyuki Ota, Yukinori Morita and Eisuke Tokumitsu Improvement of stability of ferroelectricity in sputtered Hf-Zr-O films, FMA 38, Kyoto Japan, May 2021 (Oral).

D) Award and Research grant

Principal investigator for JAIST Research Grant (Fundamental Research) 2020 (on going).